UNIVERSITÀ DEGLI STUDI
DI MODENA E REGGIO EMILIA

Dottorato di ricerca in Ingegneria industriale e del territorio

Ciclo XXXVIII

On the development of a 3D-CFD model for hydrogen-fuelled internal combustion engine cycle simulations

Candidato: Stefano Sfriso

Relatore (Tutor): Prof. Fabio Berni

Correlatore (Co-Tutor): Prof. Stefano Fontanesi

Coordinatore del Corso di Dottorato: Prof. Alberto Muscio

Thesis index

Abstract....4
Introduction....6
Chapter 1. Physical models.....10
Chapter 2. Numerical framework validation and preliminary engine study.....26
Chapter 3. Combustion analysis and optical engine comparisons.....53
Chapter 4. Flame instability effect.....69
Conclusions....80
Acronyms and abbreviations....83
Latin symbols....83
Greek symbols....85
Subscripts....85
Bibliography....85

Abstract

The scientific community's ongoing pursuit of innovation has revived interest in hydrogen as a fuel for internal combustion engines (ICEs). This is only the latest wave in a long history of attention to hydrogen, considering that the first ICE car ever built, the de Rivaz prototype (1807), was hydrogen-fuelled. The European Union's increasingly strict emission targets for road vehicles have further fuelled this revival, especially after the "diesel gate" scandal, which revealed how difficult it was for manufacturers to meet tighter standards without expensive redesigns, complex aftertreatments, or hybridization, each reducing competitiveness. Despite industry challenges, EU policy has continued to tighten, culminating in the planned 2035 90% emissions reduction of ICEs, with the intention to relegate them to a niche market. In this context, hydrogen reemerged as a potential transitional fuel toward carbon neutrality, allowing continued use of well-established ICE technology instead of complete replacement.

The viability of hydrogen ICEs, however, depends strongly on how hydrogen is produced and distributed. While widespread use in light-duty vehicles remains unlikely in the short term, hydrogen engines appear more realistic for heavy transport applications such as trucks or ships.

Hydrogen use in ICEs is thus not a technological breakthrough, and its field of application seems limited. Yet, hydrogen-fuelled ICEs hold great research value, particularly in 3D CFD (computational fluid dynamics) modelling. Hydrogen's unusual fuel properties make it a demanding benchmark for frameworks originally developed for gasoline engines, revealing how much of the modelling relies on robust physical laws versus empirical correlations. Moreover, hydrogen's exceptional combustion characteristics force the computational framework to remain as general and physically grounded as possible.

This work presents the development and validation of a 3D CFD framework through three stages. The first phase employed a Lombardini 15LD500 single-cylinder engine, originally a naturally aspirated diesel, retrofitted by the University of Pisa for direct hydrogen injection. Tests covered equivalence ratios (φ) from 0.4 to 0.8 and speeds from 1500 to 3000 rpm, for a total of 11 operating points across the engine map. Remarkably, one single set of calibration constants reproduced experimental data for all conditions using nominal spark timing, strengthening confidence in the framework and enabling detailed analysis of combustion physics.

The second phase focused on the PSA EP6 engine, a stock-based single-cylinder unit with an optically accessible modified piston, tested by the University of Orléans in port fuel injection

(PFI) mode. By eliminating mixture-stratification uncertainties, this setup allowed a more accurate evaluation of the model's ability to reproduce combustion behaviour, the primary driver of heat release. Tests covered a narrower range of 1200–1500 rpm and $\varphi < 0.55$, extending down to 0.30, the leanest condition. This phase enabled investigation of secondary phenomena such as wall-flame quenching and instability. The latter remains an open topic, mainly because (1) modelling flame instability in 3D CFD URANS remains difficult, with only one established method to date, and (2) its effects on turbulent, transient ICE flames are still poorly understood.

The final phase introduced a new method to represent flame instability within URANS simulations. This approach provided an initial assessment of instability effects under tested conditions and, more broadly, improved the predictive capability of 3D CFD frameworks for hydrogen-fuelled ICEs.

Introduction

The utilization of hydrogen as a primary fuel for internal combustion engines (ICE) possesses a significant historical lineage. Excluding the development of Fuel Cell Electric Vehicles (FCEVs) to focus specifically on Hydrogen Internal Combustion Engine Vehicles (HICEVs), the conceptual origin dates back to the de Rivaz prototype of 1806 [1]. A subsequent milestone was achieved in 1862 by Étienne Lenoir, who developed a vehicle featuring a two-stroke hydrogen-fuelled engine [2]. Following these early iterations, a prolonged period of dormancy ensued before a resurgence of interest occurred in 1979, marked by BMW's conversion of a production gasoline model to hydrogen propulsion [3]. In the following decades, manufacturers such as Toyota, Mazda, Ford and Chevrolet joined the research field [4], leading to the contemporary landscape where companies including Volvo, Iveco, Scania, MAN, Alpine, and AVL are developing diverse power units ranging from single-cylinder research engines to full-scale production prototypes [5].

This historical trajectory mirrors the broader evolution of the industrial world. During the early turbomachinery era, machine efficiency was notably low, making fuel properties critical for achieving any viable power output. Furthermore, because modern refined hydrocarbons like gasoline and diesel were not yet established and the evaporation of liquid fuels was technically challenging, hydrogen, a gas with high power density, represented an optimal choice. As technical capabilities evolved, hydrocarbons came to dominate the market for a century. This dominance remained unchallenged until the energy crises of the 1970s prompted concerns regarding the depletion of global oil reserves and the geopolitical risks associated with hydrocarbon dependency.

Despite the renewed interest in the late 20th century, the high state of development in hydrocarbon-based ICEs highlighted significant deficiencies in hydrogen performance. A prominent example is the 2006 dual-fuel BMW Hydrogen 7; its 6.0L V12 engine produced 445 hp when fuelled by gasoline, yet only 260 hp when operated on hydrogen [6]. This performance gap is particularly striking given that a stoichiometric hydrogen-air mixture contains approximately 16% more energy than a stoichiometric gasoline-air mixture. The disparity is largely attributed to hydrogen's low density, which displaces oxygen in the intake manifold, thereby reducing volumetric efficiency.

More recently, the potential phase-out of internal combustion engines driven by European Union decarbonization mandates has catalysed a new wave of alternative fuel research. The objective is to achieve deep decarbonization while maintaining the competitiveness of the European automotive industry. In this modern context, advanced technology has enabled hydrogen engines to reach efficiencies and power outputs comparable to their hydrocarbon counterparts. However, for light-duty transportation, hydrogen adoption is hindered by significant obstacles in distribution infrastructure and on-board storage. Consequently, the heavy-duty transportation sector has emerged as the primary actor in hydrogen research, as these larger vehicles are less constrained by the volumetric requirements of high-pressure hydrogen tanks.

Contemporary research has transitioned beyond feasibility demonstrations toward achieving higher power density, increased efficiency, and minimized tailpipe emissions. While hydrogen oxidation produces no CO_2, the high temperatures reached during the flame propagation process can lead to significant NO_x formation [7]. Consequently, lean and ultra-lean combustion strategies have gained prominence. These modes are technically viable due to hydrogen's exceptionally wide flammability limits and serve to reduce the adiabatic flame temperature, thereby mitigating NO_x production. This reduction is critical because NO_x species are a direct hazard for human health [8].

Operating under ultra-lean conditions, however, introduces complexities such as unusually low Lewis numbers Le of the fuel-oxidizer mixture. This phenomenon triggers thermo-diffusive flame instabilities, which become most evident in the leanest operating regimes.

In this advanced research scenario, the role of 3D Computational Fluid Dynamics (CFD) is fundamental for the fine-tuning and optimization of engine performance. The vast array of parametric variations, including piston bowl geometry, hydrogen jet-wall interaction in direct-injection systems, and flow field organization, can be evaluated more efficiently through the use of "Digital Twins." For these digital representations to be effective, the underlying models must demonstrate high reliability to ensure that predicted trends resulting from parametric changes are trustworthy. The primary objective of CFD in this context is not the exact replication of experimental data, which serves mainly for calibration, but rather the accurate prediction of performance trends to guide engine development toward the most promising configurations.

Before this research, flame instability modelling was rarely incorporated into ICEs simulations. Notably, Hernandez et al. [9] was the first to recently introduce an approach similar to the one employed here, following fundamental DNS studies that established initial correlations [10], [11]. The recent resurgence of interest in hydrogen combustion, coupled with the availability of computationally intensive thermochemical DNS, generated a fertile environment for fundamental research to provide the groundwork for high-level URANS modelling. It is worth noting that, prior to this study, the state of the art for hydrogen-fuelled engine simulations did marginally address flame instability; this was due to both a lack of theoretical frameworks and a tendency to operate engines under thermochemical conditions where such instabilities were unlikely to occur. Consequently, the necessity for hydrogen flame instability modelling did never appear as a key problem. Main contributors to the field preceding this work include Kosmadakis and Rakopoulos, [12], [13], [14], Verhelst [7], [15] and Maio [16], [17], employing approaches to model the hydrogen combustion mainly inherited form the gasoline engines practice.

Rakopoulos and Kosmadakis extensively used commercial 3D-CFD software employing variants of the fractal combustion model or standard Eddy Break-Up (EBU) models. Their work focused heavily on evaluating EGR rates, NO_x emissions, and cyclic variations in H_2 and H_2-methane blends. The fractal and EBU models, however, showed limitations at lean conditions operations: to compensate and match experimental pressure traces, the researchers often had to heavily tune model constants for every specific operating condition, reducing the predictive capability of the model across varying equivalence ratios.

Verhelst et al. attempted to integrate accurate laminar correlations into standard turbulent models like the Turbulent Flame Speed Closure (TFC) or Flame Surface Density (FSD) models. As highlighted in his comprehensive 2009 and 2014 reviews, Verhelst recognized that standard turbulence-chemistry interaction models break down for hydrogen. Standard FSD models assume that flame wrinkling is created entirely by turbulent eddies and destroyed by flame propagation. However, in hydrogen engines, the flame surface area can grows due to the spontaneous cellular structures formed by flame instabilities. Verhelst frequently noted that without accounting for stretch effects and Lewis number disparities, models simply could not predict the pressure rise rates seen in actual lean hydrogen operation without artificial adjustments.

Maio et al. applied the Extended Coherent Flame Model (ECFM) coupled with Large Eddy Simulation (LES) and Adaptive Mesh Refinement (AMR), to predict cyclic combustion variations in lean-burn hydrogen engines. ECFM, however, was originally formulated for hydrocarbon fuels (gasoline/diesel). It tracks flame surface density based on turbulence parameters. When applied to hydrogen, the base ECFM struggles because it natively assumes the flame stretch responses of a standard hydrocarbon. Maio's work demonstrated that while LES resolves the larger turbulent flow structures beautifully, the sub-grid models in ECFM failed to capture the sub-grid flame acceleration caused by hydrogen's unique diffusional characteristics. To get accurate results, especially for heavy-duty lean applications, ad-hoc corrections for the Lewis number and flame stretch had to be forced into the ECFM formulation.

The present work establishes a framework for 3D-CFD simulations of ICE working cycles specifically applied to hydrogen-fuelled engines, proposing a methodology to ensure computational reliability. This research aims to bridge the gap between emerging evidence of flame instability in hydrogen-fuelled internal combustion engines and current state-of-the-art combustion models that do not yet account for these effects, extensively discussing the conditions for their onset.

The initial phase involves the selection of physical models based on a rational analysis of the specific problem. In hydrogen applications, the combustion model is of particular importance. A simplified modelling approach is initially preferred to clarify the strengths and weaknesses of the framework while minimizing the number of calibration constants.

To validate the proposed framework, experimental data were utilized from a modified Lombardini 15LD500 single-cylinder engine, retrofitted for Direct Injection Spark Ignition (DISI) operation with H_2. The engine's two-valve head configuration allowed for the installation of two low-pressure injectors. This setup simplified the CFD representation of the hydrogen jet by avoiding the complexities of under-expanded supersonic flows typical of high-pressure injection. The validation matrix encompassed engine speeds from 1500 to 3000 rpm and equivalence ratios (φ) of 0.4, 0.6, and 0.8. Once a unique calibration was found for all the points, the framework accurately predicted trends across these diverse operating conditions, establishing a foundation for further refinement.

The second stage of the research focused exclusively on combustion physics under ultra-lean conditions. To isolate combustion phenomena from the uncertainties of mixture stratification, where errors in mixing and combustion modelling might inadvertently compensate for one another, a Port Fuel Injection (PFI) single-cylinder unit was employed. This ensured a highly homogeneous mixture, isolating the evaluation of the results to the performance of the ignition and combustion models. Testing was conducted at 1200 and 1500 rpm with extreme equivalence ratios ranging from 0.30 to 0.55.

The final phase of the study investigated the reasons why the framework could predict experimental pressure traces despite the absence of explicit thermo-diffusive instability modelling. Initial results indicated that the framework could reproduce experimental data with only minor recalibration of the ignition model when changing the engine. Subsequent detailed analysis, incorporating sub-models for instability laminar flame speed enhancement, turbulence dampening effect on it, and wall flame quenching, elucidated this behaviour.

It was determined that at the investigated conditions, the Indicated Mean Effective Pressure (IMEP) was sufficiently low to minimize the impact of flame instabilities. Furthermore, the enhancement of the laminar flame speed was effectively counterbalanced by the combined effects of wall quenching and turbulence interference. While these findings suggest that simplified models may suffice under certain conditions, it must be noted that these conclusions rely on qualitative assumptions prevalent in current literature. Further fundamental research is required to provide a quantitative understanding of flame instability effects in highly turbulent environments.

Note: parts of current work have been adapted from successive publications ([18], [19], [20], [21], [22], [23], [24]) during the years leading to this synthesis.

Chapter 1. Physical models.

1.1. Overview of the computational strategy.

The following section provides an overview of the computational framework selected for this research. An Unsteady Reynolds-Averaged Navier-Stokes (URANS) approach was adopted as the primary numerical strategy. While LES remains a theoretically viable alternative, Direct Numerical Simulation (DNS) is currently beyond the practical reach of internal combustion engine research due to its prohibitive computational requirements. The decision to utilize URANS over LES was driven by the specific statistical requirements of engine performance analysis. LES inherently resolves a portion of the turbulent scales, which are stochastic and transient by nature. Consequently, the flow field in an LES run consists of a mean component superimposed with resolved fluctuations, leading to cycle-to-cycle variations. To derive meaningful engineering metrics, such as the Indicated Mean Effective Pressure (IMEP), peak cylinder pressure, or combustion phasing, a significant number of consecutive engine cycles must be simulated and then ensemble-averaged.

While LES brings the utility, for example, of capturing the Coefficient of Variation (CoV) of the IMEP, a critical indicator of engine combustion stability and "roughness", it comes at the cost of massive computational overhead. In contrast, URANS provides a statistically averaged representation of the flow field in a single "representative" cycle. Assuming that the small-scale turbulence, which remains modelled in both approaches, exerts a secondary effect on the global engine behaviour, the URANS framework offers a robust and computationally efficient means of predicting the average performance trends necessary for this study.

URANS, on the other hand, have the great advantage of, conceptually, automatically average the cycles resolving only the steady average portion of the flow and entirely modelling the fluctuating component through a turbulence model. It is evident that the potential saving in terms of computational time, for the specific application of internal combustion engines, is huge, because significantly fewer cycles are necessary and with a coarser discretization of the fluid domain, as the high resolution of flow field fluctuations is not required anymore. Nonetheless, significant challenges persist, as the fidelity of the simulation is inherently tied to the models' capacity to accurately resolve the underlying physical phenomena. Stated that all the models have a physical base, there are often calibration constants that can adjust the predicted behaviour to match the real one. Consequently, there is a risk of reverting from a physical approach to empirical tuning. While empirical models may yield results that align closely with experimental data, they often lack the physical robustness required to ensure the model's reliability across varying operating conditions.

To delve deeper into the physics of these modelling approaches, it is fundamental to recognize that DNS, LES, and RANS all originate from the exact Navier-Stokes (NS) equations. The distinction lies in how much of the turbulent spectrum is directly computed versus modelled. RANS addresses the issue of computational effort by fundamentally altering the NS equations to solve only for the mean flow field, leaving the effect of all chaotic fluctuations to be approximated by a turbulence model.

Mathematically, standard RANS relies on Reynolds decomposition, where the instantaneous velocity is split into a time-averaged component and a fluctuating component:

$$u_i(x,t) = \overline{u_i}(x) + u_i'(x,t)$$

Substituting this decomposition into the NS equations introduces unclosed terms (the Reynolds stresses) that must be modelled. This is typically achieved using the Boussinesq hypothesis, which assumes that turbulent fluctuations act similarly to molecular viscosity, extracting kinetic energy from the mean flow to enhance mixing. Models utilizing this approach are consequently known as eddy viscosity models.

While this time-averaging framework is perfectly suited for statistically steady flows, it cannot natively handle an inherently transient problem like the working cycle of an internal combustion engine. For such applications, the framework must transition to Unsteady RANS (URANS). In URANS, the decomposition is no longer based on a time average, but rather on an ensemble average (or phase average) across multiple hypothetical engine cycles. The resolved velocity field represents the ensemble mean at a specific crank angle:

$$\langle u_i(x,t) \rangle = \frac{1}{N}\sum_{n=1}^{N} u_i^{(n)}(x,t)$$

Despite this conceptual shift from time to ensemble averaging, the closure problem remains identical, and standard eddy viscosity models are still employed to model the fluctuations. Applying these models to a transient problem relies on two fundamental assumptions:

The ergodic hypothesis: this postulates that the statistical properties of turbulence fluctuating over time (in a steady flow) are equivalent to the chaotic variations occurring across multiple repetitions of the same experiment (ensemble fluctuations) at a specific instant.

Scale separation: URANS mathematically treats each discrete timestep as a localized, quasi-steady RANS computation. For this to be physically valid, the turbulent energy cascade must have sufficient time to fully establish and dissipate within that specific time interval. Therefore, URANS requires a separation of scales: the computational timestep must fall into a "spectral gap". It must be small enough to accurately discretize the transient macroscopic flow, yet strictly larger than the turnover time of the turbulent eddies.

Adhering to these fundamental principles, the selection of sub-models detailed in the subsequent sections prioritizes mathematically robust, physics-based formulations to respect these limits and mitigate the reliance on ad-hoc empirical calibration.

1.2. Sub models: turbulence and heat transfer

The choice of sub-models starts from the turbulence model, for which the eddy viscosity assumption is adopted. The 2 equations closure k-ε RNG [25], [26] is chosen. This model is widely used in literature and in propaedeutic publications [27], [28], [29], [30], [31], [32].

The near-wall flow is modelled by a high-Reynolds wall treatment to minimize the computational time. The "Improved GruMo-UniMORE" model is used for the heat transfer prediction [33], [34], [35]. It is independent of the near-wall grid resolution, using the effective Prandtl number of the gas mixture.

The turbulence model have been considered as an invariant of the framework for the following reasons: it is hard to justify the preference of one model to another, in the field of engine applications; selecting different models would lead to different framework behaviour and consequently need to calibrate differently ignition and combustion models. Furthermore, there is little justification for prioritizing one turbulence closure over another, as the current experimental data provides no definitive benchmark to verify the local accuracy of the flow field predicted by any specific model. Similar arguments are applied to the heat transfer model, as no direct investigation on the heat rejection have been carried out in the experimental activities during which the experimental data here used were obtained. In fact, the sensitivity of the final results would be influenced by the different wall temperatures selected for each case other than the heat transfer model itself. Having no wall temperatures data for any of the engines studied, thus, trying other wall transfer models would have been irrelevant. All this considered, the selection of such models was purely based on previous experiences.

1.3. Sub models: ignition

The rationale for utilizing a dedicated ignition model, rather than simply initializing a small flame kernel for the combustion model to evolve, is revisited here. During the inception stage, turbulence exerts a limited influence on kernel development. This is due to the fact that the integral length scales of the flow field, those responsible for wrinkling the flame front and accelerating its propagation, are of the same order of magnitude as the nascent kernel itself [36]. Modelling its first development as driven by the full turbulent spectrum, as a combustion model would do, may thus lead to an overestimation of the kernel growth speed. Moreover, a big part of the early flame development is due to the thermal expansion of it [36] due to the high temperatures of the plasma channel found between the electrodes. Without a dedicated model to represent this phenomenon, this detail would be lost.

To capture the ignition physics discussed above, a model developed within the research group is implemented via a user-coded routine. In the current framework, delays associated with the electrical circuit are neglected. This simplification is justified by the extremely short duration, approximately 10 μs, between the nominal spark command and the actual dielectric breakdown, a timeframe that proves negligible relative to the crank angle resolution at the engine speeds investigated [37], [38], [39].

The model starts with the deposition of an initial spherical flame kernel. Then, its growth is governed by a 1D ordinary differential equation (ODE) whose unknown is the kernel radius. The equation is solved starting from the spark timing until a threshold value for the unknown variable is reached. The 1D ODE is detailed in Equation 1 and it is similar to the Herweg and Maly model [36].

$$\frac{dr_k}{dt} = \frac{\rho_u}{\rho_k}(S_l + S_{Plasma}) + \frac{V_k}{A_k}\left[\frac{1}{T_k}\frac{dT_k}{dt}\right] \qquad (1)$$

Meaning of symbols is clarified in the dedicated section. Attention should be posed on the first term of right side of equality, where laminar flame speed S_l and expansion velocity of the plasma column forming in the spark gap S_{Plasma} appear. Unlike Herweg and Maly model, the present approach relies, as highlighted, on a laminar flame speed inside Equation 1, instead of a turbulent one with an associated damping function. In other words, instead of a smooth transition form laminar to turbulent flame speed, a step function is adopted. Once a threshold value of r_k is reached, the ignition model (i.e. the ODE) stops and the flame propagation is governed by G-equation. As for the threshold value, reference [36] suggests that the turbulence contribution is significant after ≈ 2 mm, thus reducing the accuracy of the 1D model.

In order to infer the value of S_{Plasma}, Equation 2 is employed, which is a one-dimensional unsteady heat conduction equation.

$$\rho c_p \frac{\partial T}{\partial t} = \frac{\partial}{\partial x}\left(k \frac{\partial T}{\partial x}\right) \quad (2)$$

Among the quantities appearing in Equation 2, density ρ, specific heat c_p, and thermal conductivity k are properties related to plasma, for which the experimental measure is difficult. Estimations can be found in [40], [41], [42], [43], [44], [45], where the product $\rho \cdot c_p$ is reported equal to 8000 J/(m^{3}K), while thermal conductivity and boundary condition for the Equation 2, i.e. the temperature at x=0, are suggested equal to 0.2 W/(mK) and $60 \cdot 10^3$ K, respectively.

The initial condition of Equation 1, namely the initial value of r_k ($r_{k,init}$), is evaluated via a simplified method similar to the one proposed by Colin [46]. The initial kernel is assumed as a perfect sphere with radius $r_{k,init}$, whose volume equals the volume of the plasma channel formed between the electrodes, supposed as a perfect cylinder. In this regard, the height of the cylinder corresponds to the spark gap (d_{gap}= 0.5 mm in this case) while the radius is the laminar flame thickness (δ_l) at the unburnt gas conditions at the spark-plug. Equation 3 expresses the volume of the cylinder, from which $r_{k,init}$ can be inferred, as shown by Equation 4.

$$V_{k,init} = d_{gap} \pi {\delta_l}^2 \quad (3)$$

$$r_{k,init} = \left(\frac{3}{4\pi} V_{k,init}\right)^{1/3} \quad (4)$$

It is worth noting that the adoption of Equation 3 is related to the fact that, if the ignition is successful, the volume of the initial kernel is assumed for simplicity equal to the plasma channel one. The latter is modelled as a cylinder characterised by a height equal to the spark gap and a radius equal to the laminar flame thickness. The spark gap is selected as the spark extends between the electrodes. As for the laminar flame thickness, its adoption ensures that the kernel radius is fixed at the minimum. In fact, once the cylindrical geometry is assumed for the kernel, the radius cannot be lower than the laminar flame thickness.

In the software implementation, to resume, the model works as a delay calculator, assuming that the first part of the kernel development can be well approximated as zero dimensional. From the nominal crank angle of spark time a spherical G=0 surface is initialized, but the combustion model is not switched on till the iteration in which the ignition model computes a value for r_k equal to $r_{k,init}$. This radius is chosen as the calibration parameter of the model. While literature provides empirical estimates for this parameter, its value is highly sensitive to the specific engine geometry and operating conditions. Physically, this parameter governs the local turbulence scales, thereby establishing the critical kernel size at which the flame front begins to interact with the full turbulent spectrum. Figure 1 tries to clarify the functioning of the model: it reports 5 pictures, taken with a view pointing from the piston to upwards, of the flame during its development.

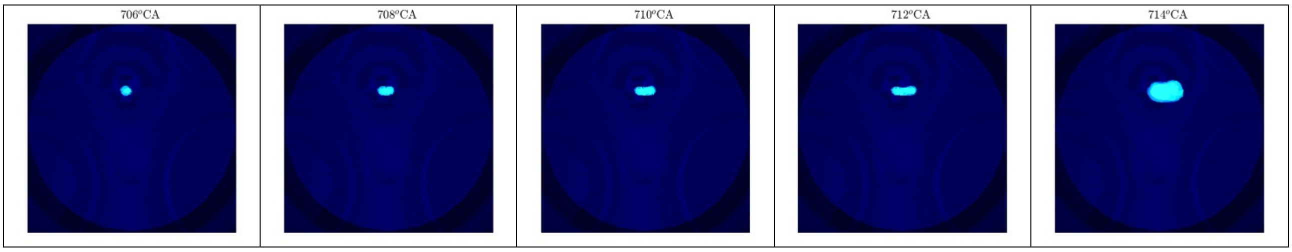

Figure 1: Flame kernel during the action of ignition model.

In the picture, 720°CA (Crank Angle) is the Top Dead Centre firing (TDCf), and the spark time is 705°CA. In the first picture, the initial kernel deposed is visible, then up to 712°CA the kernel does not expand but is only advected by the local mean flow, as visible by the progressive elongation in the direction of the local velocity in the first 4 pictures (towards right). At 712°CA, the ignition model finally reaches the imposed limit kernel radius, in this specific case 2.3 mm, and thus allow the combustion model to start propagate the flame, as visible from the last frame of the Figure. Despite this behaviour is not the most physical, still allows for a fair representation of the delay that should elapse before the flame kernel starts its propagation driven by the full turbulent spectrum. It should be emphasized that the 7°CA delay depicted in this instance corresponds to an extreme case among those tested. This condition was chosen specifically to illustrate the ignition model's performance under high-latency conditions, where its underlying mechanisms are most visible.

1.4. Sub models: combustion

Combustion model selection represents a critical component of the framework development; the fidelity of the final results is intrinsically linked to the chosen modelling approach and the precision of its associated calibration parameters. There are three main candidate methods to model the combustion in internal combustion engines, emerged as the predominant choices in the field of 3D-CFD: level set methods, flame surface density methods and detailed chemistry methods. Detailed chemistry is the most elementary approach, as it is sufficient to choose a chemical kinetic mechanism and no calibration is generally possible. It is, however, even too much simplified, because no turbulence-flame interaction is accounted for. Despite in some applications this may not be an issue, like gas turbines where a flame generally is not present as they operate in the well stirred reactor regime, it may be a problem in internal combustion engines, generally operating in the flamelet regime. All the nomenclature of combustion regimes are here defined according to Peters [47]. The detailed chemistry approach, on the other hand, can be successfully employed to model the emissions. This last advantage, however, is not judged important enough to prevail on the disadvantage, bringing to the decisions to discard this approach as it is not suitable for the application in internal combustion engines.

The flame surface density approach, on the other hand, relies on a simplified chemistry, that joins the model only through the off-line definition of a laminar flame speed, but it takes into account for the increased flame surface per unit volume due to the wrinkling induced on the flame by the turbulence. Being a complementary approach to the detailed chemistry, advantages and disadvantages are now flipped. In particular, only some pollutant emissions predictions are now possible and only if integrating additional sub-models, but the turbulence-flame interaction typical of internal combustion engines operating in the flamelet regime is now accounted for. ECFM-3Z is the most common model pertaining to this category, widely used in literature on gasoline engine. Despite this, it is a quite complex model, featuring many contributions for the production and destruction of the flame surface density in its transport equation, each of which with a specific calibration constant. Due to its complexity and specific calibration tailored for the gasoline engine, therefore, this approach has been initially discarded as well. Nevertheless, the performance of this model in some of the studied cases was assessed [48], with the resulting data validating the decision to discard it.

The last viable approach is the level set one. It is based on the definition of a passive scalar, whose value represents the distance from the flame. The isosurface where this scalar equals zero, thus, can be intended as the flame itself. This scalar is then transported with a defined velocity, the turbulent flame speed, that is the laminar flame speed increased by the already discussed effect that turbulence has over it. Dependence on turbulence is represented in a more simple way, in this case, namely through empirical correlations based on turbulent quantities and chemical ones. "In its treatment of turbulent premixed flames, the methodology is functionally similar to the ECFM-3Z approach. Its main advantage is the ability to implement diverse turbulent flame speed correlations, thereby adjusting the modelling detail of turbulence-chemistry interactions as needed. The emphasis of the present work is on developing a simplified yet robust framework that effectively represents the essential physics of the combustion regime under investigation.

The choice of a flamelet combustion model is, to some extent, aprioristic. In fact, the combustion regime is at this stage supposed to allow for the use of such a combustion model, but there are still no rigorous evidences that the studied engine cases will fall in this combustion regime. A verification of this hypothesis will be carried out later in the current work, and lot of attention will be put in it: ultra-lean hydrogen combustion, in fact, lead to mixtures with Lewis numbers much lower than 1, thus making the assumptions underlying classical Peters' classification of combustion regimes weak and necessitating revision.

With regard to the alternative approaches that were ultimately not adopted, detailed chemical kinetics, although deemed insufficiently reliable for the present application, were nevertheless tested at selected operating points. These simulations were performed in combination with the G-equation approach in order to resolve the burned-gas composition in greater detail and to enable a more accurate prediction of emissions. This exercise highlights a potential advantage of detailed chemistry over the other modelling strategies; however, such an advantage becomes meaningful only when it is coupled with an additional modelling framework, in this case the level-set method.

Turning to the description of the model employed in this work, it is based on a level-set formulation in which the scalar field G, representing the signed distance from the flame front, is transported according to the governing equation reported in Equation 5. The flame front is identified by the iso-surface $G = 0$, while, by convention, positive values of Gcorrespond to the burned region.

$$\frac{\partial}{\partial t}\rho G + \frac{\partial}{\partial x_i}\rho u_i G = \rho S_T |\nabla G| \qquad (5)$$

Hypothesis of chemistry much faster than turbulence would lead, at this point, to the idea that the species immediately react while crossing the $G = 0$ iso surface. This consideration may be somehow true speaking of a single real engine cycle: but as the flame modelled here is the ensemble average of several flames of several individual cycles (RANS simulations), the combustion cannot be imagined to happen instantaneously crossing the flame. Instead, the progress of the combustion around the $G = 0$ isosurface should be statistically distributed, mimicking the statistical distribution of the individual flames of each cycle around the average one. That’s the reason why the concept of progress variable ‘c’ is introduced (Equation 6).

$$c = a_3\left[\operatorname{erf}\left(a_1 G / l_{F,t} - a_2\right) + 1\right] \qquad (6)$$

It is a scalar whose value progressively goes from 0 to 1 anchored, in the middle, to the $G = 0$ isosurface. In particular, its value is 0 ahead of the averaged flame and reaches 1 slightly after it. In the STAR-CD implementation [26], the software used in the computations, the width of this distribution is related to the so called turbulent flame thickness, obtained from the scalars G and G' through the algebraic relation reported in Equation 7. Equation 8, instead, reports the transport equation for G'. Meaning of all the symbols is reported in the dedicated symbols section.

$$l_{F,t} = \alpha \frac{\sqrt{G'}}{|\nabla G|} \quad (7)$$

$$\frac{\partial}{\partial t}\rho G' + \frac{\partial}{\partial x_i}\rho u_i G' - \rho S_T \frac{\nabla G' \cdot \nabla G}{|\nabla G|} = 2\frac{\mu_t}{\sigma_t}\left[\frac{\partial G}{\partial x_i}\frac{\partial G}{\partial x_i}\right] - c_s \rho \frac{\epsilon}{k} G' \quad (8)$$

The burnt mass of species is now computed proportionately to the progress variable value of each cell. The G-equation previously reported (Equation 5), is transported through a diffusive term containing the turbulent flame speed S_T. This point represents the juncture where turbulence is integrated into the modelling framework. The turbulent flame speed is typically determined through a correlation that augments the laminar flame speed to account for the heightened consumption rate. Within the flamelet regime, for which this model is intended, turbulence wrinkles the flame and thus enhance its effective area exposed towards fresh mixture. This increments the speed at which, macroscopically, the flame can advance. In a URANS, the scales of flow field falling in the turbulence spectrum are not resolved, thus it is not possible to represent the wrinkling directly in the computational grid. This is the reason why correlations are necessary to model it. Among the correlations, the Peters' one [47] and the Damköhler one [49] are the most widespread. In this work, a variant of the Damköhler' s one proposed by Herweg et al. [50] is used. It is a really basic correlation, including only one tuning constant and depending on the turbulent velocity u', and the laminar flame speed S_l. It is reported in Equation 9.

$$S_T = S_l\left(1 + A \cdot \left(\frac{u'}{S_l}\right)^{\frac{5}{6}}\right) \quad (9)$$

It is noteworthy to state that, despite its simplicity, this correlation could fit many different operative points in different engines, as the calibration constant (A) value, set to 3.3, was never modified through all the simulations carried out in this work.

The turbulent flame speed expresses a ratio of laminar flame speed increase due to turbulence action. Laminar flame speed, thus, needs to be computed as well. In general it is computed offline, e.g. not for each cell during the in-cylinder simulation. This technique would be in fact highly inefficient, because laminar flame speed does not depend on flow conditions but only on pressure, temperature and chemical composition (Exhaust Gas Recirculation (EGR) and equivalence ratio). The two most common ways to introduce it in the computations is through direct tabulation or correlations. In the current case, a correlation available in literature is selected, namely the one proposed by Verhelst et al. [51], reported in Equation 10.

$$S_l = S_{l,0} \cdot \left(\frac{T}{T_{ref}}\right)^{\alpha} \cdot \left(\frac{p}{p_{ref}}\right)^{\beta} \cdot (1 - 1.21 \cdot f_{res}) \quad (10)$$

It fits chemical kinetics computation results obtained with Konnov mechanism [52]. This correlation is valid for the following ranges of pressure (p), temperature (T), equivalence ratio (φ), and exhaust gases recirculation (EGR): 5 bar ≤ p ≤ 45 bar, 500 K ≤ T ≤ 900 K, 0.33 ≤ φ ≤ 5, and 0% ≤ EGR ≤ 50%. The combinations of pressure, unburnt temperature and equivalence ratio experienced by the mixture throughout all the studied cases are various but always inside the fitting ranges of Verhelst correlation (except for two operative points at φ=0.30 which are, however, really close to the lower limit of 0.33).

In the URANS framework, the modelled flame represents an ensemble average of all individual cycles. It is important to note, however, that the laminar flame speed S_l calculated using mean values for pressure, temperature, equivalence ratio, and EGR is not necessarily equivalent to the average of the flame speeds calculated for each discrete cycle. To compensate, to some extent, for this, the employed software performs an integration of the turbulent flame speed over the space of the possible mixture fractions at each cell. More in detail, it is supposed that, in each cell, the mixture fraction is distributed across the engine cycles following a β-function shaped PDF (Equation 11).

$$P(Z,x,t) = \frac{\Gamma(r+s)}{\Gamma(r)\Gamma(s)} Z^{r-1}(1-Z)^{s-1} \qquad (11)$$

where

$$r = Zp, \quad s = (1-Z)p, \quad p = \frac{Z(1-Z)}{Z'} - 1$$

This function requires the solution of mixture fraction Z itself, for which a dedicated transport equation is introduced, but also of its variance Z'. The two corresponding transport equations are reported as Equation 12 and 13.

$$\frac{\partial}{\partial t}\rho Z + \frac{\partial}{\partial x_i}\rho u_i Z = \frac{\partial}{\partial x_i}\left[\left(D_Z\rho + \frac{\mu_t}{\sigma_t}\right)\frac{\partial Z}{\partial x_i}\right] + S \qquad (12)$$

$$\frac{\partial}{\partial t}\rho Z' + \frac{\partial}{\partial x_i}\rho u_i Z' - \frac{\partial}{\partial x_i}\left[\left(D_Z\rho + \frac{\mu_t}{\sigma_t}\right)\frac{\partial}{\partial x_i} Z'\right] = 2\frac{\mu_t}{\sigma_t}\frac{\partial Z}{\partial x_i}\frac{\partial Z}{\partial x_i} - c_s\rho\frac{\varepsilon}{k}Z' \qquad (13)$$

Once all those variables are computed, it is finally to compute the final turbulent flame speed, input to the G-equation, as follows (Equation 14):

$$S_T = \int_0^1 S_T(\Phi)P(Z)dZ \qquad (14)$$

This final operation allows this model to drive the G-equation through the 'ensemble average' turbulent flame speed, at least with respect to the mixture fraction. The current approach neglects pressure and temperature fluctuations in the averaging process, assuming their cycle-to-cycle variation is sufficiently linear to allow the use of mean values for s_T calculations. In contrast, the mixture fraction displays much higher non-linearity in its effect on s_l. This disparity makes it critical to account for the mixture fraction distribution more strictly than that of pressure or temperature.

1.5. Sub models: flame instability

The last chapter of the theoretical background of the models regards the flame thermo-diffusive instability. It is worth to treat this argument because the hydrogen-air mixture, if lean, leads to such kind of flames. The reason is in the molecular properties of hydrogen, in particular its mass diffusivity, the highest of any other substance in gas state under equal conditions [53]. To illustrate why lean hydrogen-air flames exhibit such distinct characteristics, it is helpful to examine a cross-section of the flame front that separates the unburnt reactants from the combustion products (Figure 2).

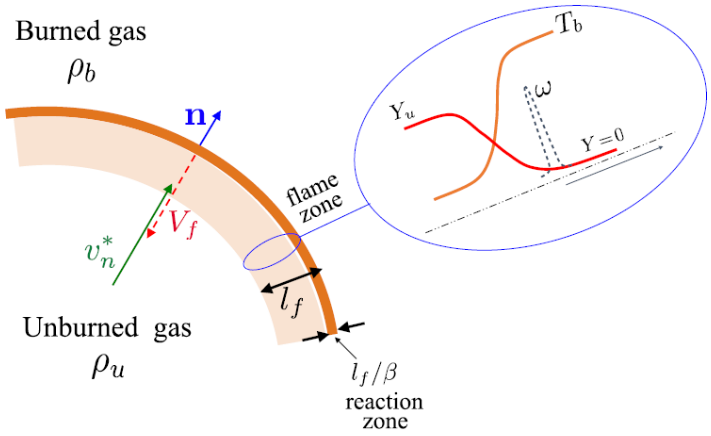

Figure 2: Flame cross section [54].

If the flame, that is the region where reactants are converted to products and where a high thermal gradient occurs because of the exothermicity of reactions, stretches, local gradients of mass and temperature increase. From this point, the flame behaviour is governed by the interplay between two competing physical processes: on one side the reactant species are attracted to the reacting zone, where their concentration is poor; on the other side, flame tends to cool down due to the increased heat exchange towards the fresh gases, enabled by the higher temperature gradient. The number representing this competition is the Lewis number, defined as the ratio between thermal (α) and mass (D) diffusivity (Equation 15):

$$Le = \frac{\alpha}{D} = \frac{\lambda}{\rho c_p D} \qquad (15)$$

For a mixture of multiple gases, it is possible to define an effective Lewis number of the mixture [54]: in the example of hydrogen-air, the correlation in Equation 16 can be used:

$$Le_{eff} = \begin{cases} \dfrac{Le_O + A Le_F}{1 + A} & \text{lean mixture } (\phi < 1) \\ \dfrac{Le_F + A Le_O}{1 + A} & \text{rich mixture } (\phi > 1) \end{cases} \qquad (16)$$

Where the coefficient A depends on the equivalence ratio and the Zel'dovich number β (Equation 17):

$$A = \begin{cases} 1 + \beta(\phi^{-1} - 1) & (\phi < 1) \\ 1 + \beta(\phi - 1) & (\phi > 1) \end{cases} \qquad (17)$$

Based on this expression, it can be inferred that a lean hydrogen-air mixture possesses an effective Lewis number Le_{eff} lower than unity. Recalling the definition of Lewis number itself, this shows that a lean hydrogen-air mixture is more biased towards the mass diffusion. In the problem of the flame response to a stretch, This property renders the flame front more susceptible to the influx of reactants than to the dissipation of heat when subjected to local stretch. As a consequence, where the flame is locally stretched, it tends to accelerate rather than slow down. This is the basis that constitutes the thermo-diffusive unstable behaviour of such flames that, in response to a perturbation (that leads to local stretches), tend to increase such perturbation instead of smoothing it out (as would happen in thermo-diffusive stable flames, where the thermal diffusivity prevaricates the mass one, cooling down the flame and ultimately slowing the perturbation down).

Thermo-diffusive instability, despite suspected to be dominant in lean hydrogen flames, is not the only kind of instability the flames are possibly subject to. Imagining the flame as an infinitely thin surface splitting two regions of gases with different densities, if the surface moves from the less towards the more dense, it is intrinsically unstable. This is the so called Darrieu-Landau instability [55], which necessarily interacts with the mechanisms of the thermo-diffusive one. The reason why not all flames are intrinsically unstable is in fact the stabilization (if present) effect of thermal and mass diffusivities. A nice mathematical description of this is given in the work of Matalon [54], where the simplest interpretation of the flame as a 2 dimensional sheet leads to a linear dispersion relation, indicating that the growth speed of each spectral component of instability perturbation (modelled as a wave) is always positive, thus the instability wave tend to grow. Assuming that the perturbation can be described by Equation 18:

$$f' = Ae^{iky+\omega t} \qquad (18)$$

With A wave amplitude, k wavenumber and ω growth rate, the solution of the related eigenvalue problem leads to the expression, for the growth rate, reported in Equation 19 that, for $\sigma > 1$ as in an expanding flame, is always positive.

$$\omega = \underbrace{\frac{1}{\sigma+1}\left[\sqrt{\sigma^3+\sigma^2-\sigma}-\sigma\right]}_{\omega_{DL}} S_l k \qquad (19)$$

Plotting ω against k, the dispersion relation can be visualized (Figure 3).

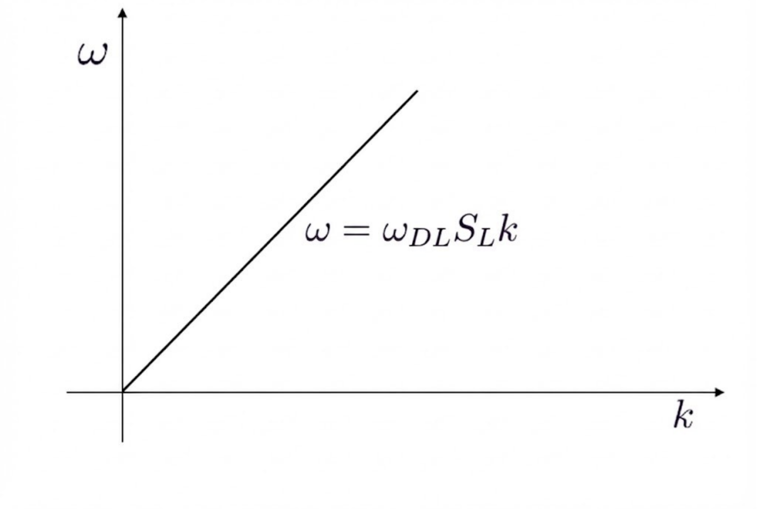

Figure 3: dispersion relation predicted by the Darrieus-Landau theory.

Refining the modelling and including a certain thickness to the flame, thermal and mass transport across such thickness must now be taken into account leading, finally, to a new dispersion relation reported in Equation 20 and plotted in Figure 4.

$$\omega = \omega_{DL} S_L k - \delta_l \underbrace{\left[B_1 + \beta\left(Le_{eff} - 1\right)B_2 + PrB_3\right]}_{\omega_2} S_L k^2 + \ldots \qquad (20)$$

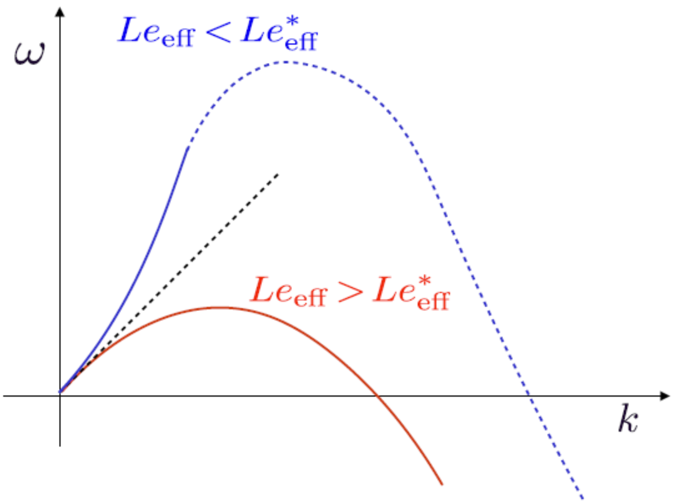

Figure 4: dispersion relations according to the hydrodynamic theory [54]. Two possible shapes are reported, depending on the specific value of the parameter Le_{eff} (solid lines). The black dashed line reports the dispersion relation according to Darrieus-Landau theory.

Interestingly, refining flame physics led to an additional second order component of the dispersion relation, expanding upon the previous model as a higher-order extension rather than a correction of a fundamental error. The thermo-diffusive instability, indeed, should be intended not as a different kind of instability compared to the Darrieus-Landau one, but rather as an expression of a different physical mechanism driving the instability, which is unique and result of many different possible contributions. With this new second order component, the dispersion relation shows the same behaviour for really big wavelengths (smaller wavenumbers k), but for smaller ones it tends to zero and eventually goes below zero, meaning that an unstable perturbation is slowed down: the flame can even be stable. This is a sort of correction of the classical Darrieus-Landau theory application to flame instability, partially explaining experimental observations (flames are generally more prone to be stable rather than intrinsically unstable) but still not so precise in predicting the actual dispersion relation computed from 3D DNS simulations. In fact, other descriptions of the phenomena exists, that are able to give different expressions for the dispersion relation, as the one by Clavin [56] (Equation 21) or Sivashinsky [57] (Equation 22).

$$\omega = \frac{\sigma - 1}{\sigma + 1} S_l k - \delta_l \left[\frac{\sigma}{\sigma + 1}\left(\mathcal{M} + \frac{1}{\sigma - 1}\ln\sigma\right)\right] S_l k^2 \qquad (21)$$

$$\omega = \left[\frac{\beta}{2}(1 - Le) - 1\right] D_{th} k^2 - \gamma D_{th} {\delta_l}^2 k^4 \qquad (22)$$

Nonetheless, the Matalon dispersion relation is, to the aim of this work, the more interesting, because it was chosen as the basis for the selected correlation to correct the laminar flame speed.

The correlation is the one of Howarth [11], who carried out 3D DNS simulations of thermo-diffusive hydrogen-air flames in unstable conditions not so far from the ones encountered in the studied operative points. As told, the correlation is based on the Matalon dispersion relation, and in particular on the parameter ω_2 (see Equation 20), addressed as a representative one for the hydrogen-air flame, where the thermo-diffusive contribution is believed to be dominant on the overall instability (ω_2 serves as the coefficient for the second-order term in the dispersion relation, which emerges once the transport phenomena are accounted for). The laminar flame speed measured from the DNS simulations is then compared to the one computed through 1D kinetic simulations at same conditions; finally, a correlation fitting the dataset is found (Equation 23).

$$\frac{S_{L\,instab}}{S_L} = \begin{cases} e^{0.08\cdot\omega_2} & if\ \ \varphi \geq \varphi_{lim} \\ 1 + 0.47\cdot\omega_2 & if\ \ \varphi < \varphi_{lim} \end{cases} \qquad (23)$$

The fitting was found to better work with two separate fitting functions, depending on the combination of pressure, temperature and equivalence ratio. This condition is expressed through the inequalities of equivalence ratio φ, for which a limit value individuates whether the studied point falls on one side or another of the ω_2 map. Some maps are hereafter reported, for a better visualization (Figure 5).

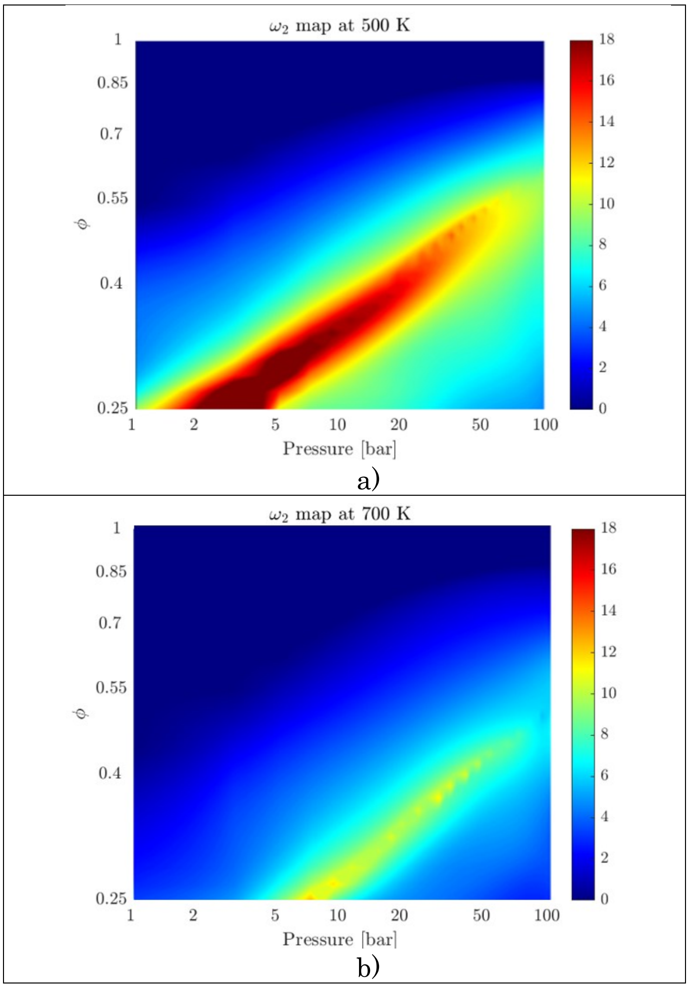
ω_2 map at 500 K

a)

ω_2 map at 700 K

b)

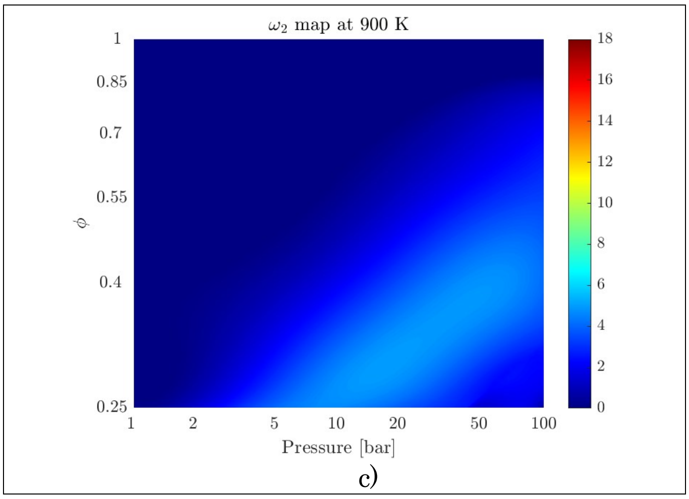

Figure 5: values assumed by the variable ω_2 for 3 different temperatures, in a bi-logarithmic map [22].

Equation 24 delineates the locus of the maxima of this function for various temperatures.

$$\varphi_{lim} = (0.3475 - 0.000325 \cdot T) \cdot p^{0.1425+0.000225 \cdot T} \qquad (24)$$

It should be noted that this is a variant to the original expression individuated by Howarth in its work. This modification was made necessary after a map of ω_2 was computed and extended beyond the ranges tested in Howarth work, because the original correlation to individuate the pressure ridge was noticed not to hold anymore over 700K of unburnt temperature. The reason for this discrepancy is the empirical nature of the correlations. In the work by Howarth, investigations were limited to temperatures of 700K, where the original correlation proved sufficient. However, by extending the range to higher temperatures, as in this study, it became necessary to adapt the correlation to these new boundaries.

Again, Howarth's one is only one of the possible relations to correct the unstretched laminar flame speed, but it is here judged the best because of the vicinity to motoring conditions and the accuracy, as it is derived form 3D DNS simulations. Other correlations available, namely the ones in references [10], [58], are based on 2D DNS, and a significant scaling is shown to exist between 3D and 2D DNS fitted data of laminar flame speeds [11]. However, the scaling is left to the user as a calibration, introducing an unwanted leverage to artificially recover the numerical-experimental agreement.

Around the final stages of this activity, Equation 23 was introduced in the framework, through an external computation of ω_2 values that were thus interpolated in function of pressure, temperature, EGR and equivalence ratio. The framework, thus, remained almost unchanged, having only an additional intermediate step between laminar and turbulent flame speeds computations, in which the unstretched laminar flame speed is incremented by the correction factor proposed by Howarth. This final "stretched" laminar flame speed is subsequently integrated into the turbulent flame speed calculation, following the established methodology. It is important to emphasize that, given the current modelling approach, the correlation does not isolate the thermo-diffusive contribution alone; rather, it inherently accounts for the Darrieus-Landau instability that naturally emerges within the 3D DNS simulation framework. That's why, in general, the term flame instability rather than thermo-diffusive instability, will be preferred in the following.

A final relevant quest is posed on the applicability of such approach in presence of turbulence. Some authors ([11], [59]), in fact, claimed that there are conditions at which a mutual interaction between turbulence and instability can further enhance the flame de-stabilization, in turn further accelerating the turbulent flame speed. The adopted approach, in fact, relies on the hypothesis that turbulence and instability are decoupled phenomena. This hypothesis may hold, but only under specific circumstances, usually not close to engine operations. To better explain these concepts, it may be useful to refer again to the dispersion relation, and include in the same graph the turbulent spectrum, obtaining the Figure 6. The wavelength of the turbulent spectral component is imagined included inside the wavenumber k in the x-axis and the eddy turnover time in the growth rate ω in the y-axis.

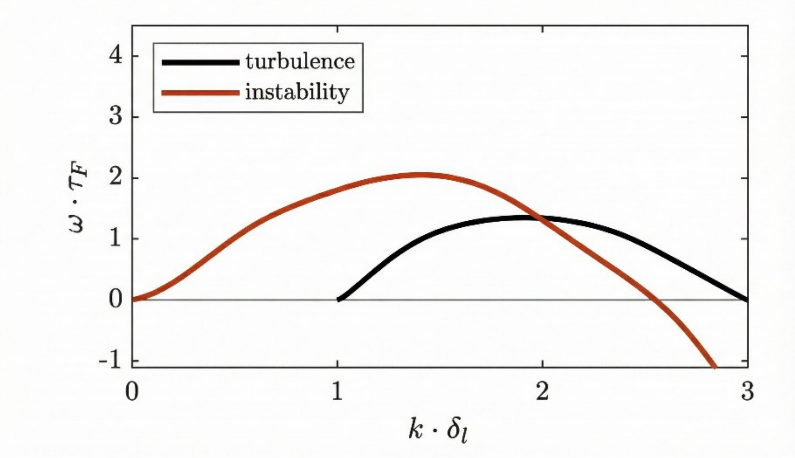

Figure 6: instability and turbulence spectrum. This representation is not physically accurate, and only describes qualitatively a possible way for the two spectrums to overlap. In the turbulent spectrum, Kolmogorov scale is towards right (high wavenumbers) and integral length scale towards left.

From this perspective, the coupling or decoupling of physical phenomena is made clearer: if the two spectra do not intersect, decoupling can be assumed, as turbulent wrinkling and instability-induced wrinkling occur at distinct scales. To discuss the possibility of scale separation, it is first necessary to delineate the instability spectrum. This is not a trivial task, as it lacks a unified theoretical framework and relies primarily on experimental and numerical observations.

Nevertheless, it is possible to identify the largest possible instability wavelength as the domain size, which represents the physical spatial limit constraining the flame. Beyond this, Berger et al. [60] noted in a 2D DNS study the recurrence of "finger-like" structures characterized by a specific maximum wavelength. It was observed that no complex structures develop beyond this limit, which was identified at approximately 25 times the laminar flame thickness δ_l. While 3D effects and the presence of turbulence may quantitatively alter this threshold, the hypothesis of a maximum size for instability-driven structures remains compelling, with a suggested order of magnitude between 10 and 100 δ_l. As for the lower limit, various measured dispersion relations show that the cutoff occurs at roughly two times the laminar flame thickness. Physically, it is reasonable to accept that wave components with scales close to the flame thickness are unable to effectively wrinkle the front; at such scales, the perturbation results in a slight local strain rather than a corrugation capable of increasing the flame surface area and its subsequent propagation speed.

Establishing these boundaries allows for a detailed discussion on scale separation. One possibility is that the turbulence spectrum is entirely finer than the laminar flame thickness. In such a case, the turbulence would be decoupled from the instability; however, this scenario likely coincides with the "well-stirred reactor" regime. A partial decoupling, still consistent with the adoption of flamelet-based models, is instead allowed in the thickened flame regime, where only some of the turbulent scales are smaller than the laminar flame thickness, so out of the instability spectrum. In this regime, intense small-scale turbulence tends to thicken the flame front, potentially dampening cellular instabilities by homogenizing the local gradients that drive them.

The other possibility for decoupling is that the finest turbulence scales capable of wrinkling the flame are larger than the largest instability structures (the aforementioned 10–100 δ_l). However, it is highly unlikely that the smallest turbulent scales can obey this limit in motoring conditions. Given that the Karlovitz number relates to the square of the ratio between the flame thickness and the turbulent scale ($Ka \approx \left(\frac{\delta_l}{\eta}\right)^2$), requiring the smallest turbulent scales to be 10 to 100 times larger than the flame thickness translates into Karlovitz numbers between 1/100 and 1/10000. Such values are exceptionally low for engine practice, suggesting that in most applications, turbulence and instability are at least partially coupled.

Stated that these phenomena are likely coupled, a unified modelling approach remains difficult to find. Howarth et al. proposed an empirical correlation from 3D DNS data, linking the turbulent unstable flame speed to 1D kinetic laminar speeds by incorporating the instability parameter ω_2 alongside turbulent intensity u' and dissipation ε (Equation 25).

$$\frac{S_S}{S_F} = f_{S,S} = 1 + 0.26\exp(-0.038\omega_2)\cdot\left((u'^3\delta_l)/(s_F^3 L_t)\right)^{0.25} \qquad (25)$$

However, such models are often narrowly tailored to their calibration datasets. For instance, this correlation tends to predict a flame speed enhancement ratio of unity as ω_2 approaches zero, implying that in the absence of instability, turbulence provides no enhancement to flame propagation: a result that is physically inconsistent.

Given the aforementioned complexities and the current lack of comprehensive data required to fully describe the interaction between turbulence and intrinsic instabilities, the adopted modelling strategy represents a calculated compromise. By primarily utilizing a laminar flame speed correction, hydrogen-specific instability effects are incorporated while maintaining the assumption of weak turbulence-instability coupling. However, to account for the physical influence of turbulence on these phenomena, an additional criterion derived from experimental observations is employed. This allows for the systematic dampening of the instability contribution as the flame approaches the thickened regime, thereby ensuring a more physically consistent representation without introducing the prohibitive uncertainty associated with applying complex empirical correlations outside their original calibration bounds.

Delving into the model details, Matalon et al. [61], [62] observed that, while increasing the turbulence intensity, the turbulent wrinkling tends to dominate the flame instabilities. More recently, Berger et al. [63] noted the dampening effect of the turbulence on the flame instability in DNS simulations of a slot burner. In [64], [65], Bradley introduced a method to quantify the relative contributions of turbulence and instability to the flame wrinkling, defining a parameter known as Karlovitz stretch factor. As per Bradley's formulation, Equation 26 represents this factor.

$$K = 0.25\cdot\left(\frac{u'}{S_l}\right)^2\cdot {R_l}^{-0.5} \qquad (26)$$

The terms that appear in the equation are turbulent intensity u', laminar flame speed S_l and turbulent Reynolds number $R_l = \frac{u' l_t}{\nu}$, where l_t is the integral length scale and ν the kinematic viscosity.

In [64], [65], Bradley et al. identified the "regime of laminar instabilities and mild turbulence" for $K \leq 0.1$ and the "fully turbulent regime" for $K > 0.1$. In the former, the instability effect is

significant. Conversely, in the latter, the turbulence wavelengths dominate and intensify the flame wrinkling, thus making the flame instability-induced wrinkling negligible.
In order to obtain a smooth transition between the two regimes, an S-shaped function is introduced and reported in Equation 27. It guarantees continuity in the transition from S_l to $S_{l\ instab}$.

$$S_{l_{corrected}} = S_l + \frac{1}{e^{100(K-0.1)} + \frac{1}{S_{l_{instab}} - S_l}} \qquad (27)$$

Figure 7 reports an example of blending, with this function, between two arbitrary laminar flame speeds of 4 and 6 m/s.

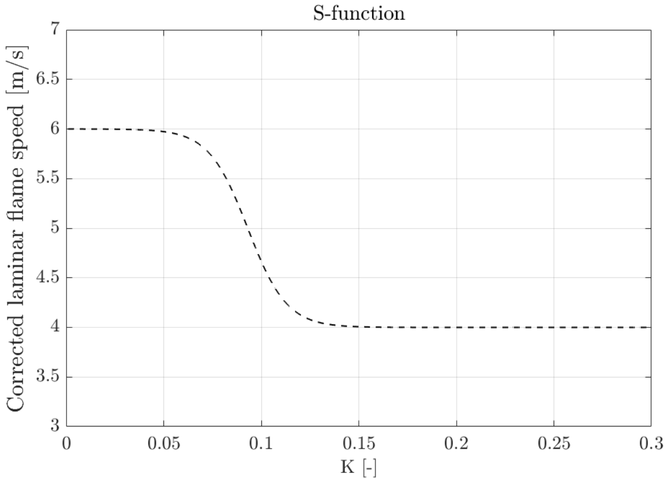

Figure 7: S-function behaviour as a function of the Karlovitz stretch factor K. As an example, values of S_l equal to 4 and 6 m/s are considered for the blending.

The parameter 100, which appears in Equation 27, is used as a calibration constant and governs the width of the ‘S’. A much higher value leads to a step function. The other parameter, 0.1, is the threshold value for the Karlovitz stretch factor, acting as a centre for the ‘S’.

A last note is given on the proper identification of the combustion regime, already nominated sometimes in the dissertation. In fact, even this aspect is non trivial when dealing with lean hydrogen-air flames. The reason of this stays again in the high hydrogen mass diffusivity, lowering the effective mixture Lewis number. In fact, an underlying assumption of the classical definitions of Karlovitz and Damköhler numbers, thus of combustion regimes, is unity Lewis number. This hypothesis clearly falls down in the case of lean hydrogen combustion: in DNS studies carried out by Aspden et al. [66] it has been observed, in fact, that changing flame conditions (modifying together equivalence ratio and turbulence) in a way to keep the Karlovitz and Damköhler, as classically defined, constant, the flame visually appeared to belong to flamelet or thickened flame regimes. An attempt to modify the classical definitions, following the approach proposed by Aspden et al., is made throughout this work.

Chapter 2. Numerical framework validation and preliminary engine study.

The first step of this work consisted in evaluating the robustness of the selected framework. Care was thus not posed on the accuracy of the results, but rather on the predictive capabilities of the framework, observing in particular its ability to catch the same trend that was observed in experiments for varying operating conditions. The available experimental dataset is particularly suitable for this aim: it consists of 11 operating conditions at 1500, 2000, 2500 and 3000 rpm, with each engine speed running with equivalence ratio $\varphi=0.4$, 0.6 and 0.8, except for the case at 1500 where only 0.4 and 0.8 were present. The engine studied presents a direct injection system, as common in hydrogen engines, with two injectors directly facing the combustion chamber. However, the relatively low maximum engine speed and the dual-injector configuration allowed for low-pressure delivery, ensuring that flow velocities did not significantly exceed the speed of sound. This allowed for some simplifications of the framework, and didn’t force to use expensively fine meshes and timesteps for such a preliminary activity. A description of the experimental apparatus and the engine studied follows.

2.1. Experimental campaign

The experimental activity starts with the adaptation of the original engine to H_2 injection and combustion [67]. The production Diesel engine, namely Lombardini 15LD500, was developed nearly 20 years ago for several light duty applications. Table 1 provides details of the engine specifications before and after the conversion.

Table 1: engine specifications

N° of Cylinders	1
Valves per cylinder	2
Alimentation	Naturally aspired
Bore	87 mm
Stroke	85 mm
Displacement	505 cm^3

Compression ratio	19:1 (Diesel), 10:1 (Hydrogen)
Max Power	9 kW @ 3600 rpm (Diesel), 9.14 kW @ 3000 rpm (Hydrogen)
Max Torque	31 Nm @ 2000 rpm (Diesel), 32.7 Nm @ 2500 rpm (Hydrogen)
Combustion	CI (Diesel), SI (Hydrogen)

The conversion to H_2 involves the adoption of two low-pressure injectors (operated at 6 bar), a spark-plug for mixture ignition and a reduction of the geometric compression ratio (CR) from 19:1 to 10:1. The CR reduction is achieved by a broader piston bowl, which is shown in Figure 8, and inserting a spacer between crankcase and cylinder.

Figure 8: Modified piston bowl for hydrogen operations [68].

In order to mount the two H_2 injectors, an external portion of the engine head is flattened. Figure 9 reports the cylinder head with the additional components used for the conversion.

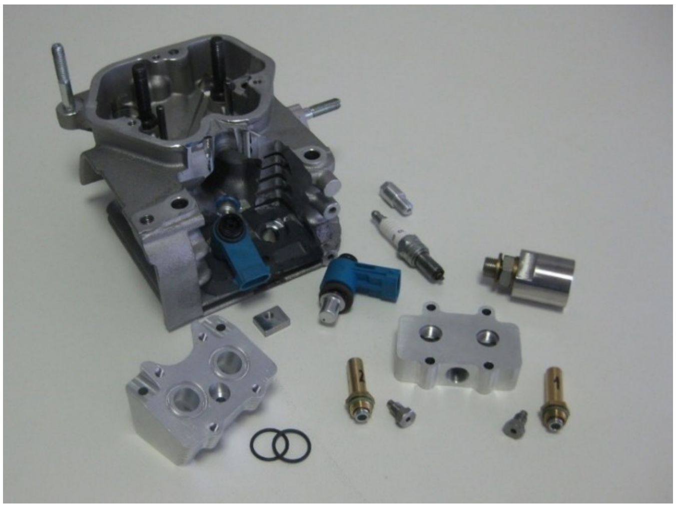

Figure 9: modified head with additional components for hydrogen operations [68].

Table 2 resumes the experimental operating conditions replicated by the numerical simulations.

Table 2: tested operating points.

Test N°	φ	SOI [° CA bTDC]	Ignition [° CA bTDC]	p H_2 [bar]	T H_2 [°C]	H_2 MFR [g/s]	Speed [RPM]	Power [kW]
1	0.80	210	-4.5	5.81	17.2	0.24663	2995	9.14
2	0.80	210	-4.5	5.83	17.5	0.21957	2501	8.55
3	0.80	220	-9	5.86	19.1	0.17173	2008	6.52
4	0.80	220	-9	5.87	19.5	0.13253	1549	4.98
5	0.60	200	3	5.85	20.2	0.18223	2995	6.15
6	0.60	200	3	5.86	20.6	0.16007	2507	6.04
7	0.60	200	3	5.89	20.7	0.12343	2011	4.62
8	0.40	200	12	5.88	21	0.12600	3003	3.28
9	0.40	200	12	5.89	21.1	0.10967	2505	3.82
10	0.40	200	12	5.91	21.3	0.08727	2015	2.94
11	0.40	200	12	5.92	21.3	0.06230	1505	1.97

A schematic representation of the test rig is depicted in Figure 10. The complete system is positioned on the test bench and the engine output shaft is connected to a “Borghi e Severi” eddy current dynamometer, controlled by an API microprocessor unit. In order to obtain the indicated cycle, pressure is measured by the Kistler 6052C piezoelectric high temperature sensor, with a nominal sensitivity of nearly 20 pC/bar and a pressure range of 250 bar, featuring a maximum linearity error of ±0.4% of the full-scale output. The crankshaft position measurement relies on the 365X AVL angle encoder with ±0.1°CA precision. The signals of in-cylinder pressure sensor and encoder are processed by the VL IndiCom 1.2 acquisition code, in order to obtain the indicated cycle. The electronic control of injection and ignition is entrusted to the engine control unit (ECU), namely the Motec M400. In the exhaust line, the Bosch LSU 4.2 wide-band lambda sensor is installed to evaluate the equivalence ratio. Due to the strong sensitivity of the lambda sensors to H_2 operation, three probes are alternated during the tests to keep the measurement accuracy within ±5%. To reduce the uncertainty of the data, φ values are verified by mass flow rate data of both intake air and H_2. Fuel and intake air mass flow rates are obtained by the Bronkhorst High-Tech EL-FLOW mass flow meter. To calibrate the lambda sensors, a suitable range of mixture qualities is firstly individuated based on the engine conditions. Then, a mixture with the highest equivalence ratio of the defined range is imposed in the engine with the help of the mass flow meters. Given the voltage signal of the lambda sensor, the corresponding output value is scaled to match the imposed one. This procedure is repeated at steps of 0.1 till the lower equivalence ratio and the measure is checked for different days to account for the specific ambient conditions. The calibration is considered satisfactory if the measure remains within a ±5% error without adjustments for all the days. The test bench also monitors the temperatures of intake air, exhaust gas and injected H_2 by thermocouples. The Beckman 951 chemiluminescence analyser is used to measure NO_x emissions, which is characterized by an accuracy of ±0.5% of full scale. Gases are sampled by a probe installed in the exhaust line. Further details on the experimental apparatus can be found in Ref. [68].

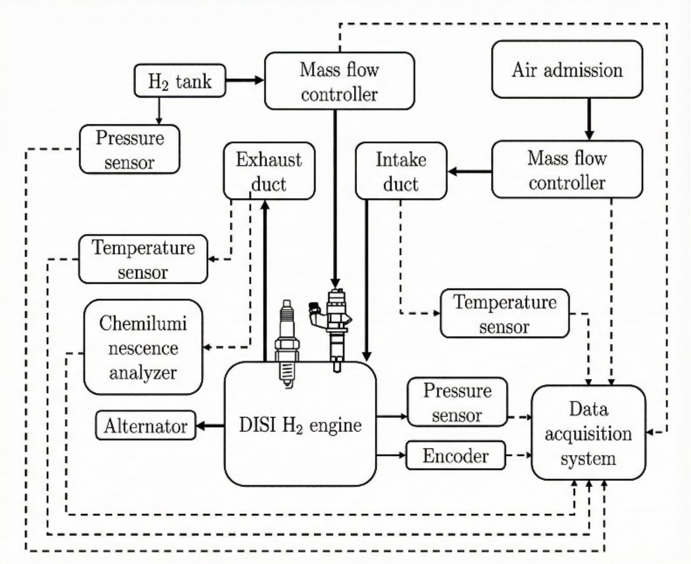

Figure 10: scheme of the test rig.

2.2. 3D CFD study

As for the numerical framework, it is basically the one detailed through Chapter 1, without the addition of instability modelling. The mesh size ranges between 1 and 2 mm in the core. Ad-hoc refinements are carried out around the spark-plug (the cell size is halved). At the solid walls, a 0.3 mm prismatic layer is imposed. With this setup, the maximum number of cells at Bottom Dead Centre (BDC) is around 320000. The adopted numerical grid is reported in Figure 11.

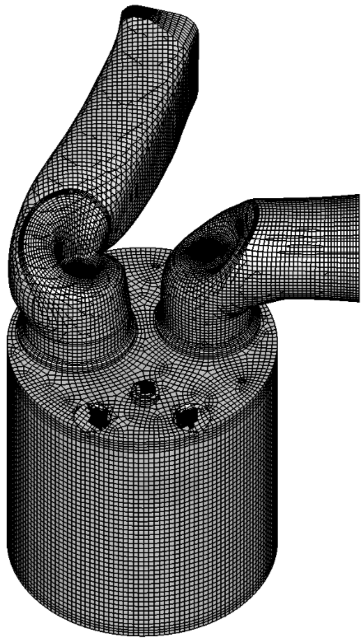

Figure 11: Computational mesh of the fluid domain [19].

As for the wall temperatures, they are a guess based on previous experiences because of the lack of specific heat rejection data. Selected values are reported in Table 3.

Table 3: wall temperatures at domain boundaries.

Combustion dome	523K
Piston crown	523K
Cylinder wall	453K
Intake valve stem and port	320K
Intake valve face	420K
Exhaust valve stem	720K
Exhaust valve face	720K
Exhaust port	473K
Spark plug	600K

As for the remaining setting, the time step is chosen equal to 0.05° CA (corresponding to 2.77×10^{-6} s at 3000 rpm, 3.33×10^{-6} s at 2500 rpm, 4.16×10^{-6} s at 2000 rpm and 5.55×10^{-6} s at 1500 rpm) during valves opening and closing, injection and combustion, while 0.1° CA (corresponding to 5.54×10^{-6} s at 3000 rpm, 6.66×10^{-6} s at 2500 rpm, 8.32×10^{-6} s at 2000 rpm and 1.11×10^{-6} s at 1500 rpm) is adopted in the rest of the cycle. Constant values are adopted for pressure and temperature on intake and exhaust boundaries, with temperature values available from the experiments. The exhaust pressure is set equal to the atmospheric one. The intake pressure is calibrated to match the experimentally-derived cycle-averaged trapped air mass. The mass flow rate condition imposed at the H_2 inlet boundary is the trapezoidal law described in the following paragraph, dedicated to the particular injection system.

Since preliminary experimental analyses revealed a relevant charge stratification, as discussed in Ref. [69], caps reported in Figure 12 are mounted on the injector tips to guide the hydrogen jets in order to improve mixture homogeneity.

Figure 12: injectors caps [70].

The orientation of the caps adopted in this analysis to favour the charge homogeneity is proposed in Figure 13, where the orientation on different planes is illustrated. Further details can be found in Ref. [71].

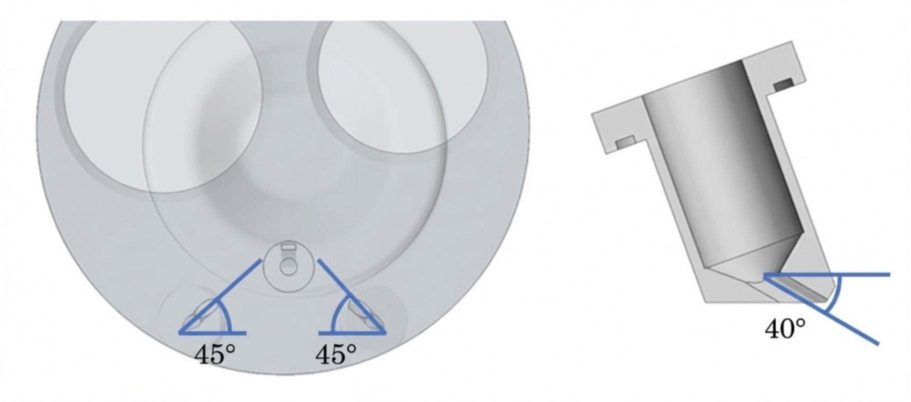

Figure 13: injector caps characteristic angles [19].

Because of the particular geometry of injector caps, the possibility to simplify the injector geometry, with consequent relevant savings of computational time, was explored. In-cylinder simulations include part of the internal portion of the H_2 injector, characterized by an annular orifice. This implies a high-resolution grid (with a characteristic cell size in the order of 10 μm, as in Ref. [72]) needed to discretize the internal nozzle annular channel. In order to limit the CFL number (which is already critical considering that the H_2 flow is sonic), small volume cells lead in turn to reduced time-step values, with a further increase of the computational cost. In addition, since H_2 injection occurs in the small volume between nozzle and cap as visible in Figure 14, such volume should be meshed as well.

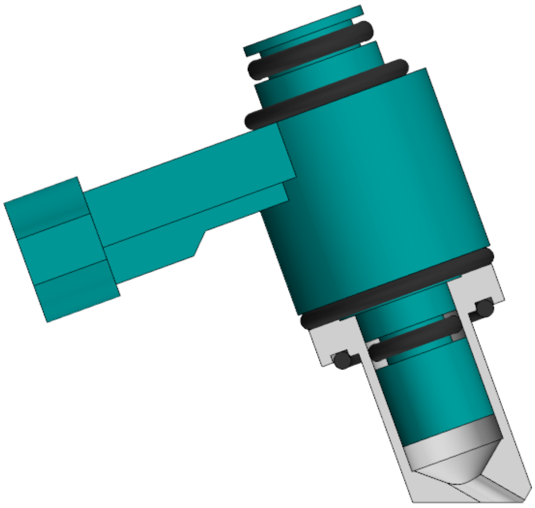

Figure 14: injector-cap assembly [19].

Therefore, preliminary vessel simulations are carried out to evaluate the possibility to simplify the computational domain in proximity of the injector. The elimination of both the inner portion of the injector and of the cap volume prevents the use of very small cells and time-steps. The adopted numerical setup for the vessel simulations is presented at first, then results are shown.

2.3. CFD vessel simulations

3D-CFD vessel simulations consist in test cases characterized by a simplified geometry compared to the cylinder one, in order to facilitate and speed-up the analysis. In particular, the combustion chamber volume is included in the simplified form of a fixed flat-piston cylinder (with mass exchange possible only via the H_2 inlet) with no valves. Moreover, the geometrical symmetry is exploited, thus only one of the two injectors is included and half of the cylinder is considered. Simplifications on the chamber are allowed as the attention is focused on the injector only. Two configurations are tested and visible in Figure 15: the first one (a) with the complete injector geometry and the second one (b) including only the cap hole.

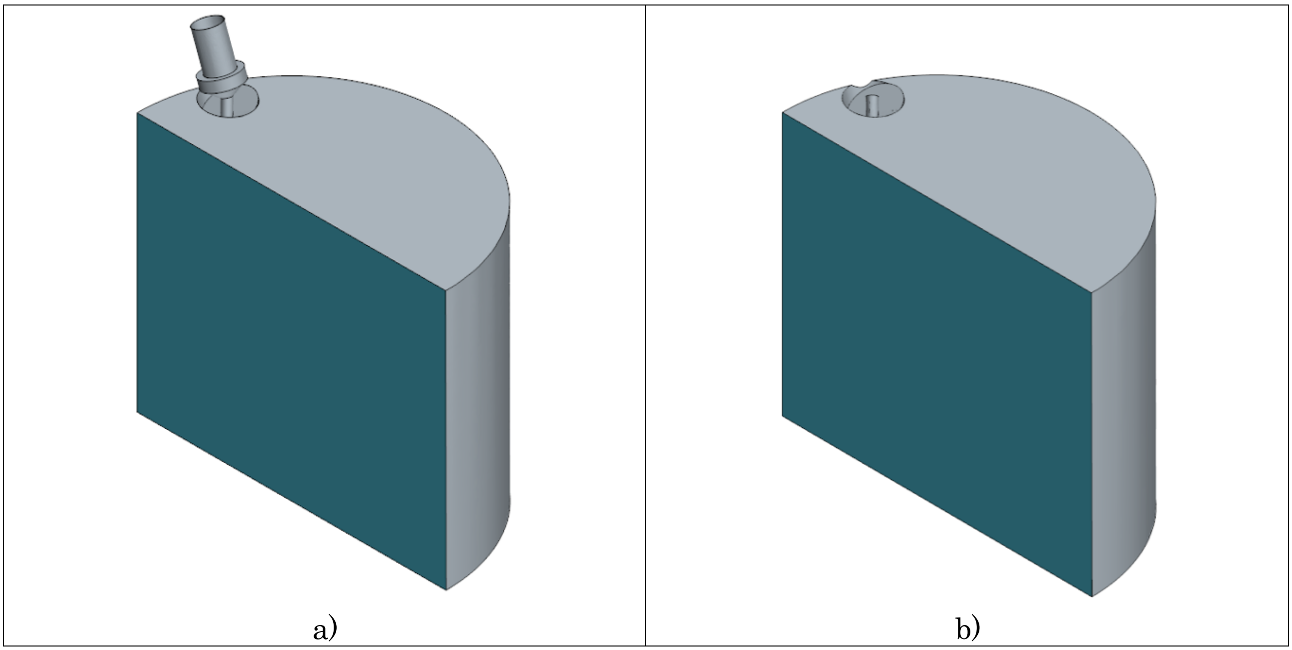

Figure 15: vessel with original a) and simplified b) injector [19].

Figure 16 shows the section downstream of the inlet which is considered to monitor the average temperature and the hydrogen mass flow rate. The same section is used for both the simplified version and the full-geometry one, as it can be noticed comparing Figures 16 a) and b).

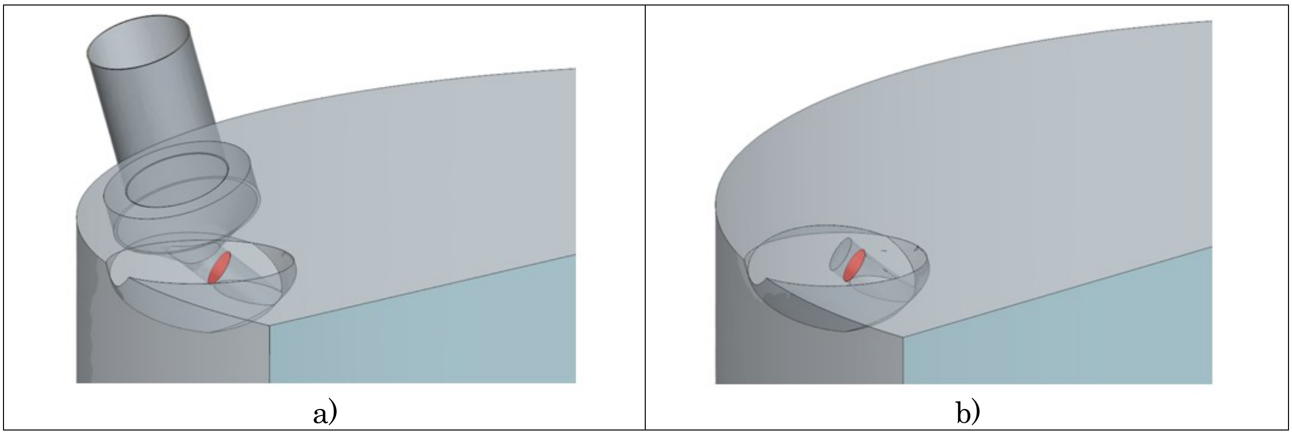

Figure 16: control section across the injector cap hole [19].

Simulations are performed using SIMCENTER STAR-CCM+, licensed by SIEMENS. The Realizable k-ε turbulence model is used, with a low- Reynolds approach, despite the in-cylinder simulations are carried out by the k-ε RNG model. The reason is that the low-Reynolds version of the RNG model is not available in STAR-CCM+, thus the most similar model is adopted. Moreover, in a previous study conducted by Pavlovich [73], it was observed that when simulating supersonic jets in open vessels, also the Realizable k-ε turbulence model is able to effectively capture the flow characteristics. In the light of the sonic/supersonic velocity and the Joule-Thomson effect, the fluid is simulated as a real gas, via the Soave-Riedlich-Kwong model. At the hydrogen inlet boundary, an experimentally derived trapezoidal injection law is imposed for the mass flow rate, while the H_2 total temperature is 293 K. The same mass flow rate and total temperature are applied to both the configurations. In order to select the initial vessel pressure, the actual injection process occurring in the engine is investigated to verify the presence of a choked flow for the whole injection duration of each condition. For the purpose, the first operating condition of Table 2 is considered as it is the most critical one, having the greatest injected mass and the lowest available time before combustion (because of the highest engine speed). As a result, the injection terminates in proximity of the TDC, with a high in-cylinder back-pressure. In order to confirm the choked flow, the critical static pressure below which a sonic flow verifies is calculated as in Equation 28, using the throat section and the injector inlet pressure and temperature, p_{inlet}, as the inlet total pressure and k as the ratio of the specific heats.

$$p_{crit} = p_{inlet}\left(\frac{2}{k+1}\right)^{\frac{k}{k-1}} \qquad (28)$$

Figure 17 shows the H_2 mass flow rate, the critical pressure and the experimental in-cylinder pressure for case 1 of Table 2.

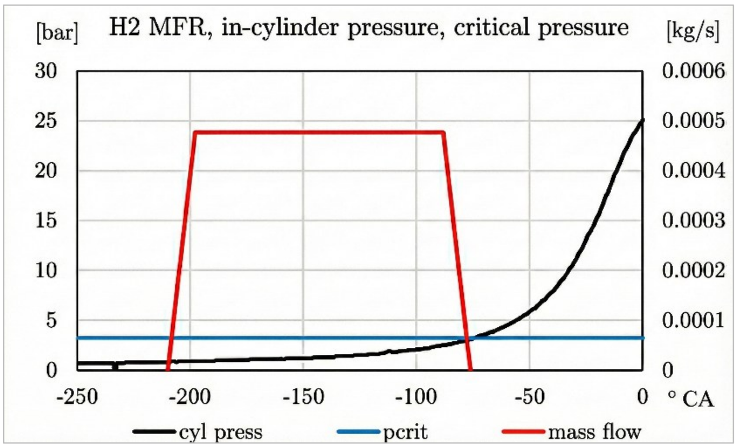

Figure 17: mass flow rate, critical pressure and cylinder pressure for the studied case [19].

From the image, is it possible to observe that the entire injection (apart from the very last CAs) takes place at sonic conditions, terminating immediately after chamber pressure rises above p_{crit}. This is also true for the other conditions in which, as previously anticipated, injection terminates even earlier. Since the injector always operates with choked flow, the injection flow is independent of the downstream condition. Therefore, the chamber pressure to be adopted in the preliminary vessel simulations discussed in the present paragraph is set to an arbitrary constant value (equal to 2 barA) below the critical pressure. Wall temperatures are set to 300 K, the adopted timestep is 5×10^{-6} s and the characteristic mesh size is 0.5 mm. Localized mesh refinements of 0.2 mm are introduced around the injector in both the tested configurations. Figure 18 shows the trapezoidal mass flow rate (dotted line) imposed at the inlet boundary of both the tested configurations: it is almost perfectly superimposed to the hydrogen mass flow (red line) recorded at the monitoring boundary of case b.

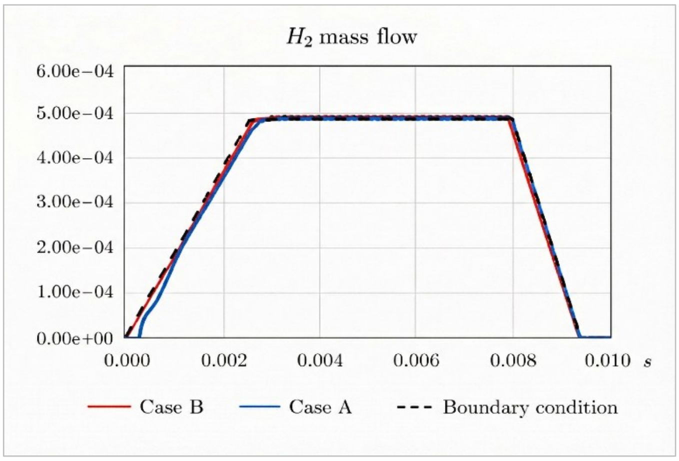

Figure 18: mass flow rates across transverse control sections and at boundary [19].

The mass flow rate for the case a shows a little delay in the early phase due to the time needed to fill the fluid volume between injector and cap. Since such delay is almost irrelevant, the impact of the injector simplification is considered negligible. The total temperature is almost entirely conserved from the original to the simplified inlet boundary, since the heat losses in the region eliminated from the configuration b are negligible. Therefore, the static temperature on the monitored section is very close between case a and b. This result further justifies the geometrical simplification. Since the software used for the in-cylinder simulations needs the hydrogen static temperature at the inlet (instead of the total one), a trapezoidal law is derived from the results of Figure 19 and it is the dashed line reported in the same figure.

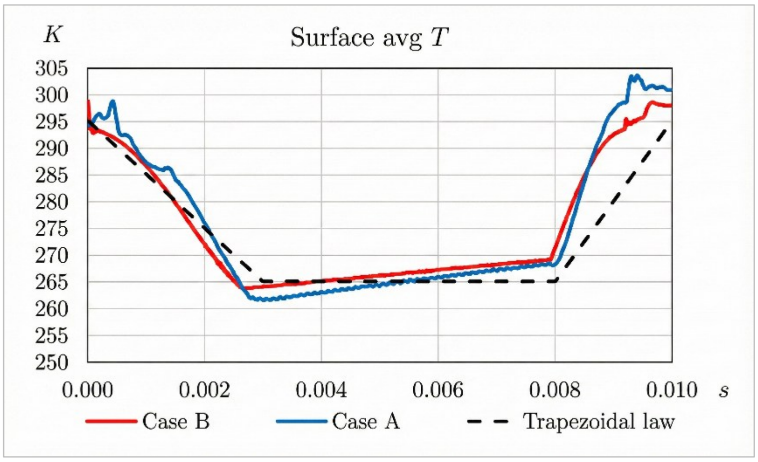

Figure 19: hydrogen injector inlet static temperature [19].

This is adopted in the in-cylinder simulations described in the next paragraph. As a further confirmation that it is possible to simplify the injector geometry without penalizing the quality of the results, the fuel concentration distribution is reported in Figure 20 during the injection process for both the original geometry and the simplified one. The distribution is similar between the two configurations.

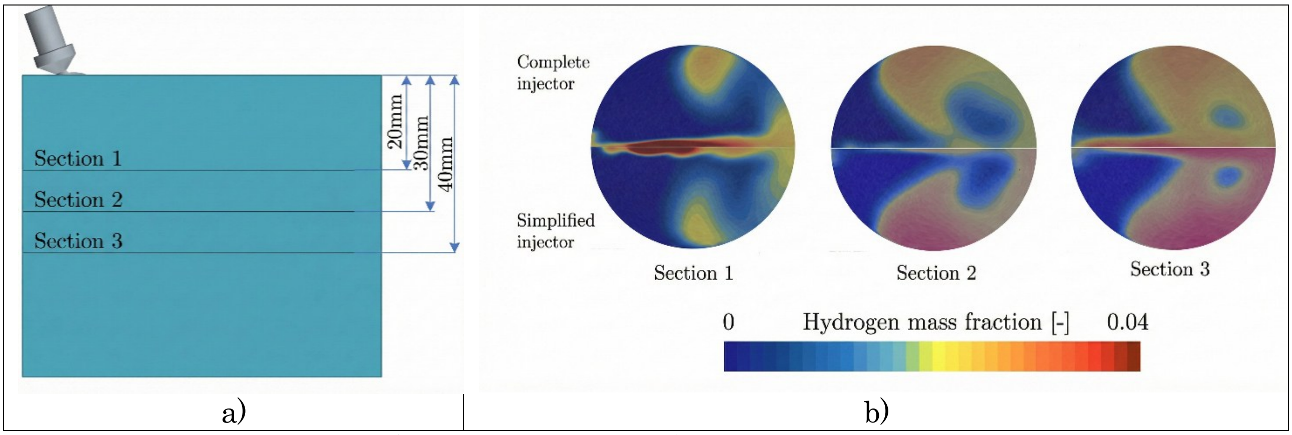

Figure 20: measurement stations a) and resulting sections b), highlighting similar hydrogen distribution among configurations [19].

2.4. 3D CFD combustion results

In order to eliminate the influence of the initial conditions, multiple cycles are run for each investigated condition. For brevity, only the results of the last cycles are proposed in the following. The investigated operating points are characterized by the set of equivalence ratio and engine speed values presented in Table 2.

Before considering the hot portion of the cycle, attention is focused on the mixture preparation. The latter is strongly influenced by the flow field. The swirling motion inherited from the original Diesel operation and due to the intake port shape is clearly visible in Figure 21, where the flow field is reported close to the TDC. The resulting intense flow field is able to deviate hydrogen jets, as shown in Figure 22. H_2 is carried around the chamber and this limits a homogeneous mixing with the air.

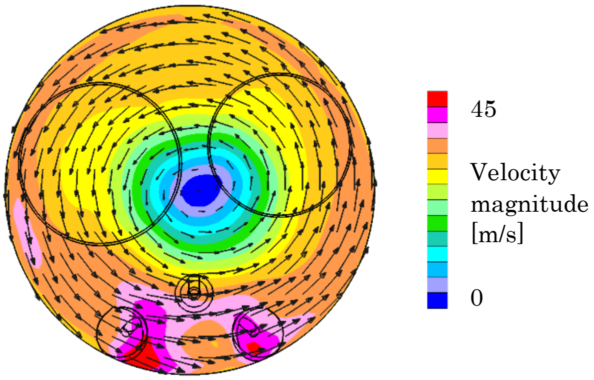

Figure 21: velocity field at 700° CA [19].

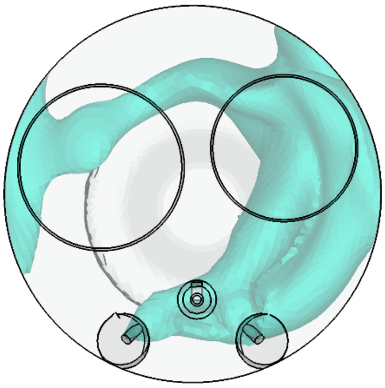

Figure 22: the iso-surface at φ=1 shows the impact of the swirl motion on the distribution of the hydrogen plumes for the case at φ=0.8 and 3000 rpm [19].

The consequence is a peculiar tendency of the investigated conditions to form regions of rich and lean mixture at the opposite sides of the combustion chamber as visible in Figure 23, which shows a comparison between the different equivalence ratios at 3000 rpm. In Figure 24, the equivalence ratio probability density functions (PDFs) of the same cases show that the inhomogeneity increases with the average φ on equal engine speed and nearly equal injection start. This is motivated by the reduced mixing time for longer injection durations. The same comparison at 1500 rpm reveals an opposite trend. In fact, in Figure 25, φ=0.8 case is characterized by a more homogeneous mixture than the φ=0.4 one. Such behaviour is related to the short injection duration that characterizes φ=0.4 cases. Since hydrogen is carried by the flow field around the chamber and the injection is short, fuel concentrates just in a limited sector of the cylinder. Increasing φ and thus the amount of fuel, the latter is more distributed along the circumferential direction, as shown in Figure 26, promoting a more homogeneous mixture. This effect becomes more relevant at 1500 rpm than the one related to the reduction of time available for the mixing.

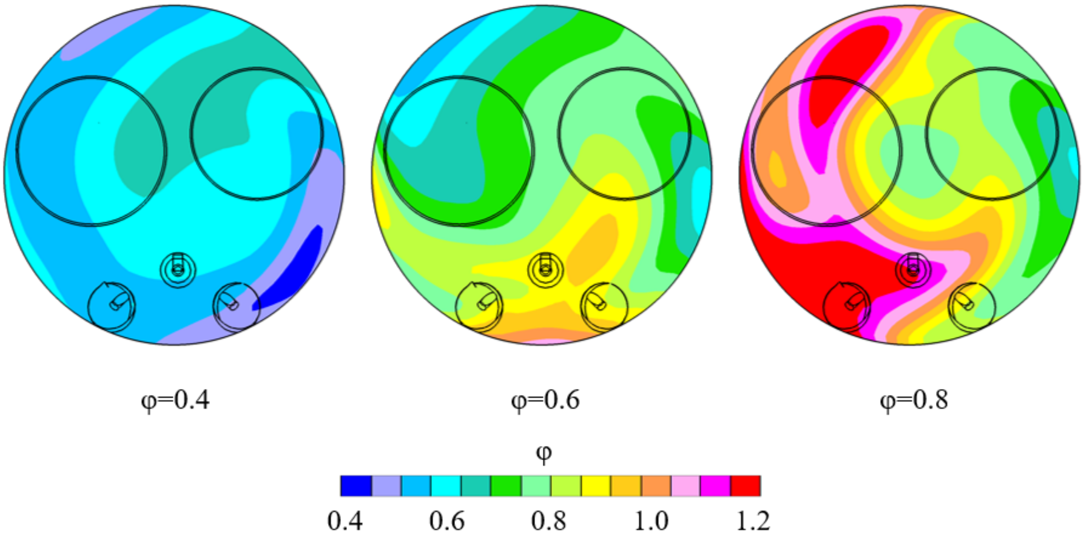

Figure 23: equivalence ratio at 700° CA for the 3000 rpm case [19].

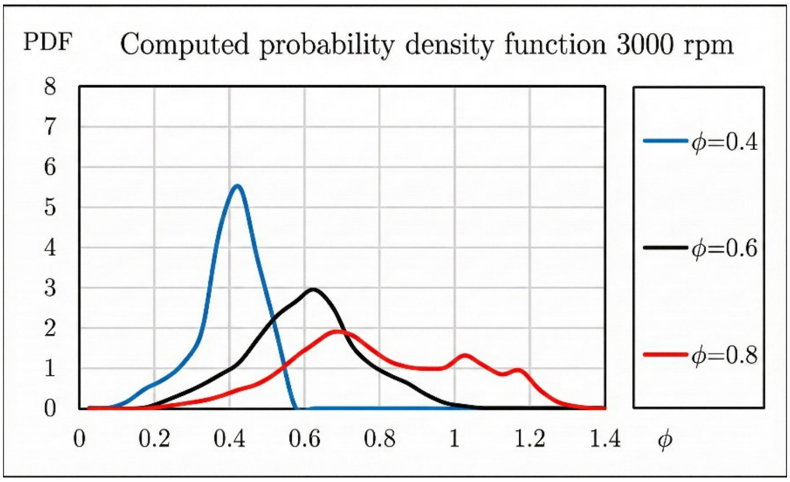

Figure 24: probability density function of φ for all the equivalence ratios at 3000 rpm [19].

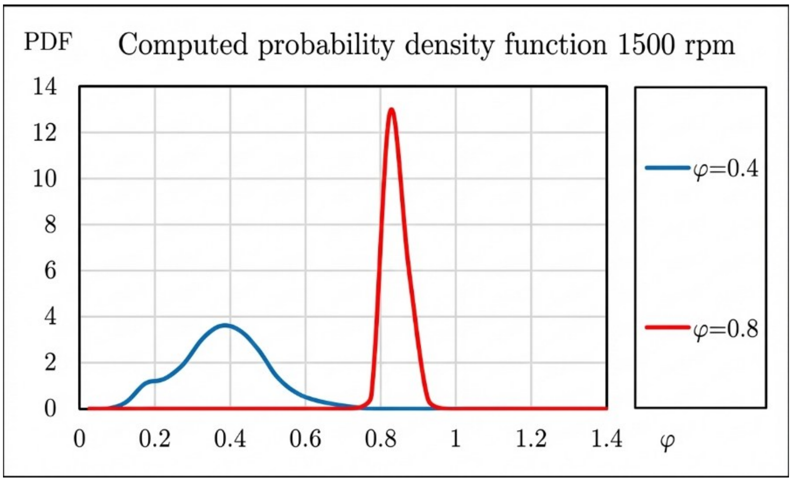

Figure 25: probability density function of φ for all the equivalence ratios at 1500 rpm [19].

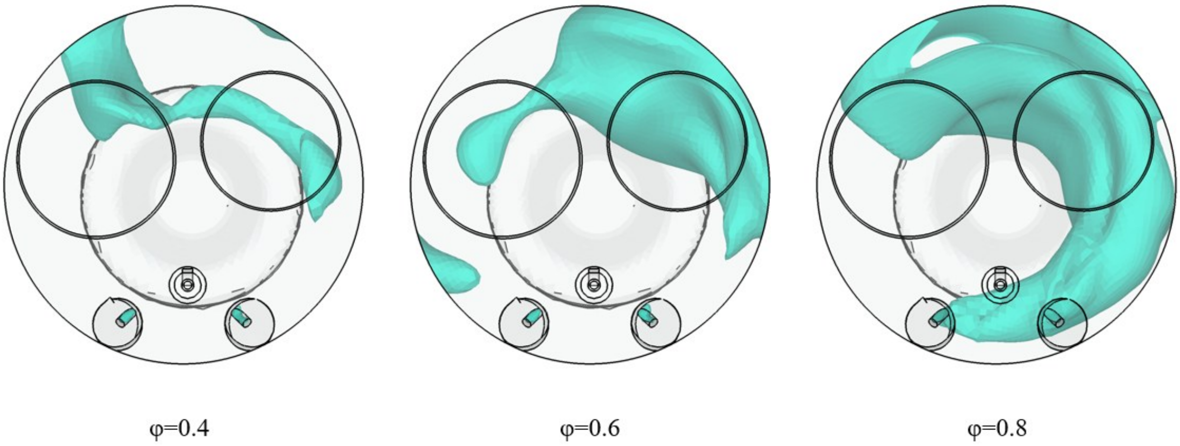

Figure 26: φ=1 iso-surface at the EOI for all the equivalence ratios at 3000 rpm [19].

Considering the φ=0.8 cases and comparing the equivalence ratio distribution for the different speeds as in Figure 27, it is possible to notice that for lower rpm the mixture homogeneity improves, despite a lower turbulent kinetic energy as reported in Figure 28. This emphasizes the dominant role of the mixing time over the turbulence intensity to achieve a uniform hydrogen-air mixture. At high engine speed (3000 rpm), the injection terminates close to the TDC, thus H_2 has no time to homogenize. At 1500 rpm, a greater time available for the mixing, leads to an extremely homogeneous mixture. Figure 29 quantifies, by means of PDFs, the equivalence ratio distribution for all the engine speeds at φ=0.8, confirming the presence of a more homogeneous mixture for lower engine speed.

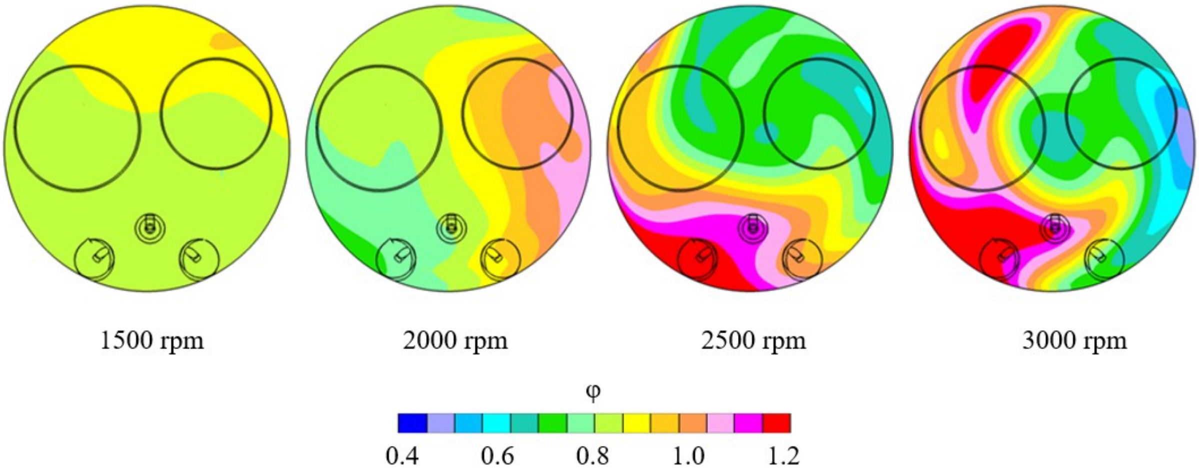

Figure 27: equivalence ratio at 700° CA [19].

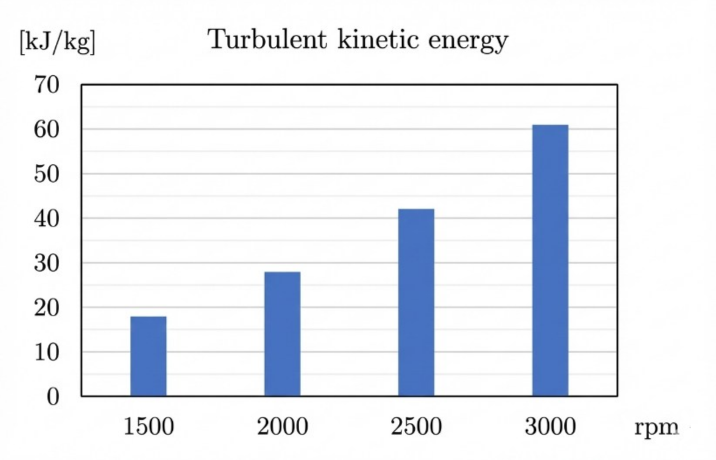

Figure 28: mean specific turbulent kinetic energy for the φ=0.8 cases at 700° CA [19].

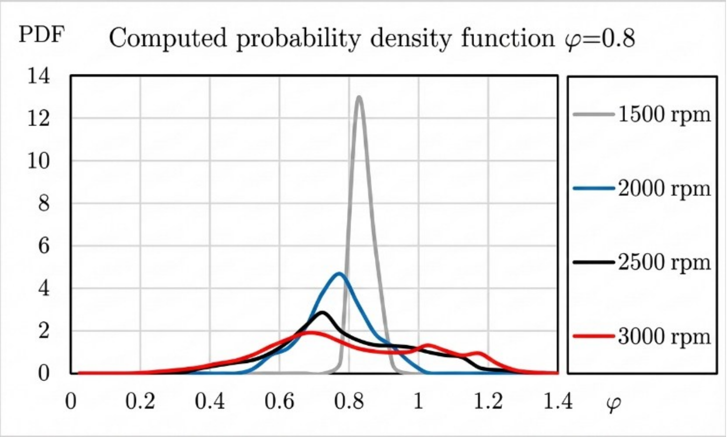

Figure 29: probability density function of φ for all the engine speeds at φ=0.8 [19].

The trend of the PDF with respect to the engine speed for φ=0.6 is the same. As for φ=0.4, instead, the fuel distribution homogeneity seems to be poorly influenced the rpm value, as visible in Figure 30. Such behaviour is due to the effect previously described and shown in Figure 26, which is related to the short injection duration that characterizes φ=0.4 cases. Because of the limited circumferential distribution of the fuel in the cylinder, the increasing available time for the mixing as the engine speed lowers cannot be adequately exploited.

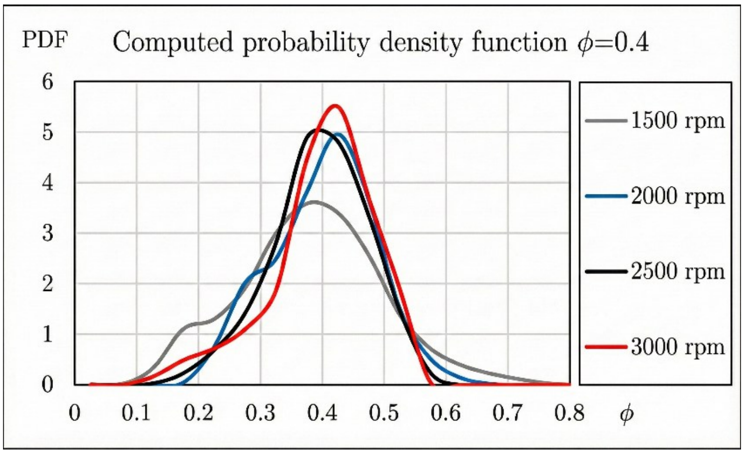

Figure 30: probability density function of φ for all the engine speeds in φ=0.4 case [19].

Finally, an overview of the mixture homogeneity in all the cases is proposed by means of the standard deviation of hydrogen mass fraction, reported in Figure 31.

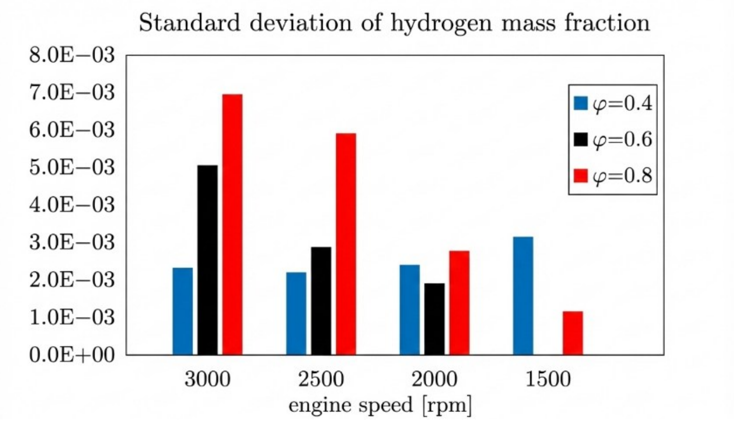

Figure 31: standard deviation of hydrogen mass fraction at 700° CA [19].

Moving to the high-temperature cycle portion, numerical results are presented and compared to the experimental counterpart. As for the latter, data from test bench consist in phase-averaged pressure traces, and they are adopted as a reference for the model validation. An overall agreement is found between simulations and test bench measurements, as visible in Figure 32. The major misalignment can be noticed for the case at 1500 rpm and φ=0.8, as the pressure is strongly underestimated during the expansion stroke. However, for this specific case, an inconsistency can be found in the experimental data. In fact, the in-cylinder pressure trace leads to an IMEP value that, combined with measured BMEP, results in an outlying FMEP value compared to the other cases. Accuracy of the individual case, however, is not the target of this activity, thus no concern was posed on this issue.

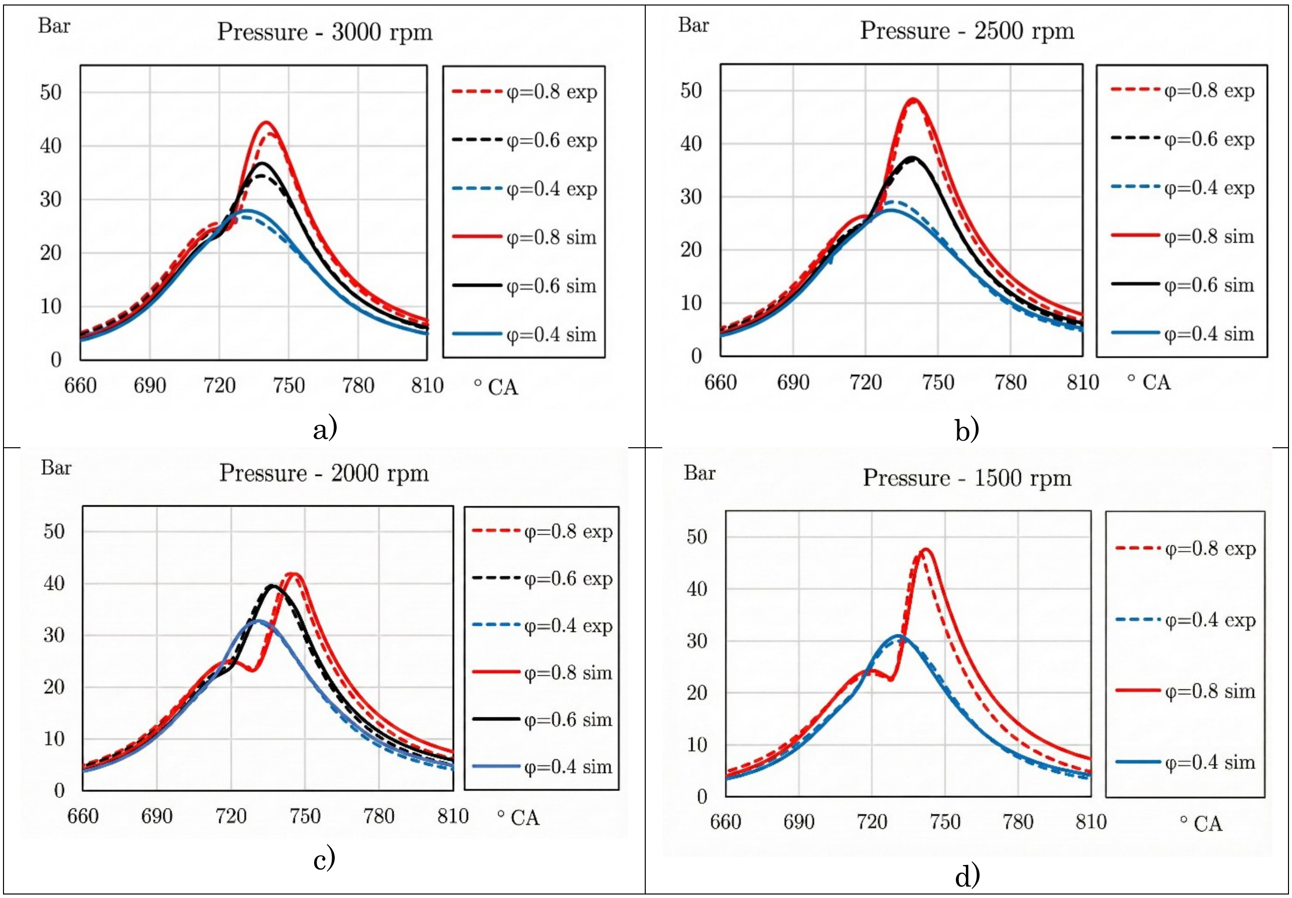

a) b) c) d)

Figure 32: numerical-experimental comparison in terms of average in-cylinder pressure [19].

An error analysis is however carried out to quantify the differences between simulated and experimental pressure traces. Despite accuracy was not the target of this activity, the results are surprisingly aligned with the targets, thus the attempt to gain a deeper insight on the misalignment is done by means of the scatter plots reported in Figure 33. The coefficient of determination R² is there reported as well. The latter is computed as in Equation 29.

$$R^2 = 1 - \frac{\sum_{i=1}^{n}(y_i - \hat{y}_i)^2}{\sum_{i=1}^{n}(y_i - \bar{y})^2} \qquad (29)$$

y_i and $\hat{y}_i$ are the experimental and computed pressure values for the crank angle i, respectively. $\bar{y}$ is the phase-average of the experimental pressure values. The computation is focused on the combustion interval 700°-810° CA.

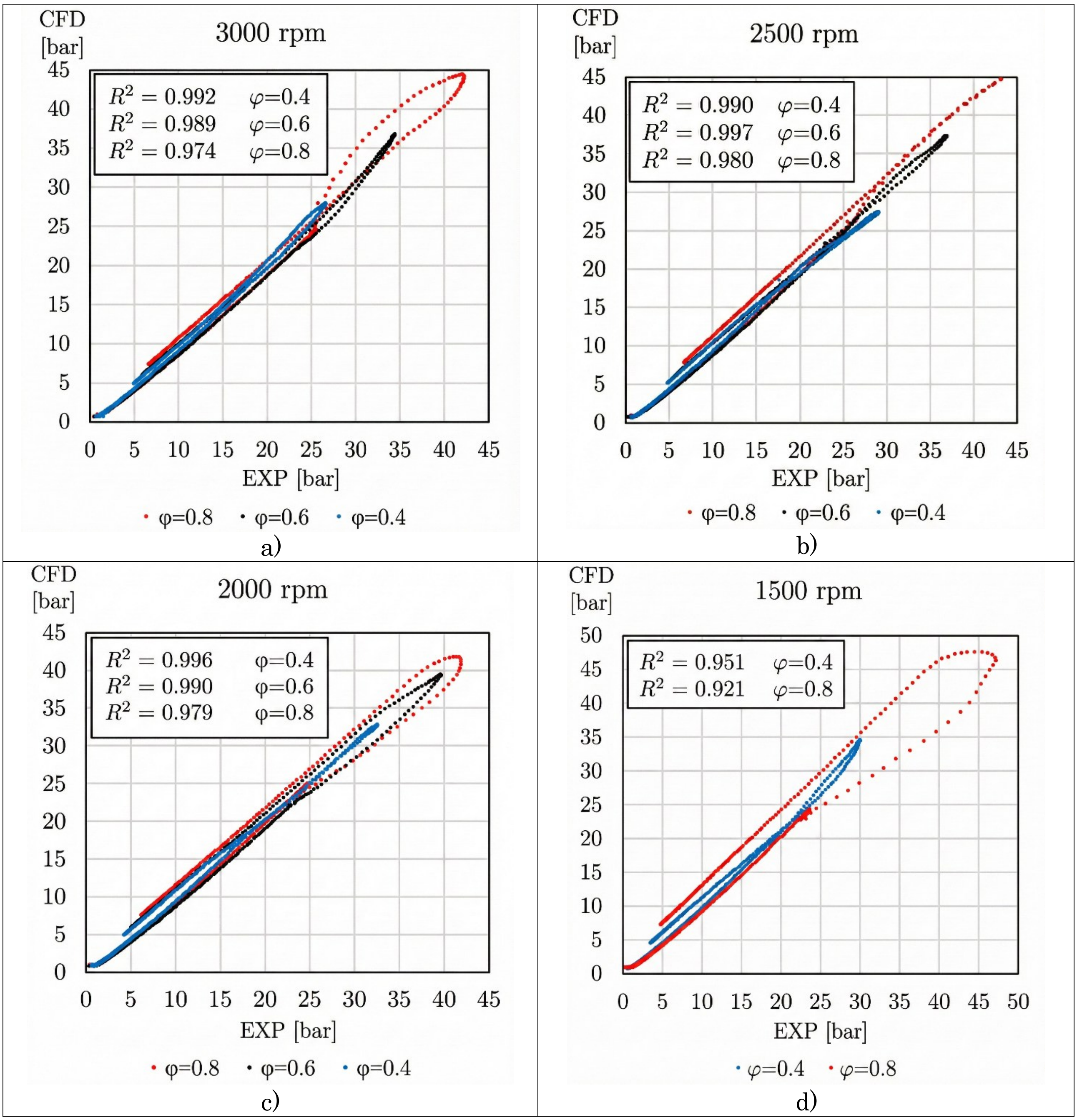

a) b) c) d)

Figure 33: error analysis for all the calculated pressure traces [19].

The apparent heat release rate is analysed and reported in Figure 34. The overall agreement between numerical and experimental outcomes is confirmed, and CFD is able to closely replicate phasing and duration of the investigated cases despite speed/mixture variation. Similarly to the comparison in terms of pressure, it is possible to individuate the misalignment during the expansion stroke for the case at 1500 rpm for φ=0.8. In addition, it is evident that all the cases at 3000 rpm are affected by the same problem, that is combustion phasing anticipation.

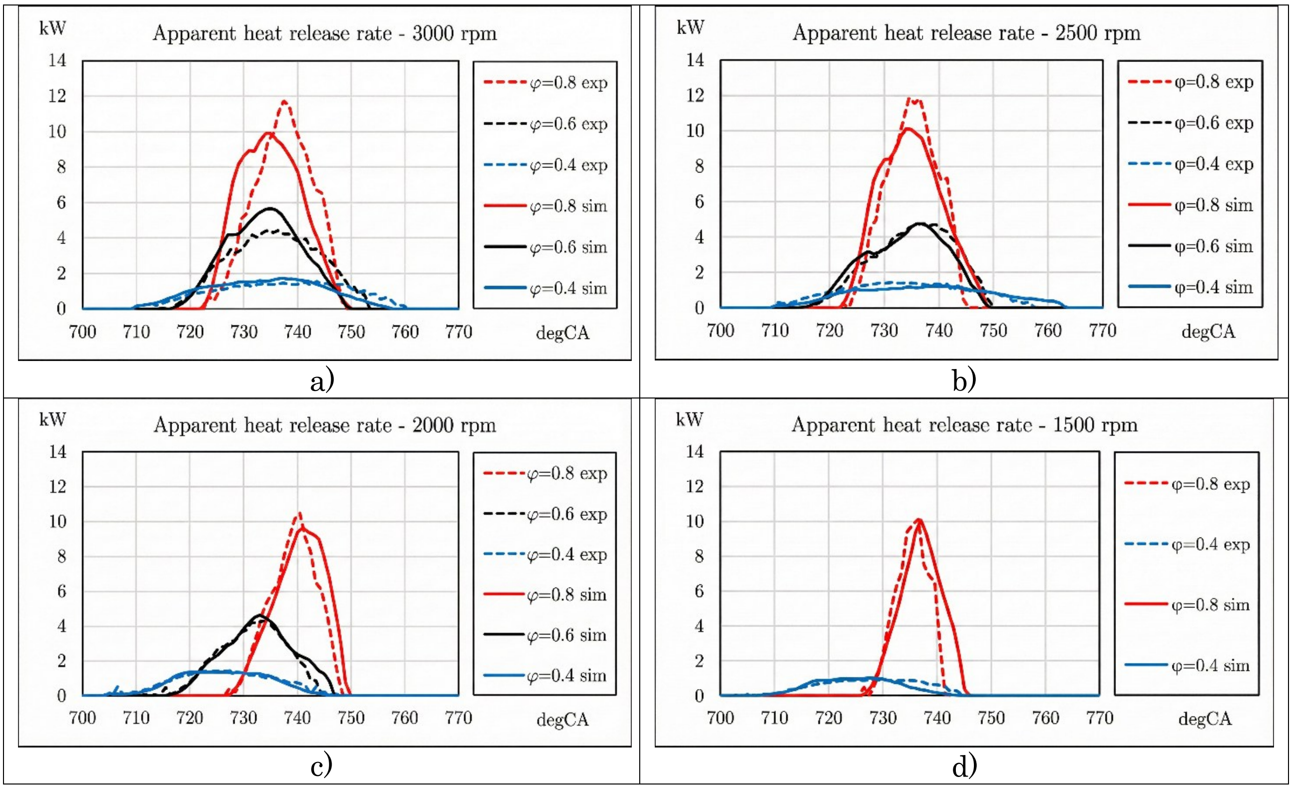

a) b) c) d)

Figure 34: numerical-experimental comparison in terms of apparent heat release rate [19].

In order to highlight the capabilities of the numerical framework, Figure 35 reports the mass fraction of burnt fuel (MFB) for a selection of cases. In particular, a sensitivity to the mixture quality on equal engine speed (as well as the opposite) are proposed in Figure 35 a) and 35 b), respectively. In both the figures, only the extremal operating points are presented, for the sake of clarity. For a consistent comparison of the burn rates, the curves are shifted in the x-axis so that for each one the 50% of burnt mass occurs at 0° CA. This is motivated by the difference in same start of combustion and MFB 50% phasing of the original ones, hindering a clear comparison. In Figure 35 a) the numerical framework shows the correct sensitivity to the mixture quality. In Figure 35 b), instead, attention focuses on the engine speed. Despite a slight underestimation of the burn rate can be noticed at 1500 rpm, the sensitivity to the rpm value is coherent with the experiments, i.e. the combustion velocity nearly halves with the engine speed (as quantitatively confirmed in the following by the 10%-90% values), which means that it is almost constant considering the phenomenon on a time scale. The capability of the model to reproduce this behaviour is not trivial, considering the influences that simultaneously concur: on the one hand turbulence decreases with the rpm value, leading to a lower burn rate; on the other hand, the mixture is much more homogeneous at low engine speed, as confirmed by the PDF curves, leading to a higher combustion velocity.

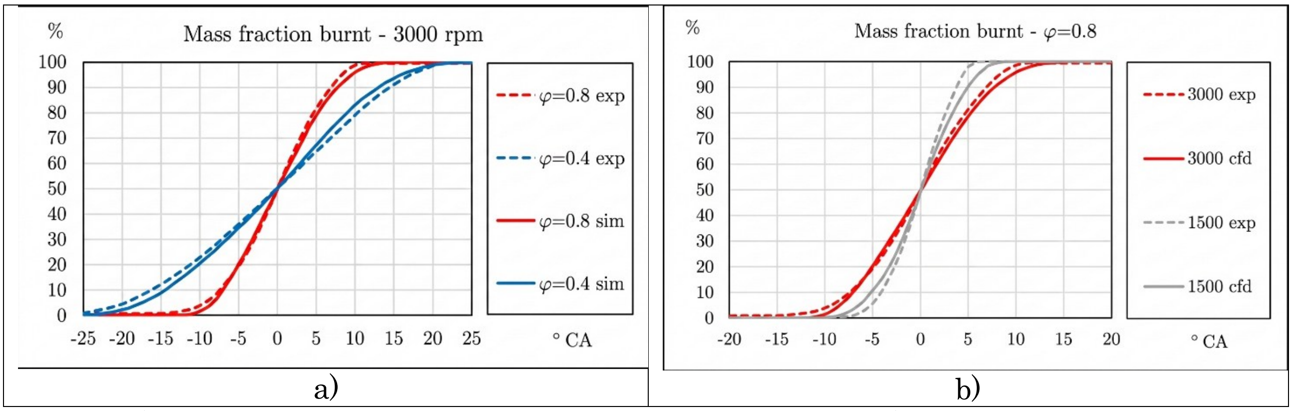

Figure 35: a) mass fraction burnt at 3000 rpm and different mixture qualities; b) mass fraction burnt at φ=0.8 and different engine speeds [19].

In order to further quantify the agreement between CFD and experiments, Figure 36 compares combustion phasing and duration for all the investigated cases. Starting from MFB 50%, operating conditions at 3000 rpm are characterized by a similar value and this is fairly reproduced by CFD. The same is valid at 2500 rpm as well, although CFD underestimates the MFB50 value for the φ=0.4 case. At 2000 rpm and 1500 rpm experiments show a delayed combustion for increasing equivalence ratio and this is properly reproduced in the simulations. Moving to the duration, all the engine speeds are characterized by the same behaviour, that is 10%-90% duration reduces as the mean equivalence ratio increases, which is again well reproduced by the CFD simulations.

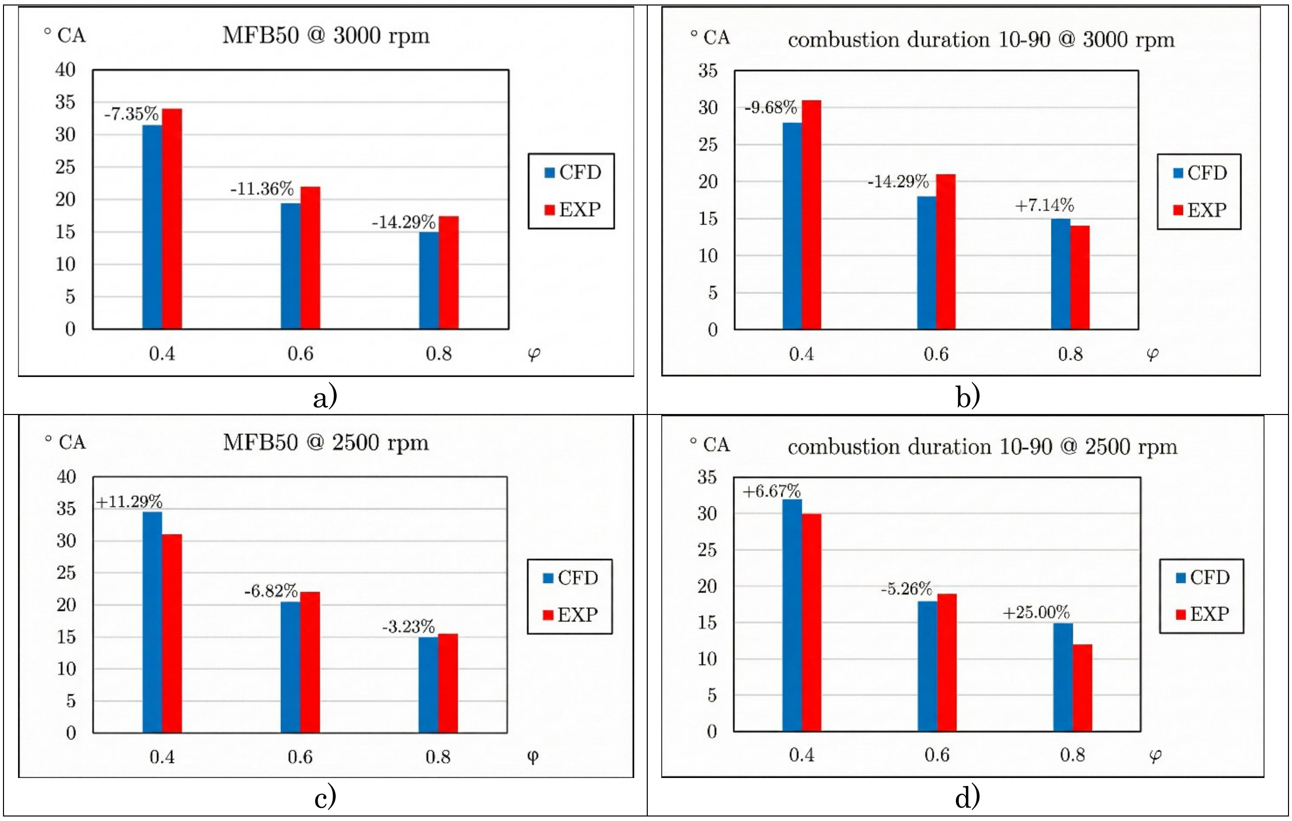

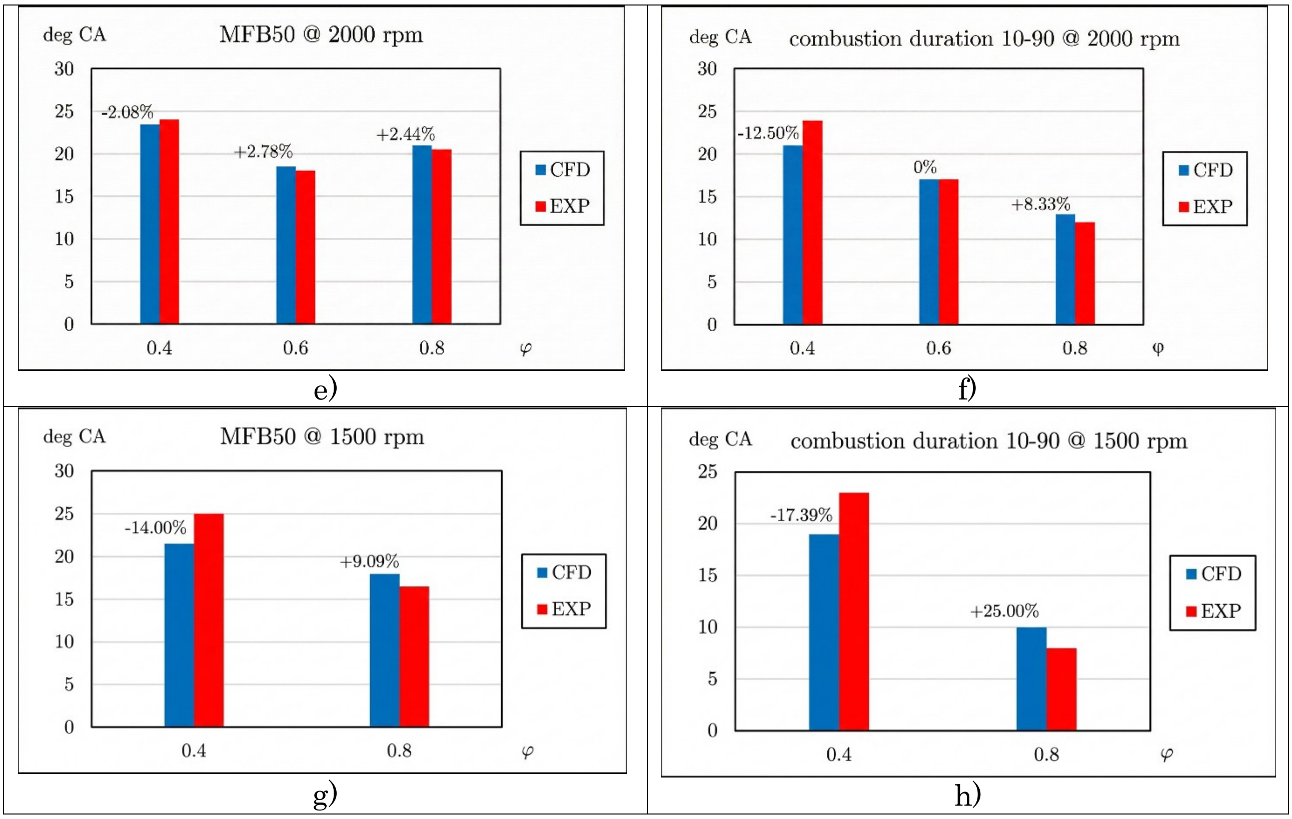

Figure 36: Comparison in terms of combustion timing and duration for all the cases. a, c, e and g show the MFB50 at 3000 rpm, 2500 rpm, 2000 rpm and 1500 rpm, respectively; b, d, f and h report the combustion duration at 3000 rpm, 2500 rpm, 2000 rpm and 1500 rpm [19].

Some highlights follows as a conclusion of the first part of this work. Framework reliability was assessed by the fact that across all the operative points tested, the framework behaved always predicting the correct trends. This was achieved finding a value for the calibration constant A of the turbulent flame speed correlation equal to 3.3. The ignition model, initially calibrated in order to grow the kernel in sub grid till a 2mm radius, was not modified. The calibration constant for the turbulent flame speed remain unaltered through all the rest of the work, while the ignition model required a slight tuning of the critical radius switching from this engine to another. All these results were at first somehow confusing, because of the high framework predictivity found despite the total neglection of flame instability modelling, according to many ([74], [75], [76], [77]), determinant to the framework predictivity. Furthermore, this was achieved for different engine speeds, thus different levels of turbulence, and different equivalence ratio. In other words, the possibility that the instability effect is just masked behind a higher turbulent flame speed calibration constant, somehow incorporating the instability effect, is hard to accredit. The same correlation, in fact, behaved well with high equivalence ratio (where instability is not expected to be present) both at high and low engine speed, but the same hold for the low equivalence ratio tested operating points where, at $\varphi=0.4$, instability is expected to be present. All of this sounded like a difficult coincidence to be believed, and led to the suspect that, despite the engine is operated even at very lean equivalence ratios, this does not automatically imply a strong influence of flame instability. However, uncertainties still remain, at this stage, around this conclusion, making it only an hypothesis to be later verified. Biggest of them is the mixture stratification: in absence of any direct experimental evidence of mixture distribution, it is hard to assess whether the distribution predicted by CFD is indicative of the actual one or it is completely different.

2.5. NO_x predictivity: general overview.

Those considerations led to the prosecution of the activity. Initially, the study investigated the mixture stratification of this engine, approaching another set of operative points for which the NO_x emissions were recorded. Since the NO_x are typically tightly related to the mixture homogeneity, correctly capturing the emissions is here intended as a sort of indirect verification of mixture homogeneity representation. Moreover, since the adopted framework cannot predict NOx emissions by himself, an addition to it was done only on this part of the whole work, that is the detailed chemistry resolution in the burnt gases region. Two different kinetic mechanisms were tested, in order to eliminate the uncertainty on results related to the selection of one specific mechanism rather than another. A more detailed explanation of the additional model, the overall numerical framework and the other details of this second stage of the activity follows.

Firstly, Table 4 resumes the operative conditions in which NO_x emissions were tested, and were reproduced in the CFD simulations.

Table 4: operative conditions tested for the NO_x emissions.

Test N°	φ	SOI [° CA bTDCF]	Speed [rpm]	Spark Time [° CA]
1	0.8	225	3000	0
2				3
3				6
4				9
5				12
6	0.6	190	3000	-15
7				-12
8				-9
9				-6
10				-3
11				0
12				3
13	0.8	175	2000	0
14				3
15				6
16				9
17				12

The combustion model is for most the same already presented, thus it still rely on the progress variable ‘c’. In this case, however, once the progress variable falls below 0.99, the Detailed Chemistry (DC) model is activated. This model is specifically designed to integrate detailed chemical kinetics into engine simulations. It solves transport equations for all the species, such as the general one reported in Equation 30, using a comprehensive reaction mechanism.

$$\frac{\partial}{\partial t}(\rho Y_i)+\frac{\partial}{\partial x_i}\left(\rho u_j Y_i - F_{i,j}\right)=S_i \qquad (30)$$

Y_i is the mass fraction of the i-th species, x_i the i-th coordinate, u_j the j-th velocity component, $F_{i,j}$ the diffusion flux component and S_i represents the production/consumption rate of the i-th species. To derive an expression for S_i, it is necessary to introduce a detailed multi-step chemical reaction mechanism as in Equation 31, including N chemical species and N_R reactions.

$$\sum_{k=1}^{N}(\nu'_{Rk}R_k)=\sum_{k=1}^{N}(\nu''_{Rk}R_k)\,,\quad R=1,2,\ldots,N_R \qquad (31)$$

ν'_{Rk} and ν''_{Rk} represent the stoichiometric coefficients for reactants and products, respectively, of species k and reaction R. R_k is the chemical symbol of the k-th species. The production/consumption rate of the i-th species is described through Equation 32.

$$S_i = M_i \sum_{R=1}^{N_R} \left[(\nu''_{Ri} - \nu'_{Ri}) \left(k_{fR} \prod_{k=1}^{N} [R_k]^{\nu'_{Rk}} - k_{rR} \prod_{k=1}^{N} [R_k]^{\nu''_{Rk}} \right) \right] \quad (32)$$

M_i represents the molecular weight of the i-th species, while ν'_{Ri} and ν''_{Ri} have the same meaning as ν'_{Rk} and ν''_{Rk}, respectively. $[R_k]$ denotes the mole concentration, while k_{fR} and k_{rR} stand for forward and backward rate constants of reaction R. The DC approach is utilized to estimate emission formation. For instance, in case of NO_x, transport equations for NO and NO_2 enable the monitor of production and consumption of these scalars.

Regarding the chemical schemes utilized in the 3D in-cylinder simulations with DC, the widely validated mechanisms proposed by Shrestha [78] and Klippenstein [79] are tested, and their results are compared. This is purposely done to investigate the sensitivity of the results to the chemical scheme.

2.6. NO_x predictivity: results.

The first part of the result section is dedicated to the validation of the proposed numerical framework. In particular, since the NO_x formation is closely related to the combustion process, it is necessary to assess the capabilities of the CFD model to properly predict such phenomenon at first. For that purpose, numerical and experimental pressure traces are compared during the high temperature portion of the engine cycle and they are reported in Figure 37. For each of the tested operating conditions, the results of three different spark times are shown.

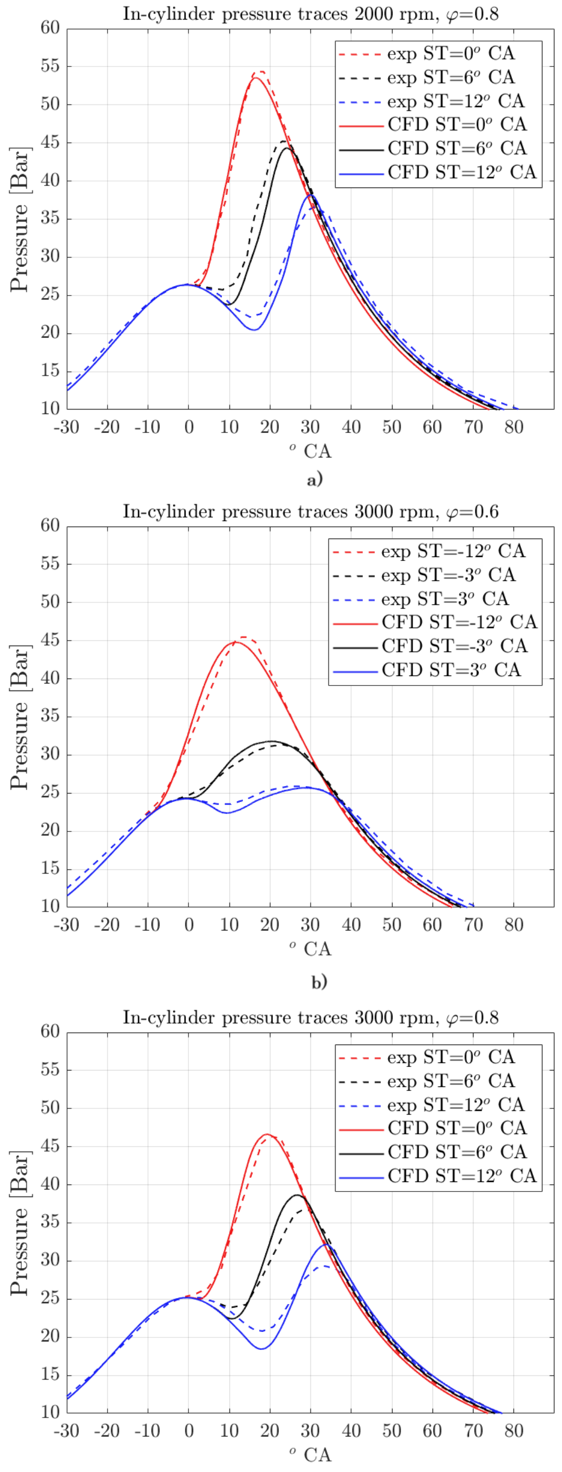

a)

b)

c)

Figure 37: comparison between measured and computed in cylinder pressure traces for: a) 2000 rpm - φ=0.8 case b) 3000 rpm - φ=0.6 case c) 3000 rpm - φ=0.8 case [21].

A satisfactory agreement between CFD outcomes and experimental evidence is obtained, which is noteworthy considering that no case-by-case calibration of the model constants is carried out. The 3D model confirms its capability to properly reproduce the trend of the in-cylinder pressure even as a function of the spark time.

Moving to the focus of the analysis, NO_x formation prediction is evaluated in Figures 38 a) to 38 c), where numerical and experimental outcomes are compared for each investigated condition and spark time. Moreover, on the numerical side, two different sets of results are presented, one per tested chemical scheme. It is important to point out that the numerical NO_x quantities reported in Figure 38 a) to 38 c) correspond to the sums of NO and NO_2 and they are the mg present at the exhaust valve opening. Thus, it is supposed that reactions are frozen in the exhaust pipe, following the validated practice proposed in [32].

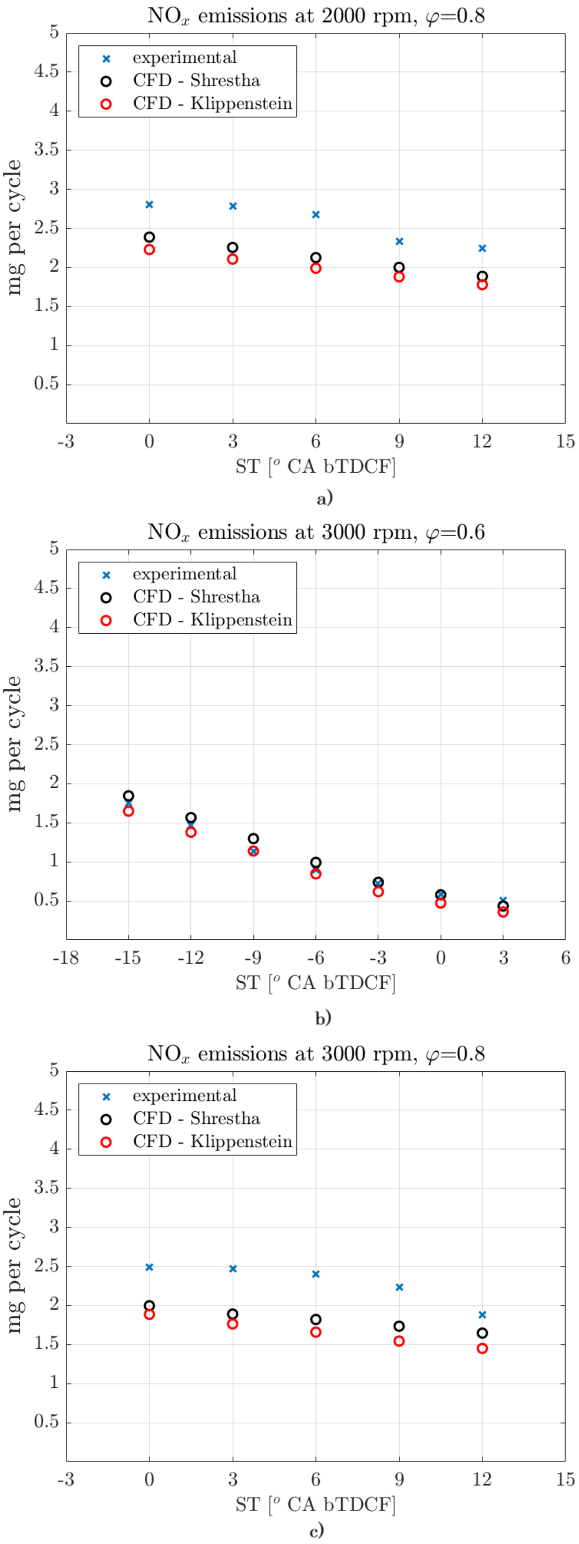

Figure 38: numerical and experimental NO_x emissions as a function of the spark time for: a) 2000 rpm - φ=0.8 case b) 3000 rpm - φ=0.6 case c) 3000 rpm - φ=0.8 case [21].

The simulations are able to match qualitatively and quantitatively the experimental data. Firstly, for all the engine speeds and the equivalence ratios, numerical results are able to properly reproduce the trend as a function of the spark time. In addition, focusing on φ=0.8 cases, the decrease of NO_x increasing the engine speed is properly captured by the simulations. Similarly, on equal engine speed (3000 rpm), CFD is able to correctly predict an increase of NO_x with the equivalence ratio. Moreover, in quantitative terms, all the numerical data are very close to the experimental counterparts, which means all the involved phenomena, gas injection, mixing, combustion and chemical reactions are reasonably captured by the proposed CFD framework. As for the chemistry, it is interesting to point out that, despite the mechanism by Shrestha always provides slightly higher emission levels compared to the one by Klippenstein, the two mechanisms provide similar results. This is a proof that NO_x emissions can be properly estimated independently of the mechanism, provided that the latter is well validated, and show no strict dependence of results on the choice of mechanism.

Results are discussed more in detail hereafter, to highlight the effect on NO_x emissions of two engine parameters, that are spark and injection timings. They affect in-cylinder temperature and mixture stratification, respectively, which are widely recognized to dominate nitrogen oxides formation. It is useful to point out such influences not only to understand the formation of the emissions, but also to emphasize the potential of CFD. In fact, the proven capabilities of the numerical framework to predict NO_x make the use of CFD suitable for the optimization of the engine parameters to lower the emissions.

Decreasing the spark advance leads to a reduction of the maximum pressure inside the cylinder. The reason is that the heat release rate occurs later and later in the cycle, and it is less and less able to compensate the decrease of pressure as a consequence of the cylinder volume increase. Similarly to the pressure behaviour, the maximum temperature of the exhaust gases decreases as well. In this regard, Figures 39 a) and 39 b) show in-cylinder pressures and temperatures for the φ=0.8 3000 rpm case. It is useful to point out that, for brevity, only φ=0.8 and 3000 rpm are considered for the present analysis, but the same trends and considerations are valid for the other operating conditions.

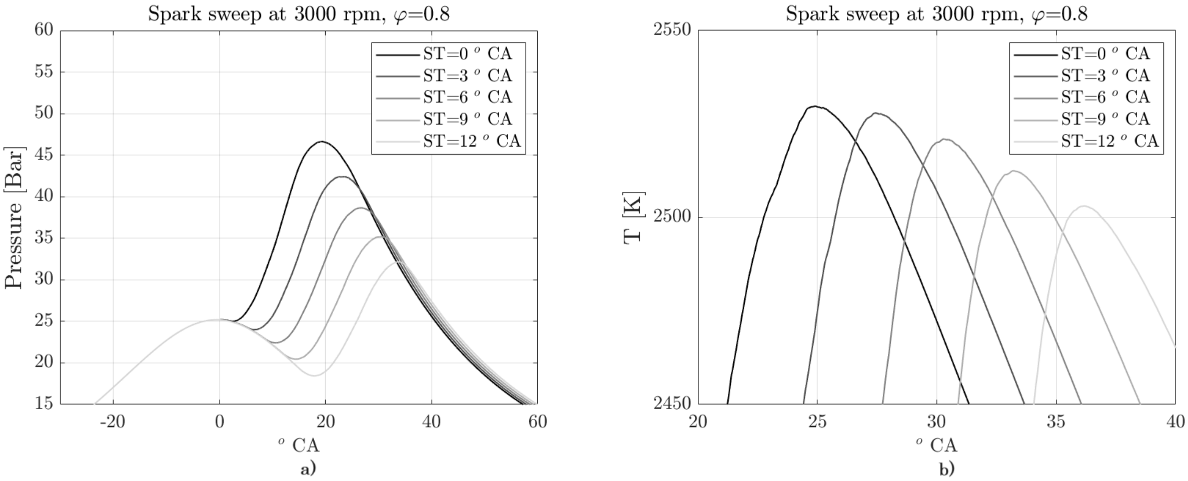

Figure 39: computed in-cylinder pressure a) and temperature b) for the spark times at 3000 rpm and φ=0.8 [21].

NO_x emissions are not simply related to the mean mixture quality, but they are strongly dependent on the local mixture stratification. This is confirmed by the proposed simulations, whose purpose is to assess framework capabilities in predicting emissions when integrating the DC, but also to indirectly confirm the correct prediction of the mixture stratification in this engine. For example, focusing on the 3000 rpm cases, Figures 40 a) to 40 f) show temperature, equivalence ratio and NO mass fraction for two different cases, one at φ=0.6 and one at φ=0.8

(further details one the proposed images can be found in the caption). Only NO is considered in the following, as the concentration is at least one order of magnitude higher compared to NO_2. Looking at the φ=0.6 case, temperature seems to be the main promoter of NO formation as the highest concentration is located where T is the highest. Although T is unquestionably a leading factor for nitrogen oxides formation, the main responsible of the local peak is the local φ, which is close to 0.8. As a demonstration, it is possible to observe in Figures 40 d) to 40 f) the results of the φ=0.8 case, where the peak of NO does not correspond to the one of T but, rather, to the presence of local mixture at φ≈0.8.

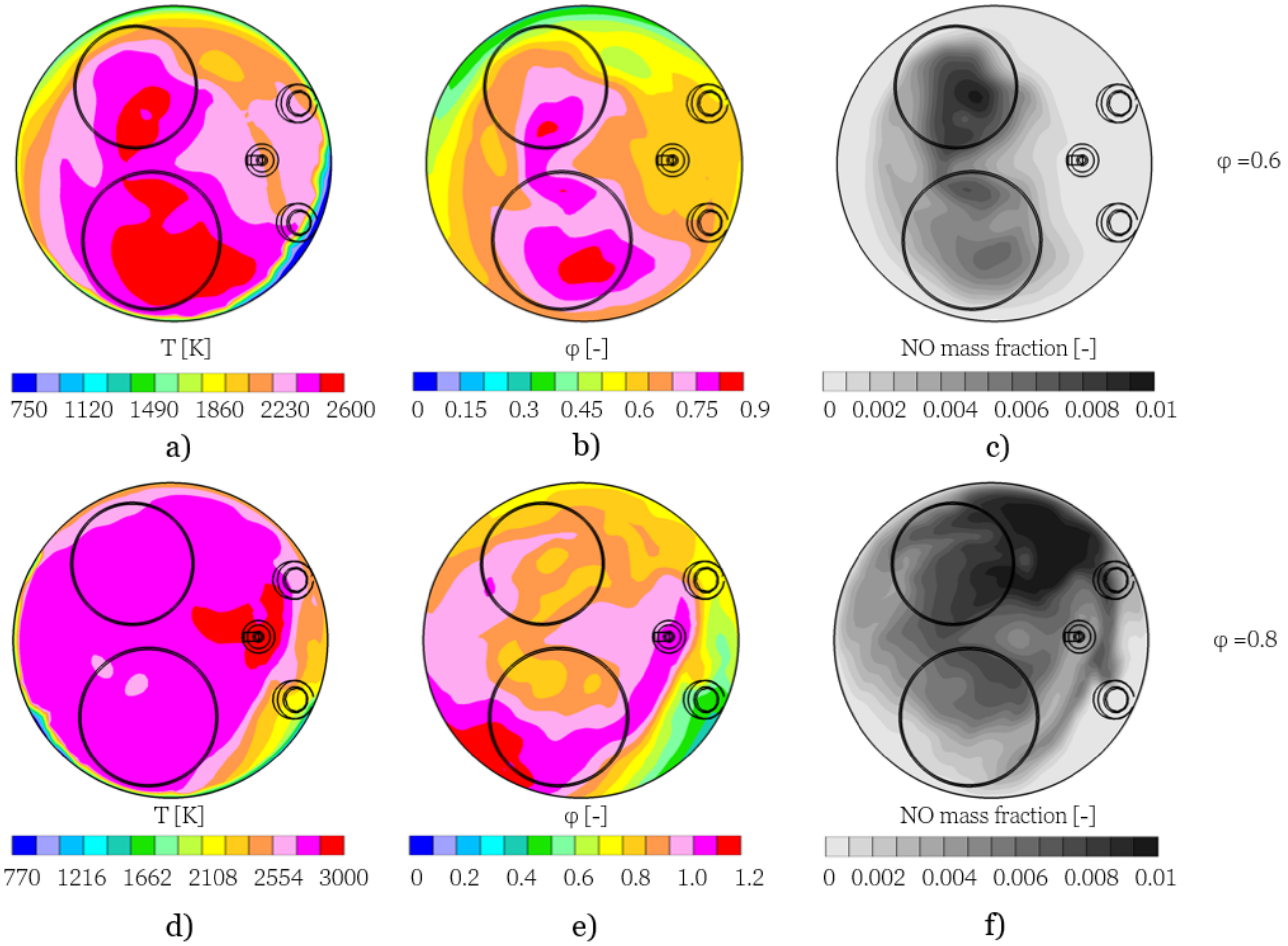

Figure 40: a), b) and c) show temperature, equivalence ratio and NO mass fraction at 750°CA for the case 3000 rpm, φ=0.8 and ST=-15°CA; d), e) and f) report the same quantities at 740°CA for the case 3000 rpm, φ=0.6 and ST=0°CA on a section distant 5mm from head plane [21].

To understand the importance of an equivalence ratio equal (or close) to 0.8, 1D chemical kinetics computations are carried out using DARS licensed by SIEMENS DISW. A single mechanism is considered for brevity in this analysis, i.e. the one by Shrestha. Pressure and unburnt temperature profiles adopted for the computations are representative of the in-cylinder conditions for the analysed operations and they are provided by 3D-CFD. Figure 41 shows the NO mass fraction at fixed pressure and unburnt temperature (40 bar and 900K). Other conditions are omitted as the qualitative behaviour with respect to φ is marginally affected by p or T. Again, similarly to the 3D analyses, the attention is focused on NO as the other nitrogen oxides are characterized by remarkably lower concentrations. Interestingly, Figure 41 shows that NO production increases with the equivalence ratio up to φ≈0.8. Then it rapidly decreases so that, at stoichiometry, the NO mass fraction is nearly the same as that for φ≈0.45.

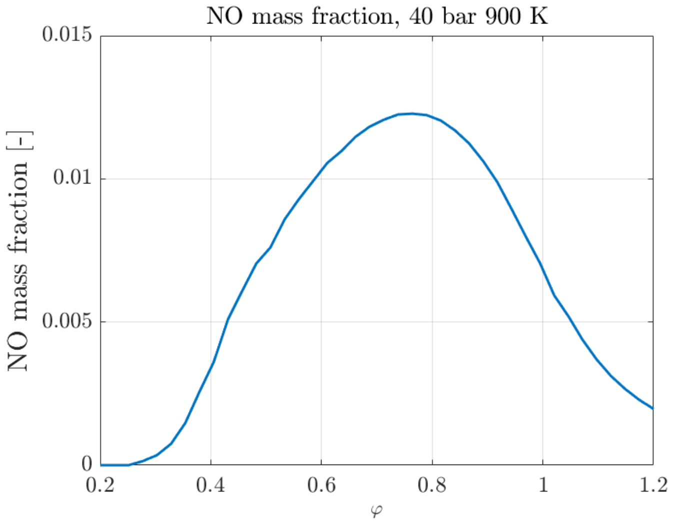

Figure 41: NO mass fraction as a function of the equivalence ratio [21].

In the light of this result, on the one hand it is possible to relate the peak of NO to local φ close to 0.8, in agreement with the outcomes of the 3D simulations. On the other hand, still considering the in-cylinder analyses, it is possible to conclude that, for the φ=0.8 case, increasing the mixture homogeneity is counterproductive. In fact, the peak of NO is positioned where the local φ is close to the average value. Pockets that are richer and leaner compared to the average value are characterized by lower NO mass fraction, as observed in Figure 41.

A further confirmation of the mixture stratification importance comes from the adiabatic flame temperature reported in Figure 42 as function of φ. The plot still refers to 40 bar and 900 K and only one condition is considered, for the same reasons previously commented. The peak of adiabatic flame T is reached at equivalence ratio of nearly 1.1, thus for slightly rich mixtures. Considering the importance of T for NO_x formation, Figure 42 would suggest a peak of NO at φ close to 1.1. Instead, Figure 41 shows a peak at φ≈0.8. The reason is that, moving from φ≈0.8 to φ≈1.1, the oxidation process of hydrogen speeds up more than the one of nitrogen, thus NO production reduces even in presence of higher temperatures. This highlights the role of φ which is not of secondary importance compared to T.

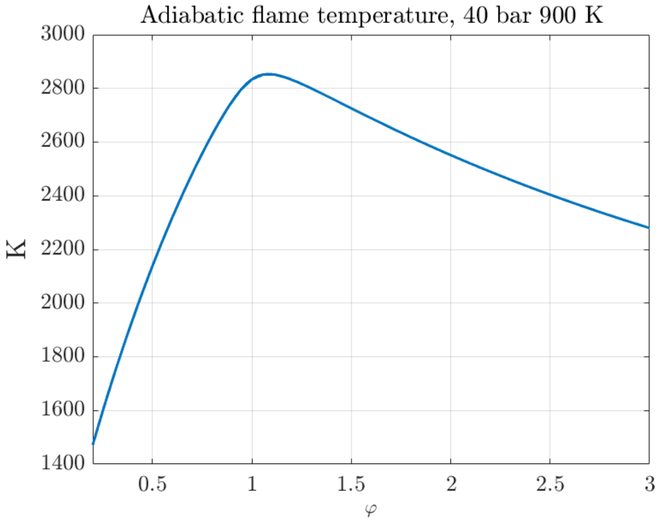

Figure 42: adiabatic flame temperature at 40 bar and 900 K [21].

As a concluding remark of this chapter, reliability of framework was assessed also in terms of mixture distribution, through the indirect verification of the NO_x emissions. This also served as a short test of the framework capabilities in predicting emissions, provided that DC is included as a sub model in the burnt region. The fact that model well behaved under there circumstances, is thus encouraging in corroborating the quest previously born on the actual flame instability influence. The next chapter addresses, to this aim, the application of this framework (in its basic version, without the detailed chemistry in the burned region) on another engine: a 4 valves PFI optical unit. This engine configuration allowed to narrow the focus around the combustion representation, eliminating definitively the stratification uncertainty and even allowing for some flame visualizations.

Chapter 3. Combustion analysis and optical engine comparisons.

This part of the work is addressed at a deeper understanding of the aspects related to the combustion representation, rather than the overall framework reliability. Nonetheless, an extensive validation across 15 operative points is primarily carried out. Peculiarity of those operating points are the low equivalence ratios, ranging from 0.30 to 0.55. While the engine speed remains nearly constant between 1200 and 1500 rpm, all tested equivalence ratios are lean to ultra-lean; this approach aims to stress the framework which, in this first stage, does not include flame instability modelling. This setup allows for the observation of the system's behaviour without mixture uncertainties, thus shifting the focus of the performance prediction primarily onto the combustion model.

3.1. Engine and test description

The engine selected is a four-valve spark-ignition optical engine, whose main geometrical features are reported in Table 5. Figure 43 shows the engine at the test bench, where additional pipes and plenums at both intake and exhaust are present. The engine is characterized by a piston with optical access, visible in Figure 44. In particular, a quartz window is present in the piston bowl, to allow for flame visualization. In this regard, images of the chemiluminescent hydrogen flame are captured using a high-speed camera (Phantom v1610) equipped with a band-pass filter (with a centre wavelength of 318 nm and a full width at half-maximum of 175 nm) and high-speed Intensified Relay Optics (LaVision HS IRO). The images are acquired at a frequency of 1 image/° CA, with a magnification ratio of 0.092 mm/pixel. The camera exposure time and intensifier gain vary based on the equivalence ratio (φ) and range from 80 µs and 65% (at $\varphi = 0.30$) to 30 µs and 50% (at $\varphi = 0.55$). Nonetheless, the piston shape is similar to the original gasoline direct injection engine. For the ignition, an unconventional spark plug is preferred, namely the Bosch ZLR07MTE, which is shown in Figure 45. It is specific for hydrogen operations and equipped with three mass electrodes. Based on the authors' experience with different engine types, such a spark plug represents a valid compromise between cycle-to-cycle variability minimization at low loads and extension of the knock limit at high loads. Finally, the engine is characterized by tumble-promoting intake ports.

Table 5: engine geometrical characteristics.

Bore	77 mm
Stroke	85.8 mm
Displacement	400 cm^3
Compression ratio	10.5:1
Connecting rod	138.5 mm
Pin offset	0.8 mm
N° of valves	4

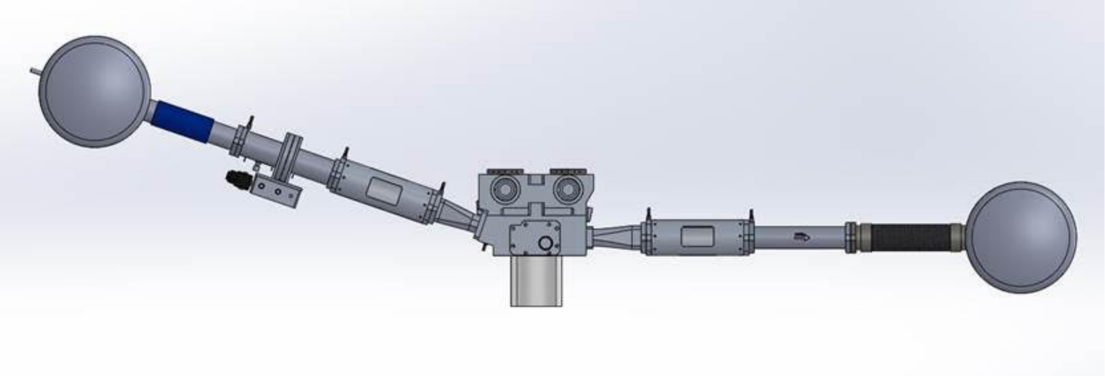

Figure 43: Single-cylinder engine with intake and exhaust plenums and ducts [24].

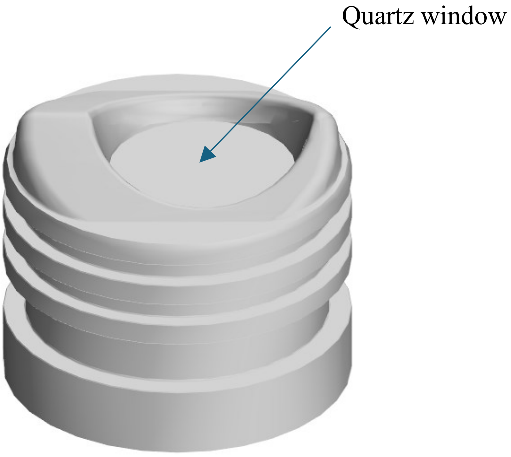

Figure 44: Optical piston.

Figure 45: Spark plug for hydrogen operations.

To ensure a homogeneous mixture, hydrogen is continuously injected through a 6 mm pipe positioned near the intake plenum, as far as possible from the intake valve. The experimental setup is detailed in [80]. Additionally, the duct is sufficiently long to dampen macro turbulent structures that form at the junction between plenum and intake pipe.

The most relevant quantities are monitored at the test bench, as illustrated in the schematic representation of Figure 46. Specifically, instantaneous pressure traces of cylinder and plenums are recorded for each cycle. The traces of 100 consecutive cycles are averaged and then used in the 3D-CFD URANS simulations for comparison or as boundary conditions. The pressure sensor used is an AVL QH32C quartz pressure transducer (piezoelectric sensor) with a nominal sensitivity of 26.82 pC/bar and a pressure range of 200 bar, featuring a maximum linearity error of ±0.25% of the full-scale output. Cycle-averaged temperatures at the intake and exhaust plenums are also measured and used as boundary conditions. The hydrogen-air mixture is regulated by mass flow controllers located upstream of the intake plenum.

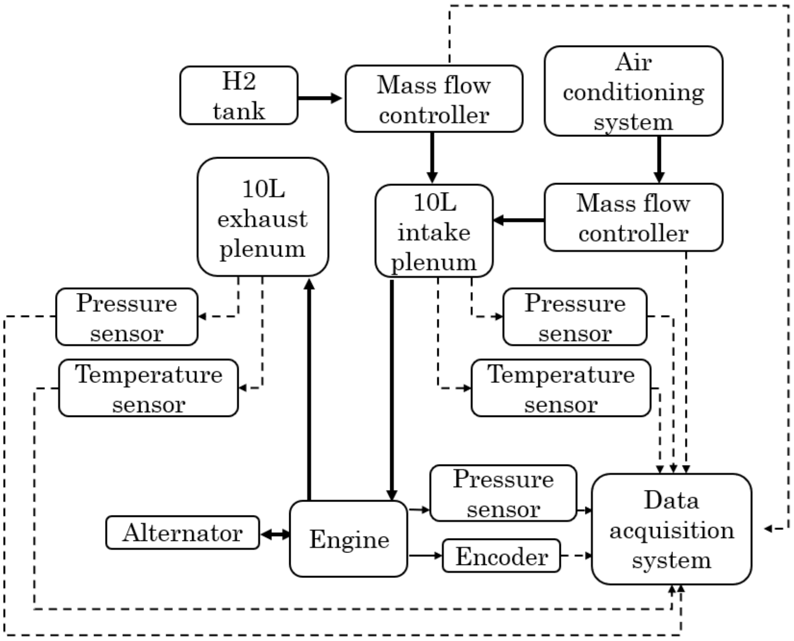

Figure 46: Test bench scheme [24].

Table 6: Experimental operating conditions considered for the numerical simulations.

Case Number #	φ	Ignition [° CA BTDC]	Intake temperature [K]	Exhaust temperature [K]	Average intake pressure [bar]	rpm	CoV IMEP [%]
1	0.30	15	295.7	596.0	0.7	1500	4.875
2	0.35	15	295.7	608.6	0.7	1500	2.144
3	0.40	15	295.8	623.7	0.7	1500	1.37
4	0.45	15	295.9	635.0	0.7	1500	0.966
5	0.50	15	296.0	658.4	0.7	1500	1.174
6	0.55	15	296.0	666.2	0.7	1500	1.508
7	0.30	15	295.2	590.4	0.9	1500	3.662
8	0.35	15	295.3	598.8	0.9	1500	1.81
9	0.40	15	295.5	612.6	0.9	1500	1.455
10	0.45	15	295.7	623.0	0.9	1500	1.098
11	0.35	23	296.2	544.0	0.89	1200	1.424
12	0.40	18	296.5	566.6	0.82	1200	1.066
13	0.45	14	296.7	599.2	0.75	1200	1.375
14	0.50	11	296.9	597.2	0.73	1200	1.197
15	0.55	8	297.0	610.0	0.72	1200	1.127

The tested operating conditions are resumed in Table 6. Cases 1 to 6 are characterized by same spark time, intake pressure and engine speed, while the equivalence ratio varies from 0.30 to 0.55. Cases 7 to 10 have the same spark advance of the previous ones while the intake pressure is fixed to 0.9 bar. The equivalence ratio sweeps from 0.30 to 0.45. Finally, the conditions of the cases 11 to 15 are obtained by pursuing the same IMEP. This is obtained by increasing φ and reducing spark advance and intake pressure. For these final cases, the engine speed lowers from 1500 to 1200 rpm.

As an example of the investigated operating points, case #1 (the one with the highest CoV IMEP) is presented in Figure 47. In particular, the in-cylinder pressure trace of each of the 100 cycles is plotted, along with average and ±2σ band (representing the dispersion of the 95% of the cycles). The ensemble average pressure trace is the one used for the comparison with URANS simulations and the same is valid for the other operating points.

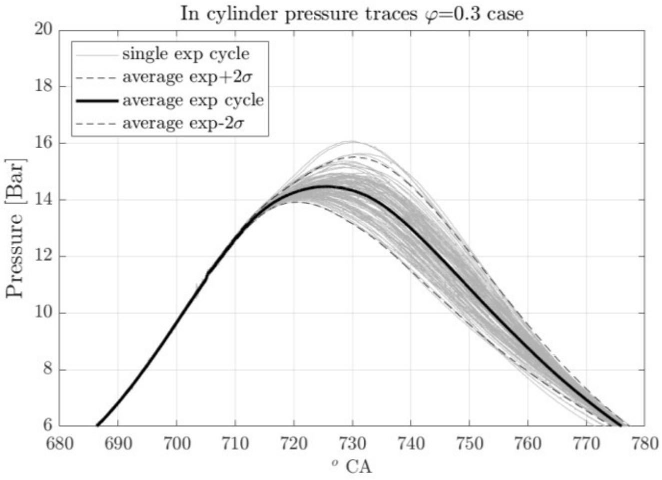

Figure 47: Pressure traces of each of the 100 cycles are shown along with average and ±2σ band, for case #1.

According to the experimental test aiming to ensure maximum homogeneity, a perfectly-homogeneous mixture of the required quality is imposed at the inlet boundary of the model. Time-dependent pressure boundary conditions are applied at intake and exhaust and an example is reported in Figure 48. Such conditions are obtained by experimentally measuring pressure in the intake and exhaust plenums for each cycle, and then averaging over 100 cycles for each operating condition. The temperatures at these boundaries is kept constant and equal to the values provided in Table 6 for each case. The reason for constant temperature values is that the adopted thermocouples are not fast enough to obtain cycle resolved traces.

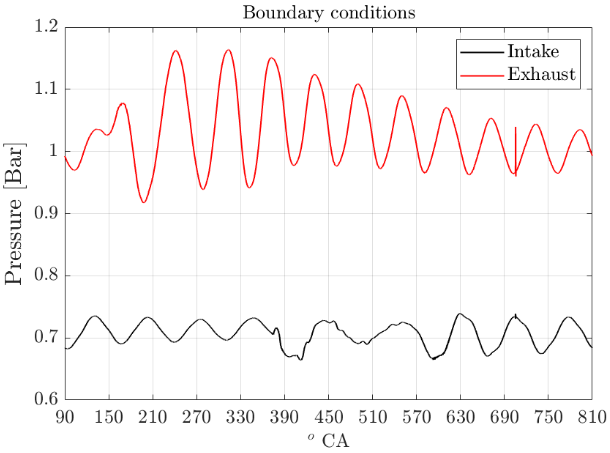

Figure 48: Time-dependent pressure boundary conditions imposed at intake and exhaust for case #6 [20].

To eliminate some more uncertainties, in this activity also a grid sensitivity is carried out. For brevity, only the sensitivity on one of the investigated cases is shown. Based on the authors previous experience [81], an initial mesh is chosen, able to balance accuracy and computational cost and hereafter referred to as "Coarse mesh." Then, a finer mesh ("Fine mesh") is tested in order to analyse the sensitivity of the results to the mesh. The "Fine mesh" has a minimum cell size of 0.4 mm and a maximum of 0.8 mm, whereas the "Coarse mesh" features sizes that are 50% larger, with a minimum of 0.6 mm and a maximum of 1.2 mm. At BDC, the finer mesh consists of nearly 1 M cells, while the coarser one contains about 500 k cells. As shown in Figure 49 where results on the case #6 are presented, the predicted in-cylinder pressures are very close and the difference is almost negligible. This is an indication that mean flow structures and gradients resolved by the URANS equations are well captured by the "Coarse mesh". Therefore, the latter is preferred to the finer version to save computational cost and time.

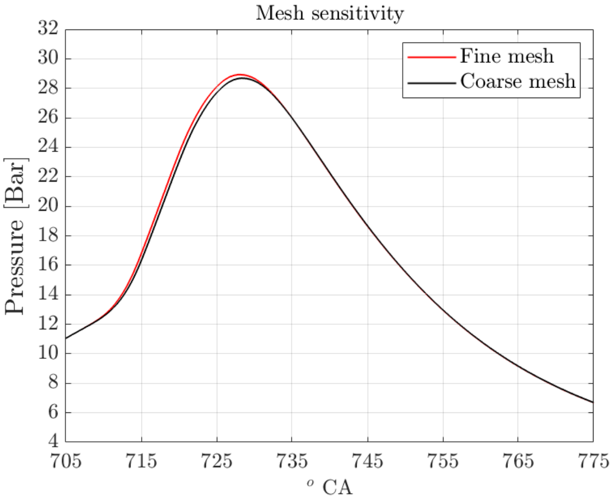

Figure 49: Pressure traces computed with different grids for case #6 .

The computational mesh selected for the present study ("Coarse mesh") is depicted in Figure 50. The cell size varies between the minimum and maximum values specified above, based on the local geometry. Around the spark plug, the cell size is further halved. A single prismatic layer with a height of 0.3 mm is used at the wall.

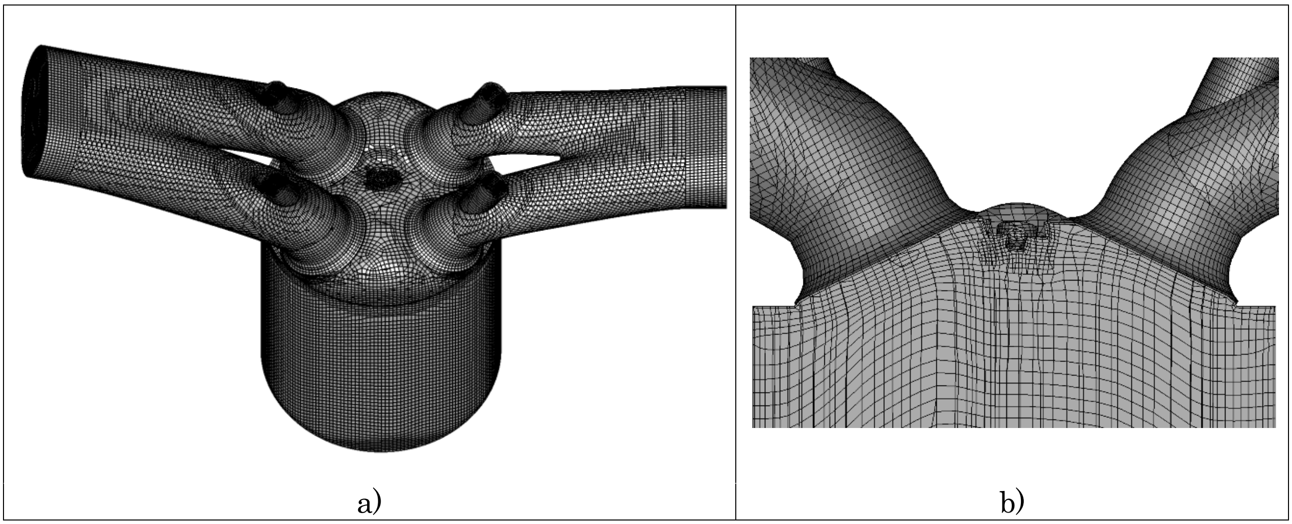
a)
b)

Figure 50: The adopted computational grid at the BDC: global mesh a) and spark refinement detail b) [24].

3.2. 3D CFD simulations results

In the present section, the predictive capabilities of the proposed approach are proven. At first, a numerical-experimental comparison in terms of pressure traces is proposed. The comparison starts with the φ sweep at 0.7 bar of intake pressure, which is reported in Figure 51 a). Then Figures 51 c) and 51 e) show the φ sweeps at 0.9 bar and constant IMEP. Overall, a strong agreement between CFD and experimental outcomes is found. The main discrepancies deal with the pressure peak for some cases. In particular, major underpredictions (but always lower than 1.3 bar) are noticed in the φ = 0.45 case of the 0.7 bar sweep, in the φ = 0.40 case of the 0.9 bar sweep and in the φ = 0.35 case of the constant IMEP sweep. A more detailed comparison between CFD and experiments is obtained by the apparent heat release rate (AHRR) traces reported in Figures 51 b), 51 d) and 51 f). An overall agreement is confirmed, even if discrepancies are identified also for this quantity. In particular, the main differences between numerical and experimental values are observed in correspondence of the AHRR peaks and towards the combustion completion, where the numerical traces are, for most cases, too inflated with respect to the experimental ones. The reason for this overestimation is multiple. Firstly, flame quenching at the walls is not modelled at this stage of numerical framework development. The effect can be non-negligible during the combustion completion, when the flame is close to the chamber walls. Secondly, the blow-by is not considered in the simulations even if slightly present in the experiments. Thirdly, although the boundary conditions derive from the experimental measurements, minimal errors in the numerical trapped mass of the different cases are present. Fourthly, the adopted heat transfer model is widely tested on gasoline and Diesel engines but no validation is available for H_2 ICEs. Although it should be able to account for the mixture properties (thanks to variable Prandtl number inside the thermal wall function), the low quenching distance characterising H_2 combustion may require ad hoc modification of the model. Anyway, despite the overestimations in terms of total heat release in some operating conditions, the overall agreement between simulations and experiments is not remarkably affected.

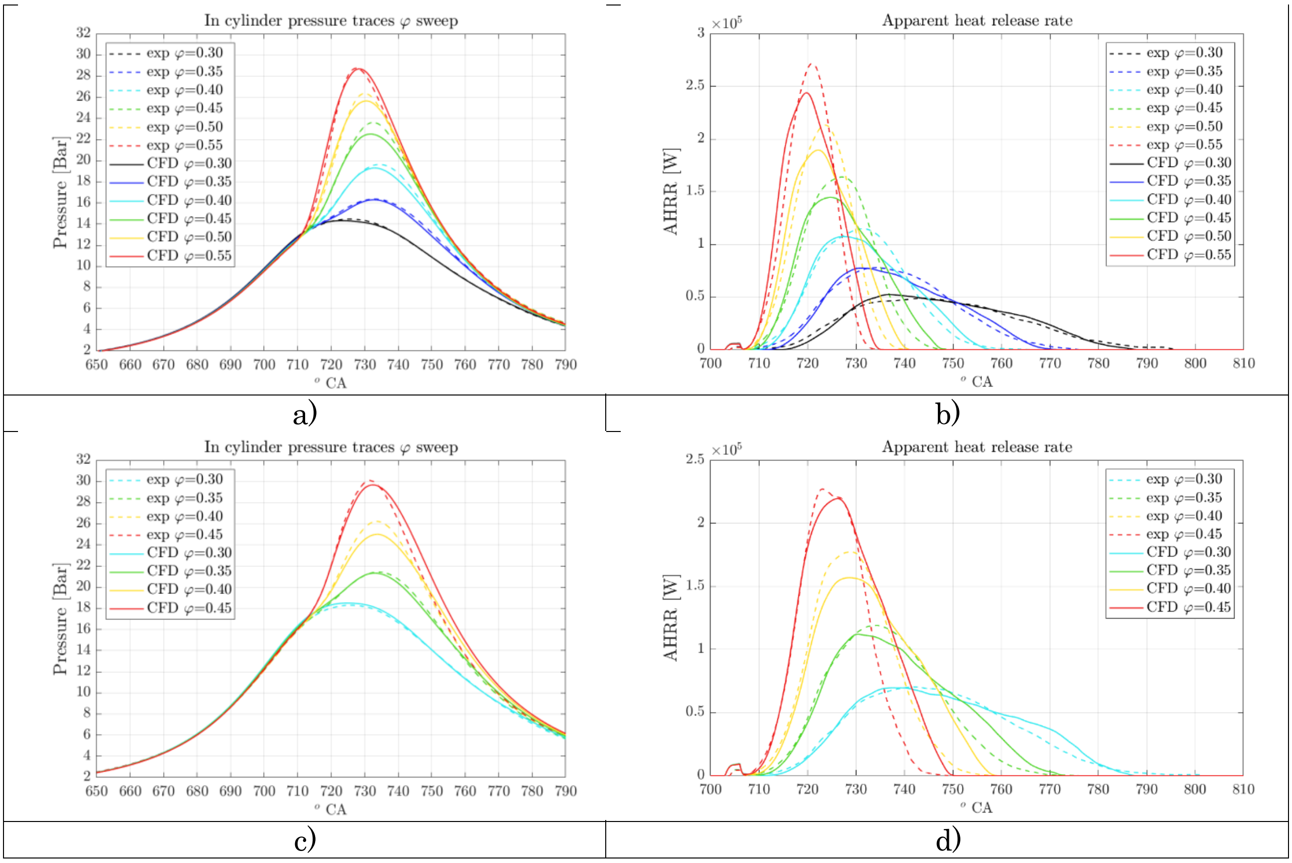

a) b)

c) d)

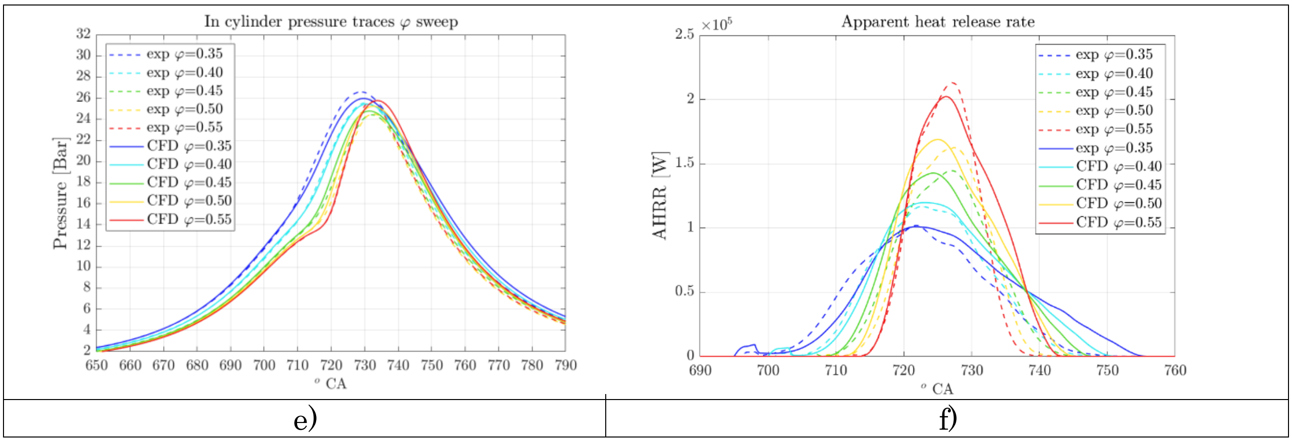

e)

f)

Figure 51: Numerical-experimental comparison in terms of pressure traces and AHRR at intake pressure of 0.7 bar (a and b), intake pressure of 0.9 bar (c and d) and constant IMEP (e and f) [24].

For a more quantitative comparison between CFD and experiments, combustion indicators (MFB, mass of fuel burnt) are reported in Figure 52, where MFB 0-10, MFB 50 (combustion timing) and MFB 10-90 (combustion duration) are proposed. They are CA intervals between spark-time and 10% of MFB, between spark-time and 50% of MFB and between 10% and 90% of MFB, respectively. Combustion timing is properly captured, as demonstrated by the MFB 50 plots. The error between numerical and experimental values is reported and is shown to be minimal. Greater gaps can be noticed for MFB 0-10 and MFB 10-90. As for the latter, the overall tendency throughout the sweeps is to underestimate the combustion duration for the lower equivalence ratios, because of inaccuracies in the combustion completion prediction. This is mainly related to the flame-wall interaction, which is not modelled here. In fact, very lean mixtures are more sensitive to flame quenching at the end of the combustion while approaching the walls. Conversely, by increasing the equivalence ratio, the sensitivity is lower and the CFD outcomes are more accurate compared to the experimental counterparts.

Intake pressure 0.7 bar — Intake pressure 0.9 bar — Constant IMEP

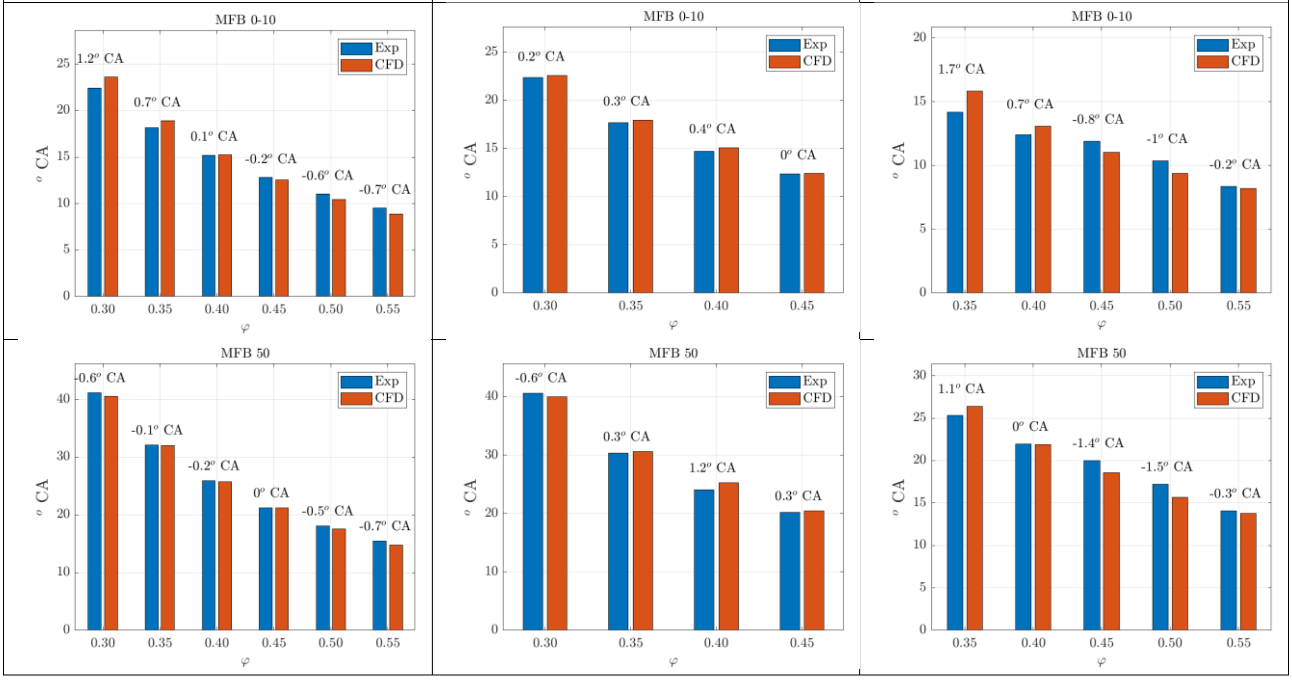

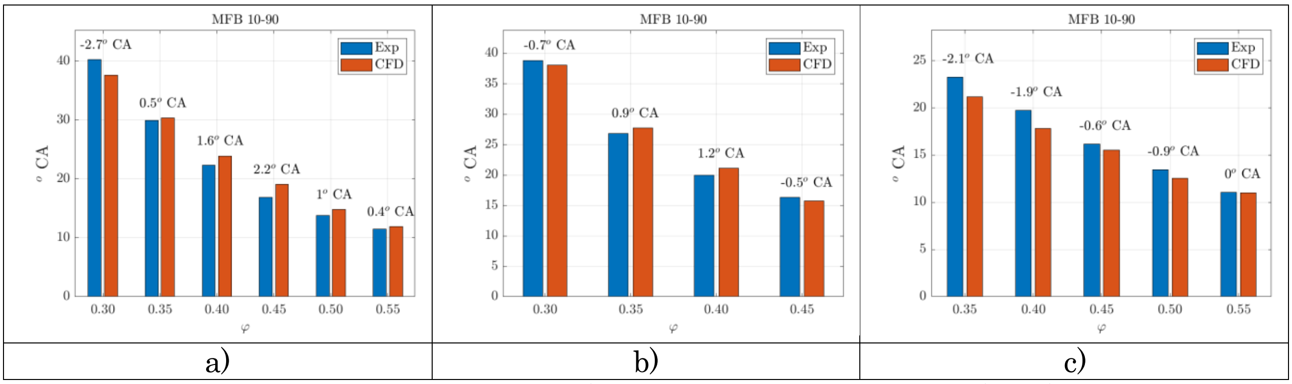

a) b) c)

Figure 52: Comparison of combustion indicators (MFB 0-10, MFB 50 and MFB 10-90) for a) the φ sweep at an intake pressure of 0.7 bar, b) the φ sweep at an intake pressure of 0.9 bar and c) the φ sweep at constant IMEP [24].

As a further validation, a comparison in terms of imaging is also proposed. In Figure 53, the experimental flame images are compared with the calculated G = 0 isosurface, for the φ sweep at an intake pressure of 0.7 bar. Only this sweep is considered for the comparison, as experimental images are not available for the other operating conditions. In each row, three different CAs are compared: 709°, 715° and 721°. 709° is the minimum CA at which the flame kernel is visible in the φ=0.30 case, while 721°CA is the maximum one before the flame expands beyond the optical window in the φ=0.55 case. 715° CA is purposely chosen as in the middle of the previously considered values. Overall, the numerical representations closely resemble the experimental images. A more detailed discussion of the imaging is proposed in the following.

Considering the combustion indicators presented in Figure 52, the MFB 0-10 is roughly 16° CA for the φ=0.40 case and 10° CA for the φ=0.55 one. Therefore, the 10% of MFB occurs at about 721°CA and 715°CA, respectively. Not by chance, observing the images of Figure 53, φ=0.40 case at 721° CA and φ=0.55 one at 715° CA show a similar flame position. In addition, the previously discussed increasing overestimation of the MFB 0-10 obtained by lowering the equivalence ratio is confirmed by the images, that show a predicted flame radius smaller than the experimental counterpart at φ=0.30 and φ=0.35.

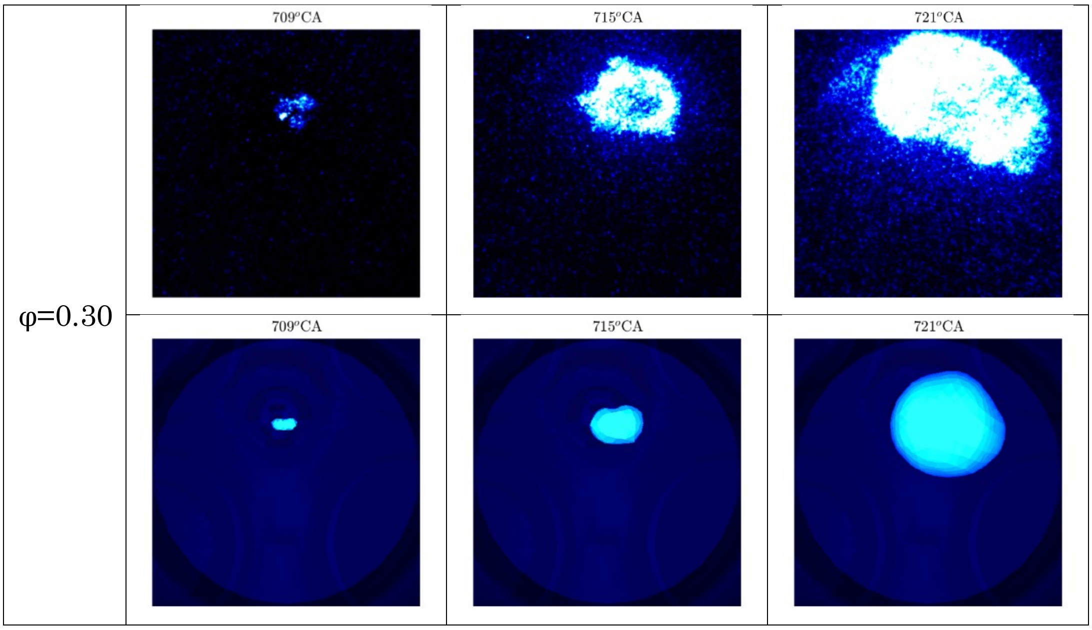

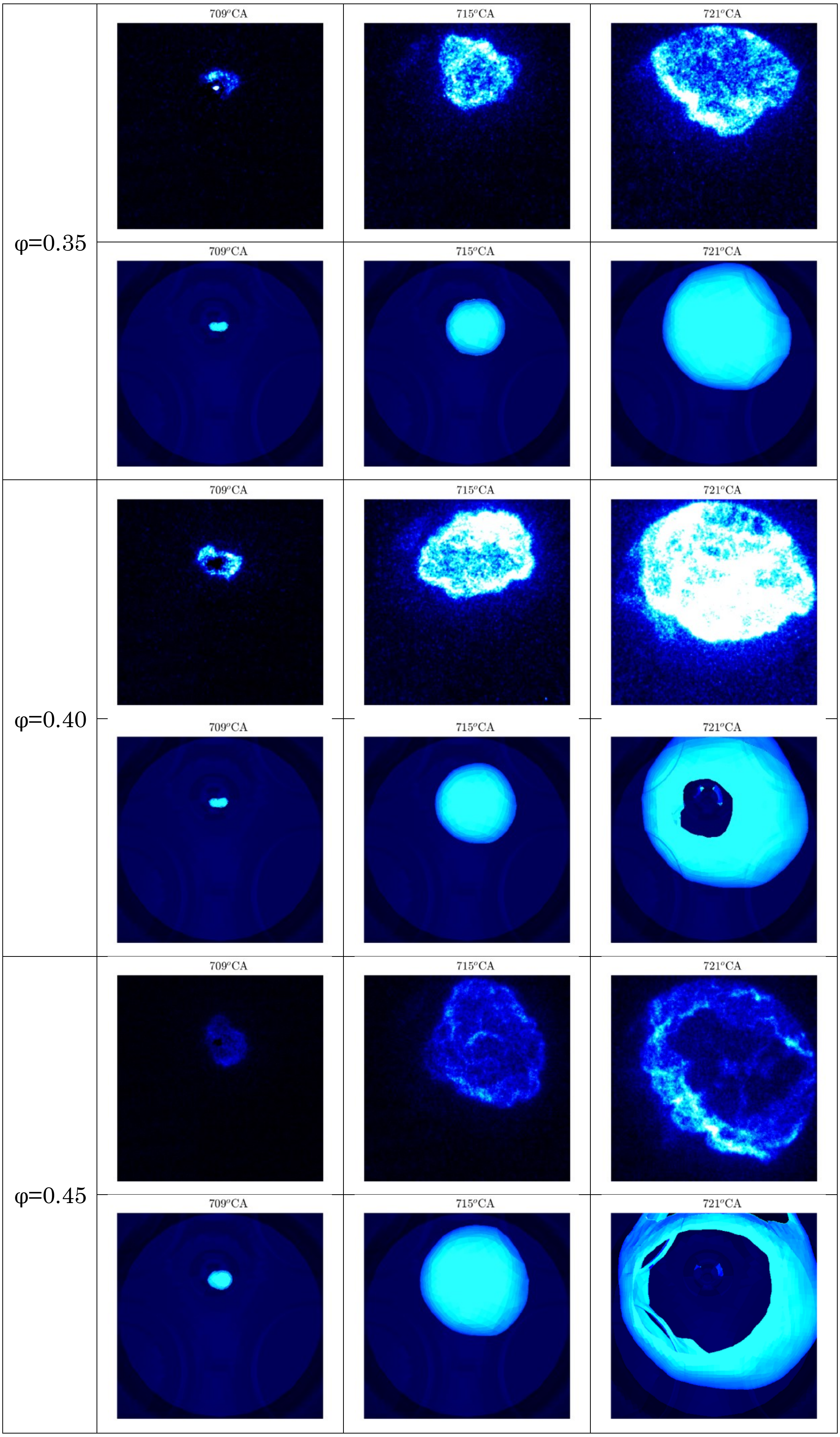
φ=0.35
709°CA
715°CA
721°CA
709°CA
715°CA
721°CA
φ=0.40
709°CA
715°CA
721°CA
709°CA
715°CA
721°CA
φ=0.45
709°CA
715°CA
721°CA
709°CA
715°CA
721°CA

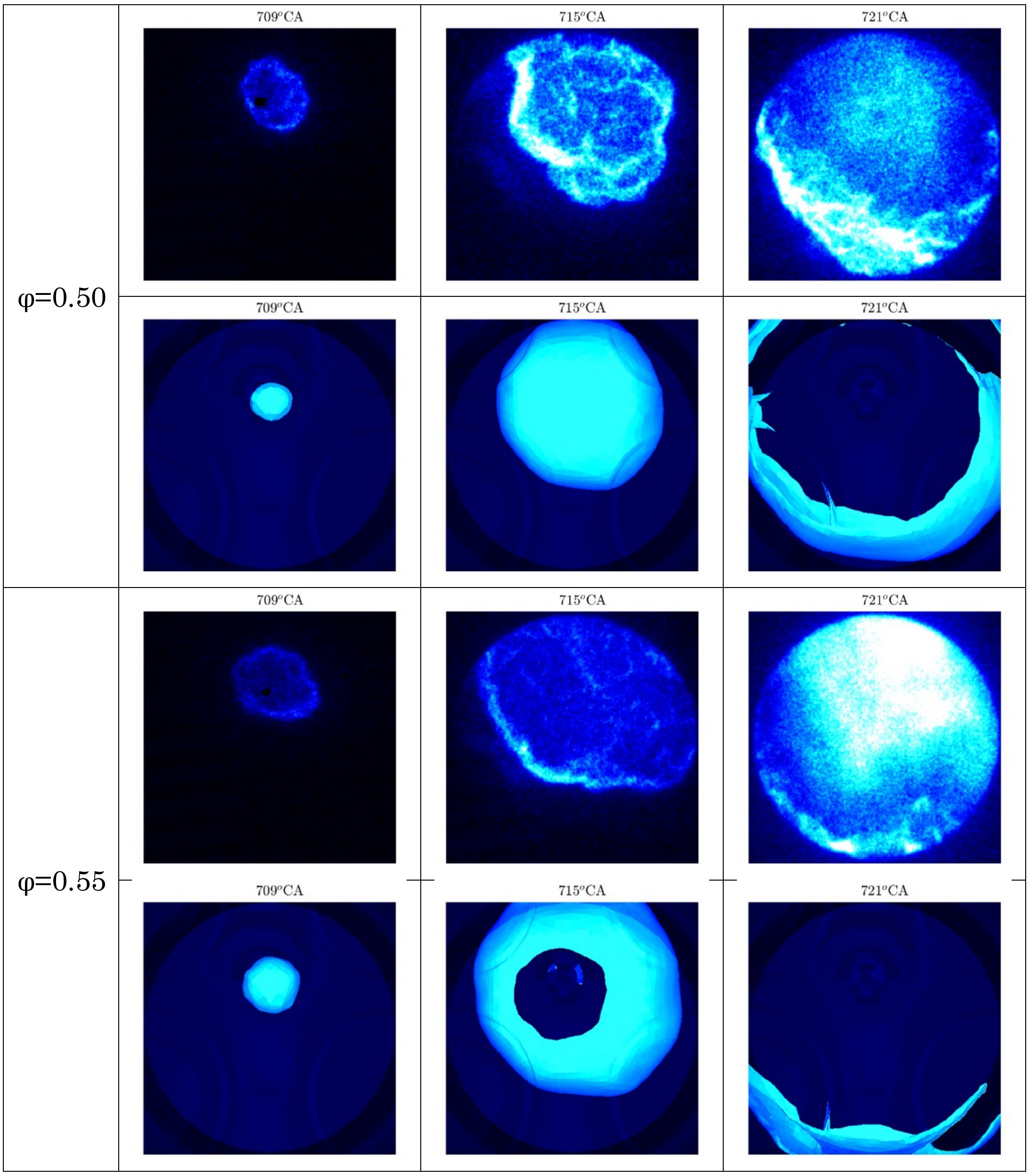

Figure 53: numerical-experimental comparison in terms of flame imaging at 709°CA, 715°CA, and 721°CA for each case of the φ sweep at intake pressure 0.7 bar [24].

In order to perform a quantitative comparison, Figure 54 a) reports a plot of the flame radius as a function of the CA, while Figure 54 b) its time derivative. The radius is computed as the one of the circle characterised by the same perimeter of the flame contour. The equivalent radius is calculated using the same method for both numerical and experimental images. The solid lines are the ensemble average experimental data, with the semi-transparent area representing a ±2σ deviation. The computed data are reported with dotted lines. The lines interrupt roughly in correspondence of the 5% of burnt mass. As the flame radius evolution is almost linear in all the cases, two important factors should be considered: the slope of the lines and their shift. Before analysing such factors, it should be pointed out that, in the CFD framework, the ignition model switches off soon in the combustion process, i.e. at ~707°CA for the φ=0.55 case and ~712°CA for the φ=0.30. This means that the ignition model is mainly responsible for the shift, while the slope (i.e. combustion rate) is primarily related to the combustion model (intended as a combination of model itself and correlations of laminar and turbulent flame speeds). As visible in Figure 54 a) and confirmed by the derivative reported in Figure 54 b), the slope is reasonably captured, as proof of the reliability of the combustion model. All the numerical curves fall in the respective bands representing 95% of the experimental traces. The main issues deal with the shifts of the traces, which are primarily accumulated during the ignition model activity periods. However, errors can be considered acceptable, even if there is room for improvement in the ignition modelling.

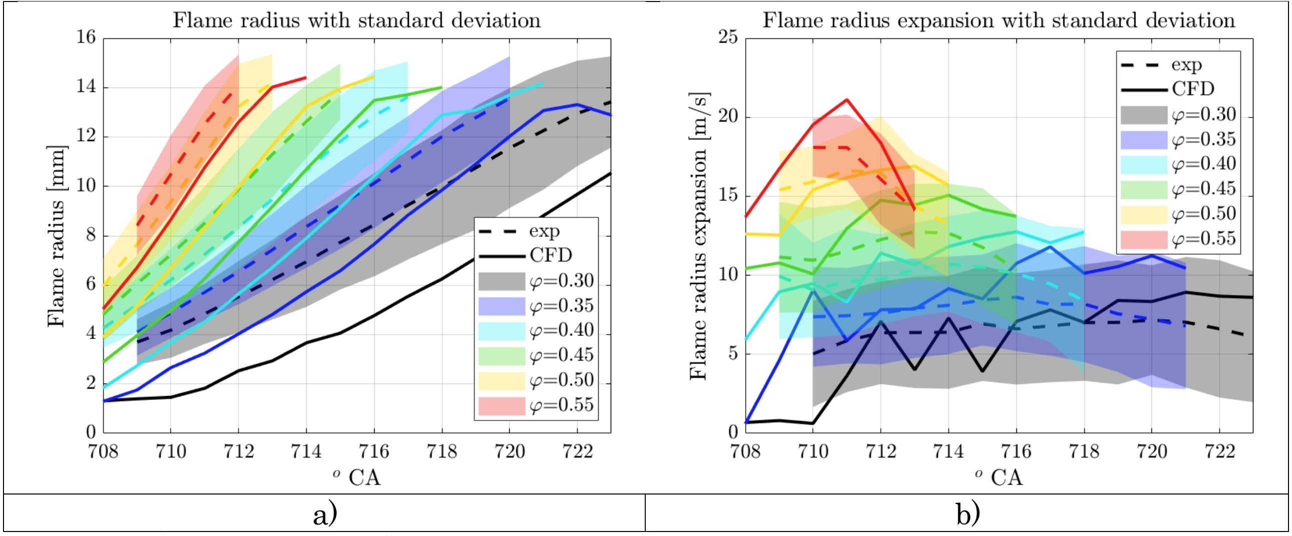

a) b)

Figure 54: a) flame radius and b) flame radius time derivative, both as a function of crank angle, for each case of the φ sweep at intake pressure 0.7 bar. Numerical data (dotted lines) are compared with experimental ones (solid lines), with the latter including a ±2σ band [24].

The observation that the results still align without instability modelling is noteworthy, yet explainable; the following section will be dedicated to this analysis. Based on previous activities described in chapter 2, this behaviour did not appear to be linked to the calibration of the turbulent flame speed. Similarly, the current study suggests that it is not due to the ignition calibration either, which shows good agreement with the experimental imagery.

3.3. Combustion regime analysis

In this section, the combustion regime is also analysed. As previously mentioned, defining this regime is far from trivial given the unique properties of hydrogen. This analysis is fundamental to verify the actual applicability of a flamelet model, an assessment not yet performed and, above all, to attempt a definition of combustion regime that remains robust for lean hydrogen combustion. This will be particularly relevant for the final section of this work, where the definition of a Karlovitz number will be central to the discussion on the influence of flame instabilities.

Internal combustion engines often exhibit "flamelet" combustion, for which the G-equation model (as implemented in the adopted software) is developed and widely adopted [47]. The goal of this section is, on the one hand, to confirm the presence of "flamelet" combustion in the investigated cases. On the other hand, it is necessary to examine the applicability of the consolidated combustion regime classification methods and to verify potential modifications proposed in the literature that can enhance their accuracy. The analysis is carried out by means of the Borghi-Peters diagram as presented in [47], since it is a well-consolidated tool to classify the combustion regimes of hydrocarbon fuels.

More specifically, one of the criteria to classically individuate combustion regimes is that the combustion moves from "flamelet" to "thin reaction zones" for Karlovitz number (Ka) greater than 1, i.e. above the so-called Klimov-Williams limit defined by the condition Ka=1. This criterion is obtained through a series of assumptions [82], [83], among which Lewis number equal to 1, which is not the case of lean H_2/air mixtures. If the hypotheses are not respected, the combustion classification can be misleading. This is confirmed by Aspden et al. in [66], who vary the equivalence ratio of a lean hydrogen-air mixture (and, so, the Lewis number) and, although the Damköhler (Da) and Karlovitz numbers are kept constant, the combustion regime shifts from "thin reaction zone" to "broken reaction zones". The findings proposed by Aspden et al. point out the limitations of the combustion regime classification proper of hydrocarbon fuels when applied to lean hydrogen combustion. In response, the same authors propose a modification to the classical definitions of Da and Ka, by computing these numbers via freely propagating flame properties instead of laminar ones. This approach allows them to obtain coherent results, i.e. when varying the Lewis number while keeping Ka and Da constant, the DNS simulations consistently exhibit the same combustion regime across the different conditions. This means that, by adopting ad-hoc definitions of Da and Ka, the Borghi-Peters diagram could be still adopted for classification of combustion regimes.

In the light of the discussion above, in the present work the Borghi-Peters diagram is presented both in its original form and in the modified version based on the approach proposed by Aspden [66]. The comparison between original and modified diagrams is shown in Figure 55. The modified ones feature different axis names, where the additional subscript 'F' indicates the freely propagating flame properties. Such properties, namely laminar flame speed and thickness, are computed through the correlations proposed by Howarth [11] (Equations 23, 24). For completeness, in each operating condition, the initial marked point represents the combustion start and the line is the evolution of the regime during the combustion process. Each point of the line represents a different CA and it is obtained by calculating the average combustion regime on the reaction zone. It can be observed that both versions of the diagram cover a wide range of conditions, although the spread is narrower in the corrected version. In both the diagrams, the combustion traces extend beyond the formal applicability limits of G-equation. However, the corrected version exhibits an overall shift of the traces toward the "flamelet" combustion regime. For instance, the two cases at $\varphi = 0.35$ move from being entirely within the thin reaction zones to partially entering the "flamelet" regime.

	Original	Modified
Intake pressure 0.7 bar	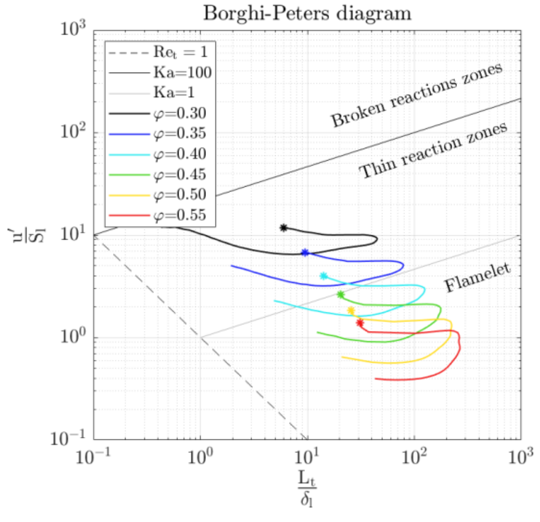	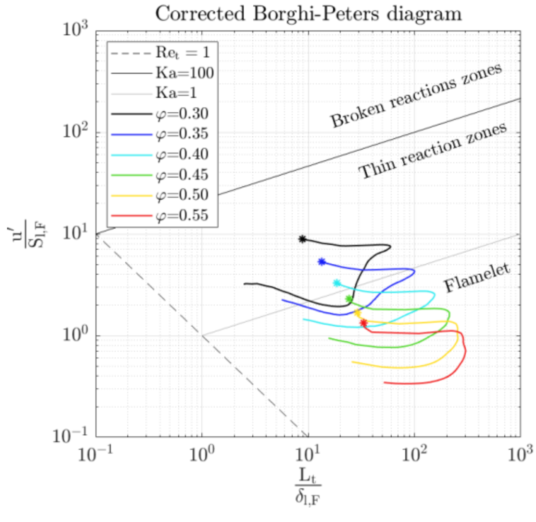

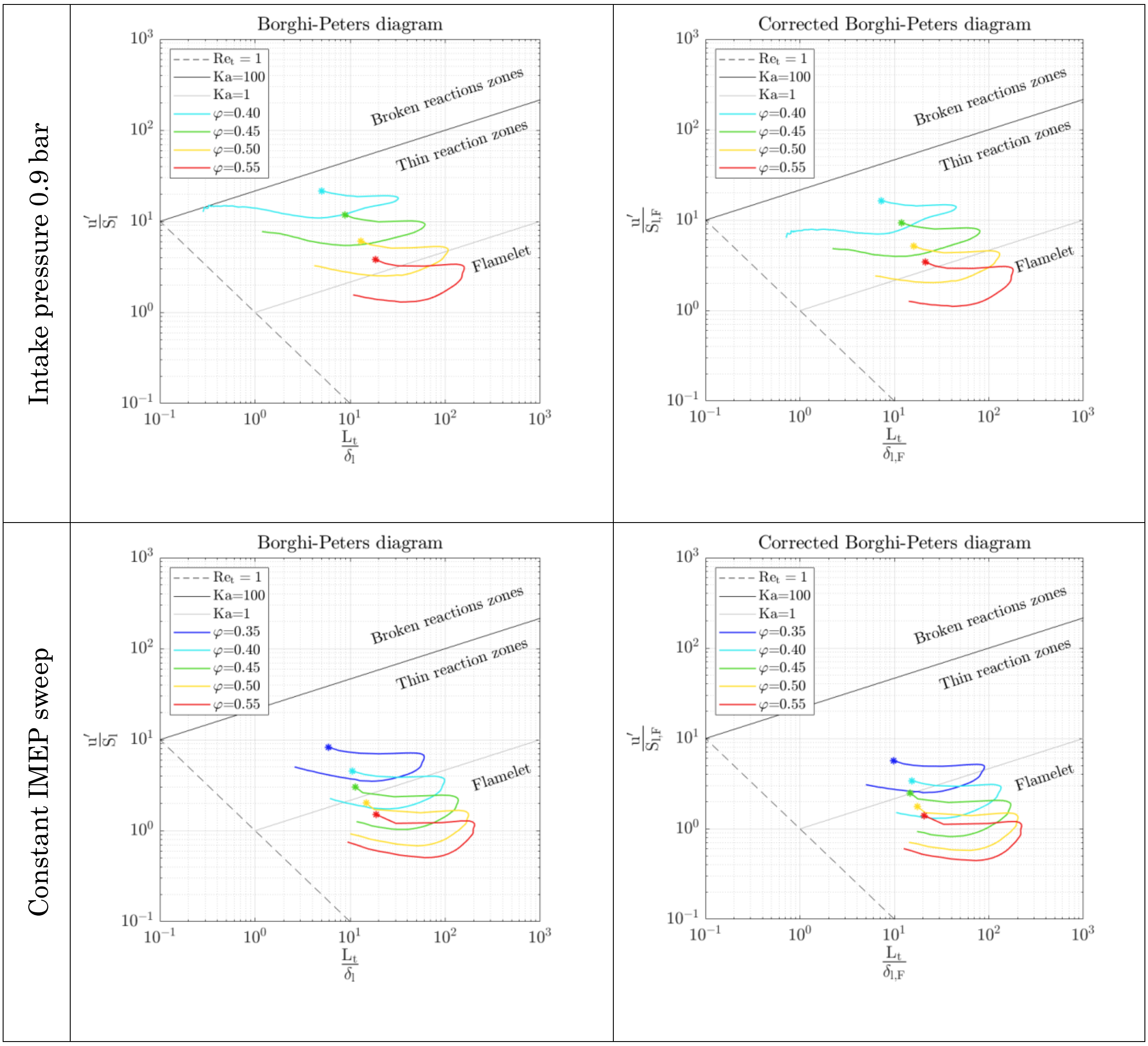

Figure 55: Borghi-Peters diagrams for all the investigated cases. On the x-axis, the ratio of integral length scale to laminar flame thickness L_t/δ_l is reported, while the ratio between turbulent velocity fluctuations and laminar flame speed u'/S_l is reported on the y-axis [24].

Although the use of the adopted combustion model is not strictly valid given the results proposed in Figure 55, G-equation combined to a Damköhler-like correlation is able to reliably predict the combustion evolution for all the investigated cases, as demonstrated in the previous paragraph. This capability is confirmed by experimental observations of the authors of the present work on the same engine. In the experiments proposed in [84] and carried out at 1200 rpm, with φ values from 0.25 to 0.55, a wide range of conditions is covered. As a consequence, although the corrections move all the operating points outside the “broken reaction zones” regime, the flame occupies different regions of both the original and modified Borghi-Peters diagrams. As for the Karlovitz number, the original and modified formulations span four and three orders of magnitude (from 0.025 to 178 and from 0.034 to 70), respectively. Despite the very different conditions, the authors show that the behaviour of the flame can be represented by a single Damköhler-like correlation, similarly to the numerical simulations. More in detail, Figures 56 a) and 56 b) show the original and modified Borghi-Peters diagrams with the experimentally investigated conditions. Each point represents an operating condition, and it is calculated when the flame front has an equivalent radius of 8 mm. For the calculation of the points (i.e. the positioning inside the diagram), the flame speed and thickness are computed through a kinetic solver, using the Burke mechanism. The turbulence intensity u' is estimated using the Heywood method [85], that provides values well aligned with the ones obtained by 3D-CFD simulations. The Heywood method is based on a correlation between mean piston velocity and turbulence intensity measured experimentally via laser Doppler anemometry. The integral length scale L_t is computed by particle image velocimetry (PIV) measurements across different CA and on different planes, and it coincides with the integral of the autocorrelation of the velocity field between zero and the first zero-crossing, as suggested by Pope [86]. A more detailed description of the experimental aspects can be found in [87].

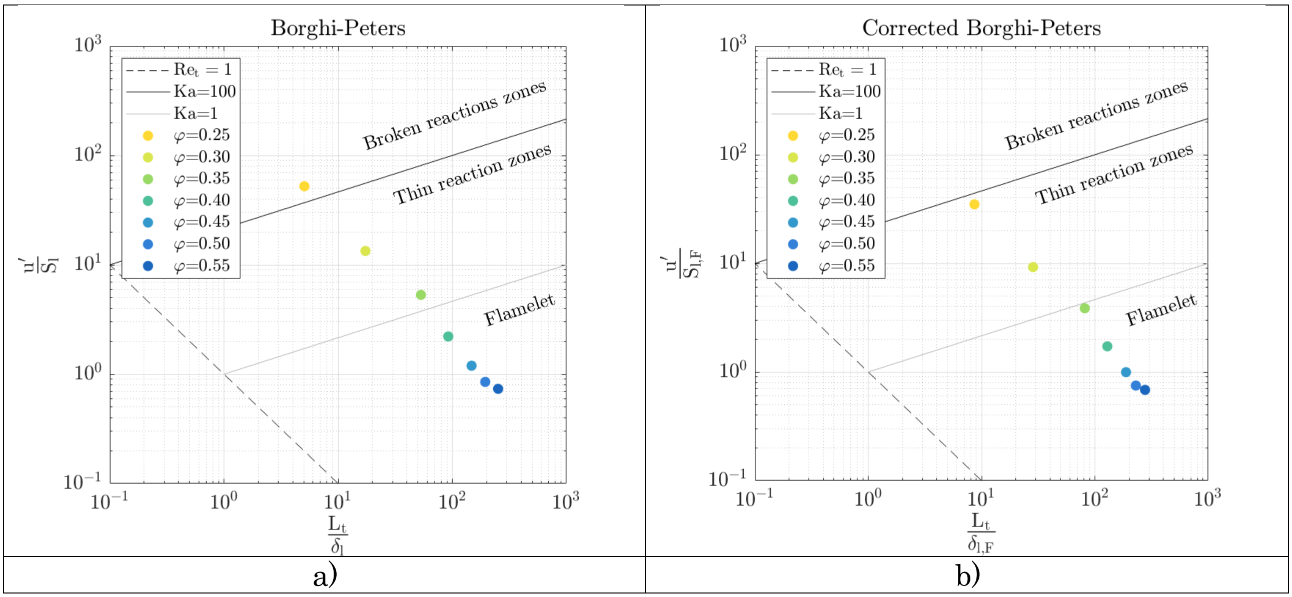

a) b)

Figure 56: Original a) and modified b) Borghi-Peters diagrams for the experimentally tested conditions [24].

For each of the points of Figure 56, it is possible to correlate the ratio between turbulent flame speed directly measured through the optical window and laminar flame speed S_l with the quantity u'/S_l, by adopting the Damköhler-like correlation presented in Figure 57 a), where the constants A and n are shown as well. The turbulent flame speed is estimated as $\frac{\rho_b}{\rho_u} \cdot \overline{v}_t$, where the fraction is the ratio of the burnt density to the unburnt one and $\overline{v}_t$ is the measured flame expansion velocity computed by the flame images. In Figure 57 a), it is evident that a single correlation is able to properly fit all the experimentally-derived values and this is true considering also the modified quantities, as visible in Figure 57 b). Moreover, apart from the coefficients, the correlation is de facto coincident with the one adopted on the CFD side. In this regard, by comparing the experimentally-derived coefficients to those used in the numerical simulations, the exponent n values are similar. Conversely, A coefficient non-negligibly differs. The reasons for the discrepancy are multiple. For instance, laminar flame speed computation methods differ between experimental activity and 3D-CFD simulation. The former relies on the Burke mechanism, while the latter exploits the Konnov one. Anyway, regardless of the differences in the coefficients, the most important aspect is that both CFD and experiments agree on the fact that a single correlation to be formally adopted for "flamelet" combustion can be proficiently adopted at different regimes. This apparent contradiction can be explained in two different ways. Firstly, it is possible that the modifications proposed by Aspden are still not sufficient to obtain a proper classification of the combustion regime. Therefore, all the investigated conditions may actually fall in the "flamelet" regime. A second explanation can be due to the fact that, since the adopted Damköhler-like correlation is able to match the flame speeds in both "flamelet" and "thin reaction zones" regimes, the use of that expression within G-equation leads to proper predictions in both areas of the Borghi-Peters diagram. In other words, it is the capability (thanks to shape and/or tuning) of the turbulent flame speed correlation that compensates the deficiency of G-equation in the “thin reaction zones” regime. This clarification will be addressed in a future work.

It is worth noting that the experimental fitting shown in Figure 57 (whose validity may be reasonably extended at ultra-lean conditions, i.e. out of the “flamelet” regime, as discussed above) does not account for flame instabilities. Therefore, the proposed experiments seem to support the numerical evidence that, at the investigated conditions, combustion indicators can be accurately matched without considering flame instabilities. As anticipated in the numerical setup section, the main reason is related to the turbulence impact on the flame which overcomes the flame instability one.

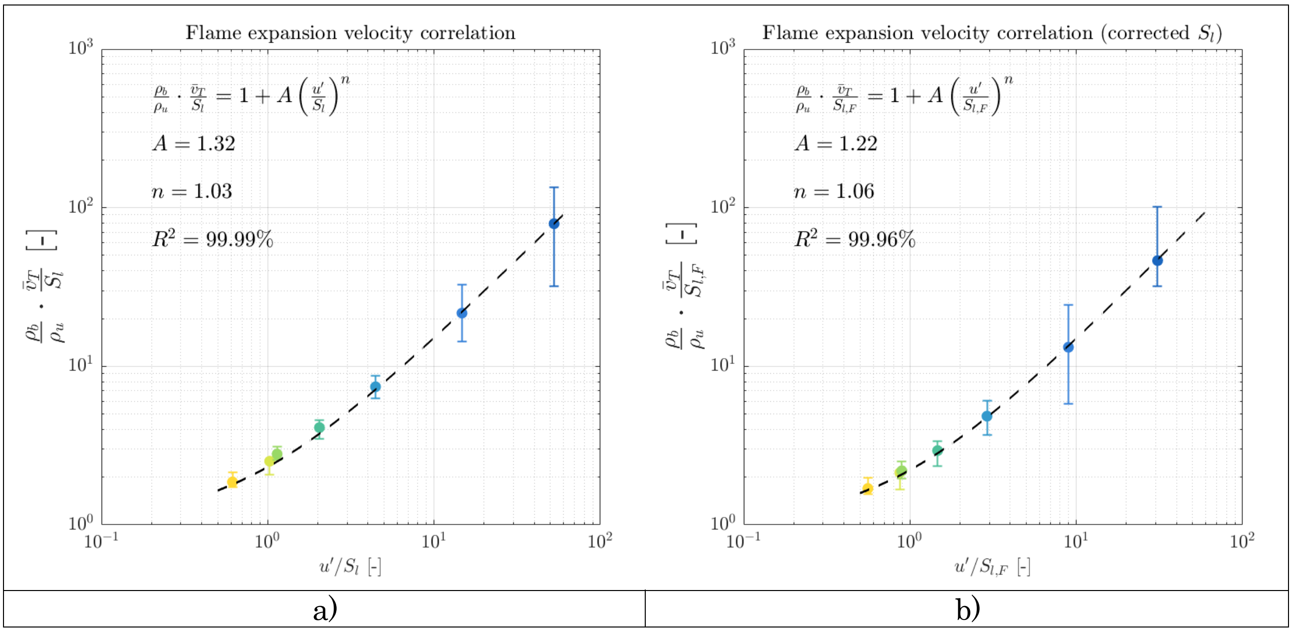

a)	b)

Figure 57: Damköhler-like fitting for the experimentally-measured flame expansion speed values. Different colours are related to different equivalence ratios, as described in the legend of Figure 56. The fitting is proposed for both original a) and modified b) quantities [24].

Chapter 4. Flame instability effect.

Having better defined a way to describe the combustion regime in lean-hydrogen combustion problems, it is now possible to try describing the effect of instability by including its sub grid modelling, according to the description previously given. It is here anticipated that another sub-model will be employed, representing wall flame quenching. This is the only part of the whole URANS activity that employed such sub-model, thus its functioning is here briefly detailed. The results are reported afterwards, for simplicity, for the sole sweep at 1500 rpm and intake pressure 0.7 bar, and are therefore referred to cases 1-6 of Table 6. The results will be presented gradually, at each integration of the original framework, in order to improve the clarity understating the effect of each sub-model individually (flame instability, turbulence instability dampening, wall flame quenching).

4.1. Wall flame quenching modelling

A simplified method is adopted to model the wall flame quenching. It relies on Equation 33 [88], which calculates the quenching distance l_q. For any cell centroid, if the wall distance is smaller than l_q, S_l is adopted instead of the turbulent one.

$$l_q = f_q\left[11.5\mu/\left(\rho C_\mu^{0.25} tke^{0.5}\right)\right] \quad (33)$$

In Equation 33, f_q is set to 1, following [88]. The other variables are density ρ, molecular viscosity μ, turbulent kinetic energy tke, and turbulent viscosity constant C_μ. The value 11.5 corresponds to the dimensionless wall distance (y^+) value defining the (ideal) transition between the viscous sub-layer and the log-region within the boundary layer. In practice, the model assumes that, when y^+ is lower than 11.5 (i.e. the cell centroid pertains to the viscous sub-layer), the impact of the turbulence-induced flame stretch is negligible. This is a simplification of the Bruneaux model [89], which applies a correction to the integral length scale for y^+<50, recognizing that vortices larger than their wall distance are unlikely to persist.

4.2. Results with instability sub-model

Figure 58 reports numerical and experimental in-cylinder pressure, for each of the studied cases (1-6 Table 6), obtained with the basic framework with the addition of flame instability sub-model only. With respect to the 'base' setup (whose results are added in Figure 58 for comparison), the predicted pressure traces are moderately affected by flame instability. To explain this behaviour, the numerical traces are coloured by the increment ($S_{L_{instab}}/S_L$) that the unstretched S_l undergoes when corrected, according to Equation 23, and they are reported in Figure 59. Coherently with the existing literature, the impact of the flame instability is strong for very lean mixtures. However, it is remarkable only towards the end of combustion, when the unburnt temperature decreases (i.e. when the stabilizing effect of temperature is less and less able to compensate the destabilizing one of pressure). Therefore, the effect on performance, namely in-cylinder pressure, is limited. It should be noted that if the combustion is fast enough, the end of the process is reached early in the power stroke, i.e. when the unburnt temperature is still high. This is the reason why the instability effect weakens rapidly, moving from φ=0.30 to φ=0.55. In other words, the instability impact reduces twice when moving towards stoichiometry. Firstly, because of the effect of the equivalence ratio and secondly, because the combustion ends sooner in the power stroke, i.e. when the unburnt temperature is higher and the stabilizing effect results stronger.

By comparing Figures 58 and 59, it is possible to notice that the effect of instability on the pressure traces is comparable, although the S_l correction is strongly different for the cases. This is evident by comparing, for instance, φ=0.30 and φ=0.55. The reason is triple. Firstly, the pressure values of the traces are very different, so a similar variation in absolute terms implies a significantly different variation in percentage. Therefore, the pressure modification for the leanest cases is higher. Secondly, an increase in S_l does not correspond to an equal increase in turbulent flame speed, which is much lower. Therefore, significant variations of laminar flame speed do not correspond to similarly large variations of burn rate and in-cylinder pressure. Thirdly, the instability effect manifests towards the combustion end, when the heat release rate is already low and any acceleration of it does not relevantly affect the pressure trace.

Finally, again comparing Figures 58 and 59, it is evident that the effect of instability on in-cylinder pressure does not match, in terms of phasing, the peak of laminar flame speed correction. For instance, considering φ=0.40 case, the pressure rise is concentrated in the first part of the combustion, when the S_l correction is lower. The reason is that both laminar flame speed and its correction are great enough to lead to a visible effect on the in-cylinder pressure trace at the beginning of the combustion. Moving towards the end of the process, S_l is much more accelerated but, similarly to the above, the effect becomes difficult to observe, due to the low heat release rate during the combustion completion.

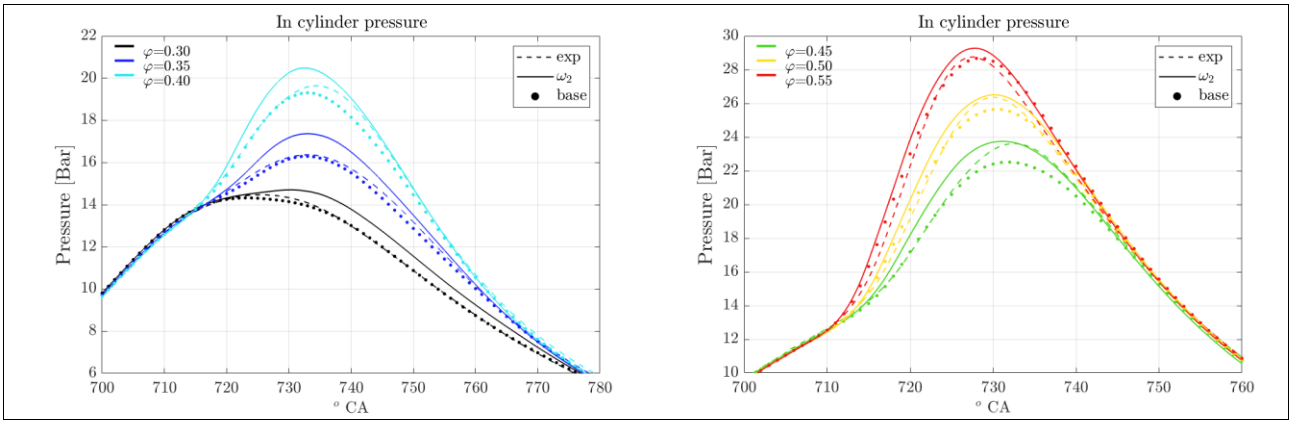

a)	b)

Figure 58: numerical-experimental comparison in terms of in-cylinder pressure, for each investigated condition. Two sets of CFD results are presented, i.e. ones obtained with the 'base' setup (Base) and ones obtained with the 'base' setup with the addition of the flame instability effect (ω_2). The sweep is split in two figures, a) and b), for improved readability [22].

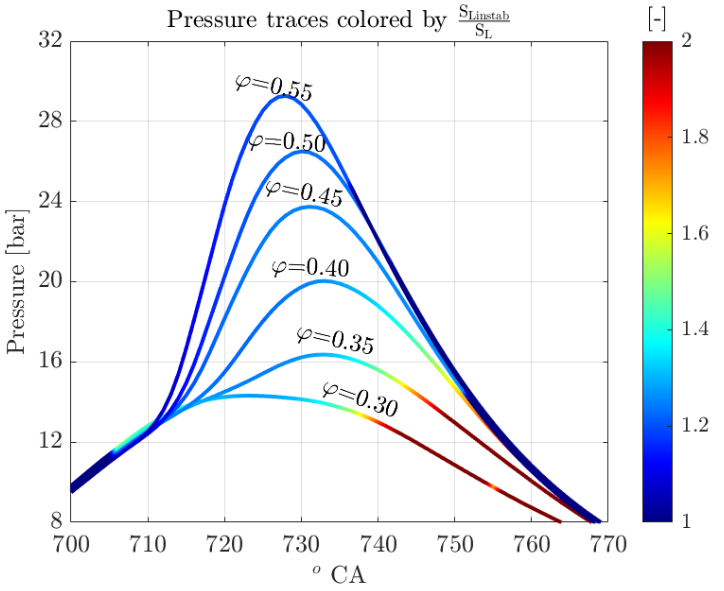

Figure 59: computed pressure traces coloured by the average percentage correction to the unstretched laminar flame speed. For completeness, pressure traces are coloured from MFB 0 to MFB 99 [22].

In order to better appreciate the effect of the flame instability compared to the 'base' setup, experimental and numerical AHRRs are reported in Figure 60. It is possible to observe that, compared to the CFD outcomes proposed in Figure 50b), all the predicted combustions are now shorter and their phasing is advanced. As for the leaner cases, also the combustion end is particularly anticipated compared to the experimental counterpart.

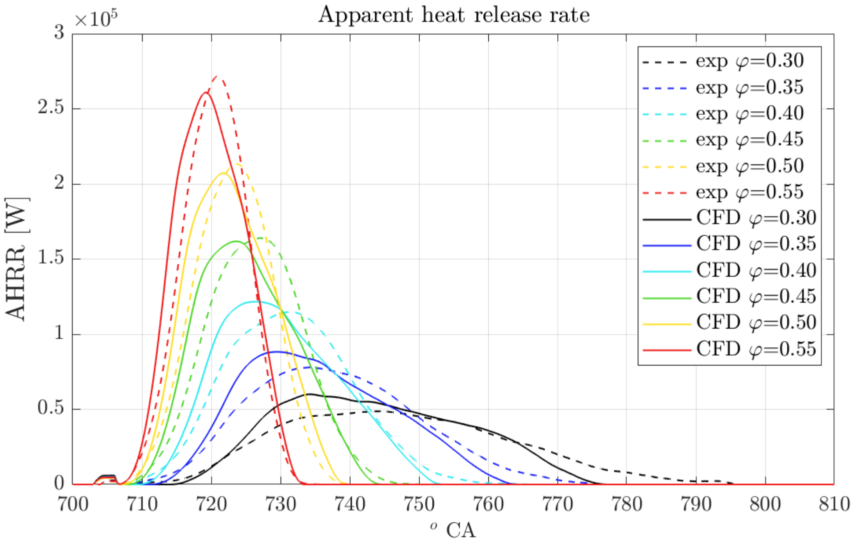

Figure 60: Comparison in terms of AHRR between CFD and experiments. CFD results are obtained with the 'base' setup with the addition of the flame instability effect (ω_2) [20].

A final observation concerns the applicability of the instability correction factor within a URANS framework. The turbulence-induced variability contributes to cycle-to-cycle differences not only by means of the unstretched laminar flame speed (which varies with the thermodynamic conditions), but also by the flame instability itself (which depends on the thermodynamic conditions as well). This further amplifies the spread of the pressure traces between the cycles. The question is if the calculation of the flame instability effect for the average cycle calculated by the URANS approach makes sense. In fact, faster-burning cycles may be influenced by flame instability differently compared to slower-burning ones. Therefore, although the experimental cycles are averaged using a simple linear method, the flame speed predicted by the URANS approach for a single representative cycle does not necessarily correspond to the flame speed of the linearly-averaged experimental cycle. Nevertheless, the URANS approach remains meaningful because, in premixed combustion cases like the investigated ones, the thermodynamic conditions at a given crank angle slightly vary from cycle to cycle. As a result, the corresponding laminar and turbulent flame speeds modify almost linearly between the cycles. The same is valid also for the flame instability contribution. Although it introduces further non-linear effects, the limited differences between the thermodynamic conditions of the cycles lead to variations of the instability contribution that can be approximated as linear. Moreover, the opposed influences of pressure and temperature on the flame instability correction factor help to limit its variation across the different engine cycles. In order to prove this, Figure 61 presents the scatter of the experimental pressure traces for the $\varphi = 0.30$ case, purposely selected as it is the one with the highest cycle-to-cycle variability. The pressure traces of two URANS cycles are reported as well, aiming at mimicking the slower and the faster experimental cycles by the adjustment of the spark timing. This method is used coherently with the origin of the cycle-to-cycle variability for this operating point. In fact, it is mainly originated during the early stage of combustion, by the variability of the flow field at the spark. This is confirmed by a dedicated LES analysis which is currently ongoing on the operating point. The CFD traces are coloured by the laminar flame speed correction factor, which shows consistent values for the two curves. Therefore, for each crank angle, the variation of the flame instability effect (i.e. the variation of the correction factor) can be reasonably assumed as linear.

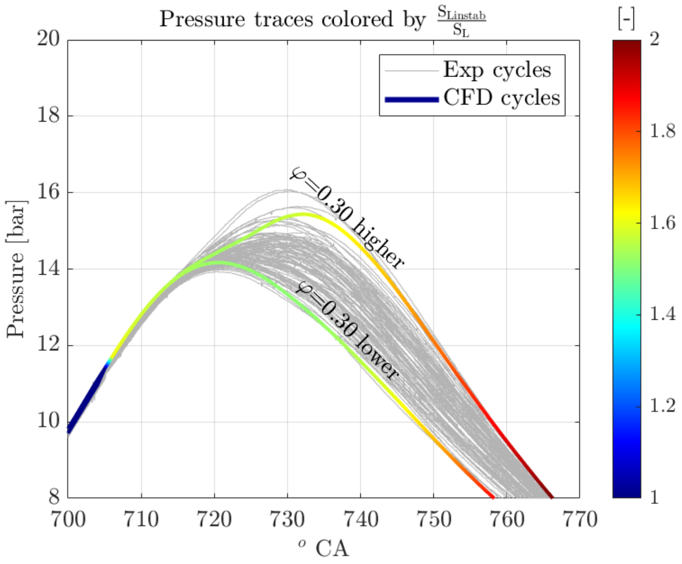

Figure 61: Scatter of the experimental cycles for φ =0.30 case. Two CFD cycles coloured by the laminar flame speed correction factor are reported as well [22].

4.3. Results with instability sub-model and turbulence dampening

The Karlovitz stretch factor is now introduced to consider the interaction between flame instability and turbulence. In particular, it allows to distinguish the cases in which the flame instability has an impact (i.e. it is possible to recognize its effect) from those in which it is negligible, with respect to turbulence. The mass-averaged value assumed by this parameter on the flame front cells is plotted in Figure 62, during combustion, for each case.

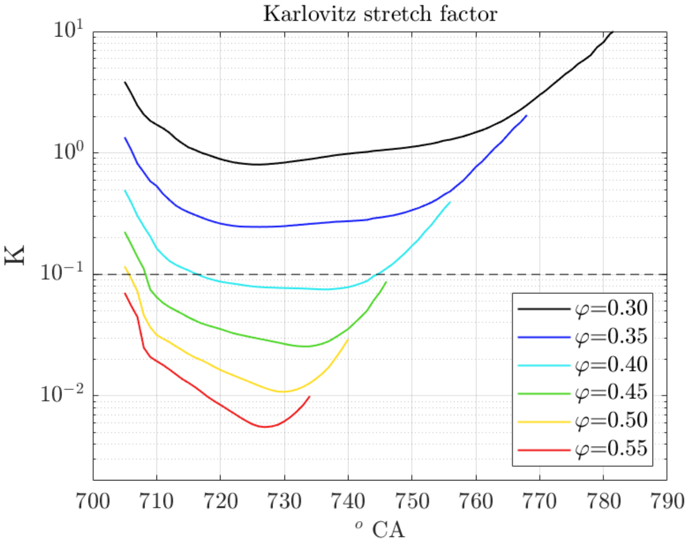

Figure 62: Mass-averaged Karlovitz stretch factor on the flame front cells, during combustion, for all the cases [20].

The combination of threshold suggested by Bradley ($K = 0.1$) and S-shaped function splits the cases in three groups. The first one includes φ=0.30 and φ=0.35 and it is characterized by a chemistry that is so slow that the instability-induced wrinkling is secondary compared to the one due to turbulence. φ=0.45, φ=0.50 and φ=0.55 pertain to the second group, in which the actions of both instability and turbulence coexist. The third group comprises the remaining case, namely φ=0.40, which is characterized by K values that move across the threshold, thus undergoing the effect of the S-function (Equation 27). In this regard, it is necessary to point out that, based on the adopted values for the parameters governing centre and width, the S-shaped function mainly acts on the φ=0.40 case, while the impact on φ=0.45, φ=0.50 and φ=0.55 ones is negligible. In the light of these clarifications, φ=0.45, φ=0.50 and φ=0.55 cases are mainly characterized by the use of $S_{L\ instab}$, while S_L is mostly adopted by the code for φ=0.30 and φ=0.35 simulations. Finally, φ=0.40 case rely on a blend of the two flame speeds. The results in terms of in-cylinder pressure obtained by introducing the effect of the Karlovitz stretch factor are presented in Figure 63. In order to highlight the effect of K, in the same figure also the results without it are reported. In Figure 63 a), it is evident that K acts in φ=0.30, φ=0.35 and φ=0.40 cases. Moreover, by comparing Figures 63 and 50 a), it is possible to notice that, due to the action of K, the instability effect is de facto neglected at φ=0.30 and φ=0.35, while it is still visible in the other ones. As for the φ=0.40 case, the pressure trace is characterized by values that are lower compared to the previous setup ('base' with instability effect) but higher with respect to the 'base' one, which demonstrates the action of the S-shaped function.

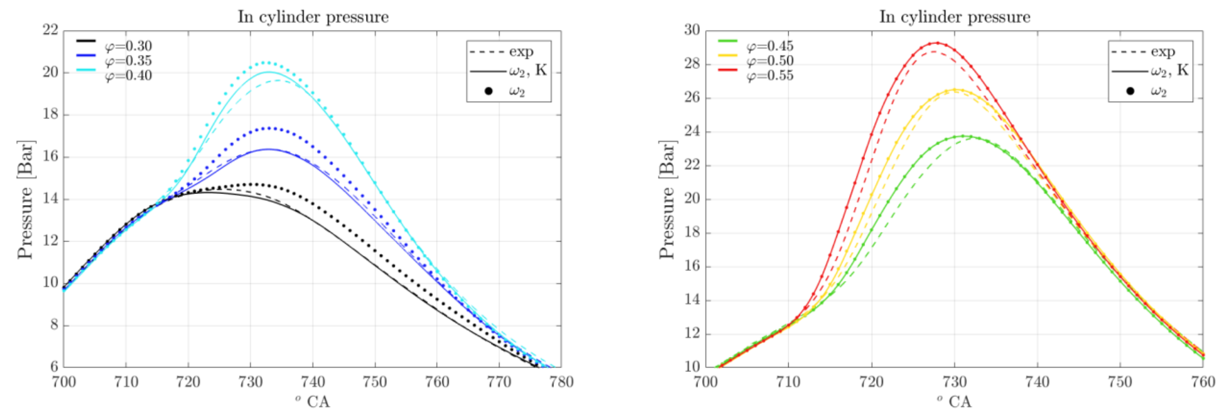

a)	b)

Figure 63: Numerical-experimental comparison in terms of in-cylinder pressure, for each investigated condition. Two sets of CFD results are presented, i.e. ones obtained with the 'base' setup with the addition of the flame instability effect (ω_2) and the ones obtained with 'base' setup and adding the effect of both flame instability and Karlovitz stretch factor (ω_2, K). The sweep is split in two figures, a) and b), for improved readability [22].

Figure 64 reports the numerical AHRR traces, obtained with the setup including flame instability effect and K, and the experimental ones. AHRR traces allow to point out the benefits related to the introduction of K. The agreement improvement is confirmed for φ=0.30, φ=0.35 and φ=0.40 cases. As shown in Figure 50 b), in fact, the adoption of the flame instability effect alone is strongly penalizing for these cases. As for the remaining ones, K does not act and no difference can be noticed between Figures 50 b) and 64.

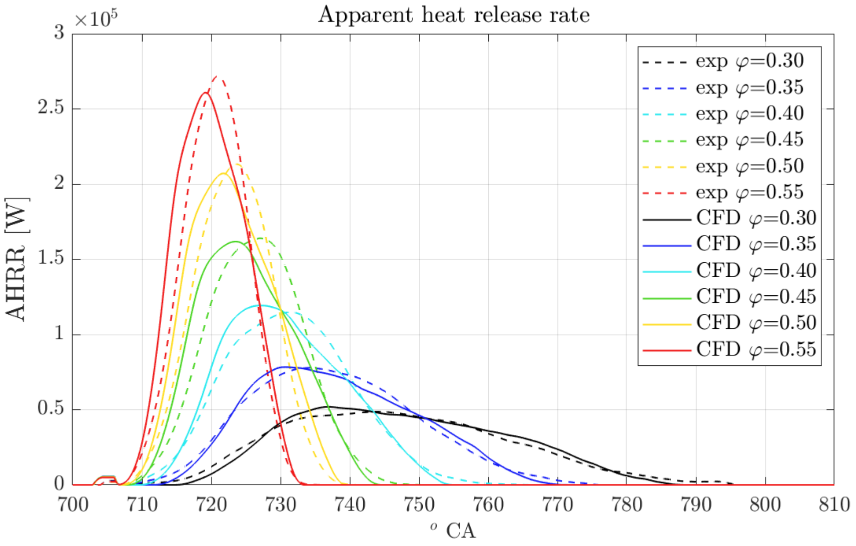

Figure 64: Comparison in terms of AHRR between CFD and experiments. Results are obtained with the ' base' setup and adding the effect of both flame instability and Karlovitz stretch factor [22].

As previously mentioned, there are two parameters defining the S-function, equal to 100 and 0.1, respectively. The first one determines the slope of the S-curve and it is used as a calibration parameter. The second one corresponds to the threshold value of K. It is inherited from the literature, and it is not varied in this analysis. To assess the sensitivity to the slope, additional simulations are performed with values equal to 50 and 10˙000. As visible in Figure 65, varying this parameter alters the sharpness of the transition, thus affecting how quickly the laminar flame speed changes (from S_L to $S_{L\,instab}$) for the cases whose K is close to the threshold.

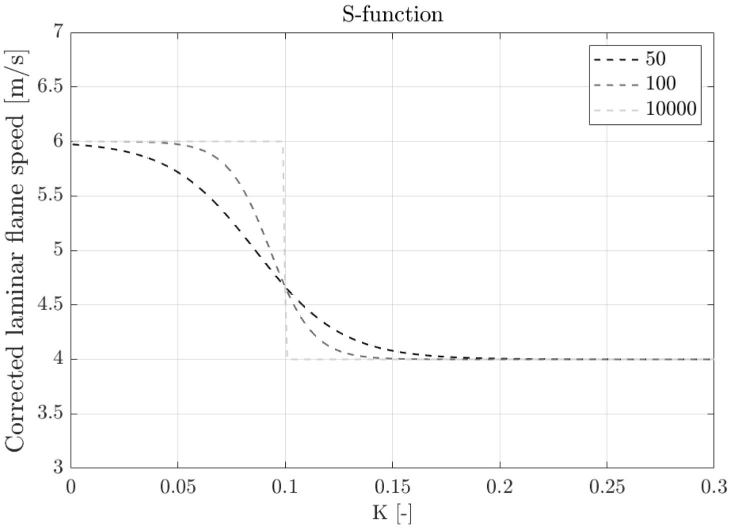

Figure 65: S-function sensitivity to the slope [22].

The sensitivity analysis is conducted only for φ=0.35, φ=0.40 and φ=0.45 cases, as these are the ones falling, on average, close to the $K = 0.1$ threshold. Figure 66 shows the pressure traces for these cases using the three different S-function slopes. The impact is minimal, and only the case closest to the threshold, i.e. φ=0.40, is affected. The effect on it is to slightly inflate the pressure trace, as a consequence of the sharp transition between the regimes that allows for advanced onset of instability. On the other hand, φ=0.35 case remains almost completely confined in the fully turbulent regime, while the φ=0.45 case is almost entirely affected by flame instability during all the cycle.

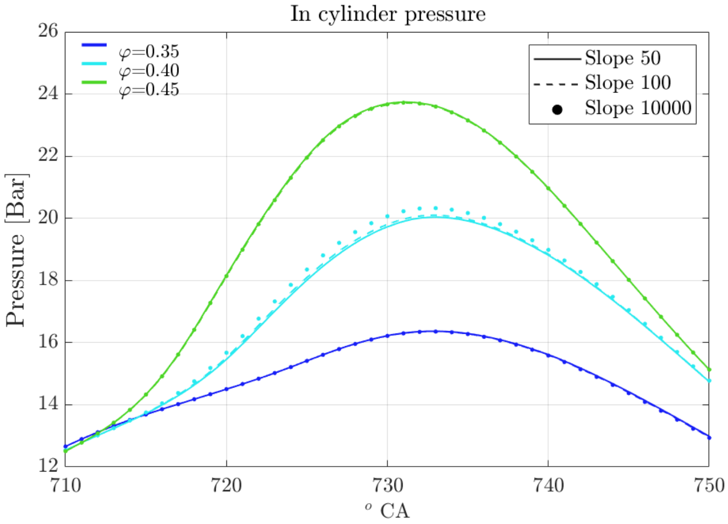

Figure 66: Sensitivity of the CFD pressure traces to the 'slope' parameter of the S-function, for φ=0.35, φ=0.40 and φ=0.45 cases [22].

4.4. Results with instability sub-model, turbulence dampening and wall flame quenching

As a final step of setup refinement, the wall flame quenching sub-model is introduced. The results obtained with the final framework including all the sub-models are reported in Figure 67, in terms of average in-cylinder pressure, along with experiments and results obtained without quenching. As visible, the introduction of flame quenching leads to minimal variations of the results. The pressure peaks of φ=0.50 and φ=0.55 cases slightly improve, as the instability effect is partly compensated. As for φ=0.30 and φ=0.35, the quenching effect causes a weak underestimation of the of experimental trace during the expansion stroke. Despite this negative aspect, the effect on the apparent heat release rate (AHRR) tail is positive, as it will be pointed out in the following.

By comparing Figure 67 with Figure 50 a), it can be noted that the results of the 'base' setup and the one including instability, turbulence dampening on it and wall flame quenching are similar. This means that prevailing turbulence effects and wall quenching of the flame roughly compensate the impact of the flame instability. However, compared to the 'base' setup, an improvement in the peak pressure prediction is visible, especially for φ=0.45 and φ=0.50 cases.

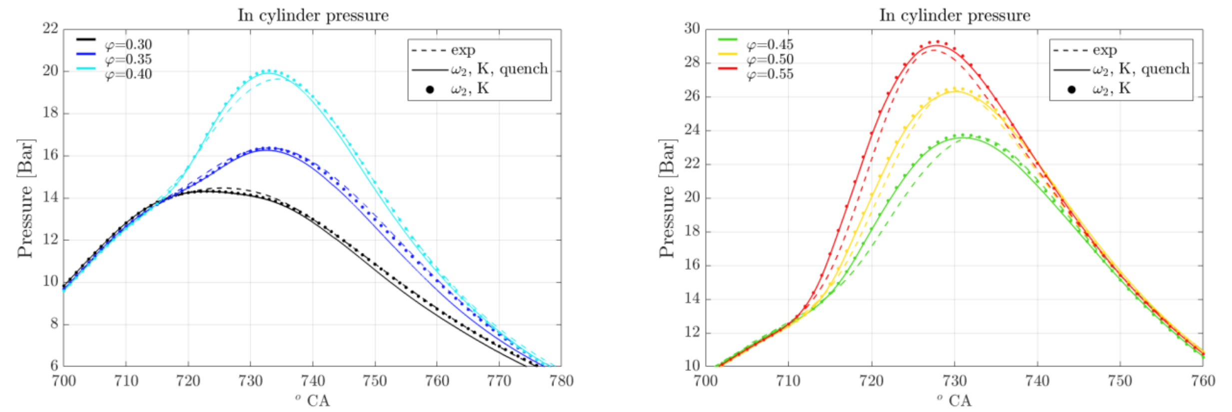

a) b)

Figure 67: numerical-experimental comparison in terms of in-cylinder pressure, for each investigated condition; Two sets of CFD results are presented, i.e. ones obtained with 'base' setup and the effect of both flame instability and Karlovitz stretch factor (ω_2 K), and ones obtained with the 'improved' framework, featuring all the sub-models (ω_2 K quench). The sweep is splitted in two figures, a) and b), for improved readability [22].

To better describe the results achieved with the final ('improved') version of the setup and point out the predictive capabilities, the numerical results in terms of AHRR and combustion indicators are compared with the experiments. Figure 68 reports a comparison between CFD and experiments in terms of AHRR, for each case. A good agreement is noticed, especially for the combustion completion, thanks to the action of both instability and quenching. In particular, φ=0.30 and φ=0.35 are characterized by the action of the flame quenching that extends the AHRR tail and allows a close agreement with the experiments to be obtained. As for the other cases, apart from quenching, the flame instability is present, leading to a progressive shortening of the tail, visible also in the experiments. The correct modelling of the combustion completion also represents an improvement compared to the 'base' setup. However, there is still room for amelioration. In fact, a slight overestimation of the combustion rate in the first half of the process can be noted, along with a progressively delayed AHRR growth moving to lean mixtures, attributable to the ignition model. In this regard, for a proper comparison, no recalibration of ignition and combustion model parameters is carried out moving from 'base' setup to its last version. A recalibration of the models may lead to further improvements of the results. It is interesting to point out that the small spikes observed at 705° CA result from the initialization of G-equation, which leads to the formation of an initial burnt mass. Such an initialization is a modelling requirement, even though the effective propagation of G begins later, following the delay imposed by the ignition model.

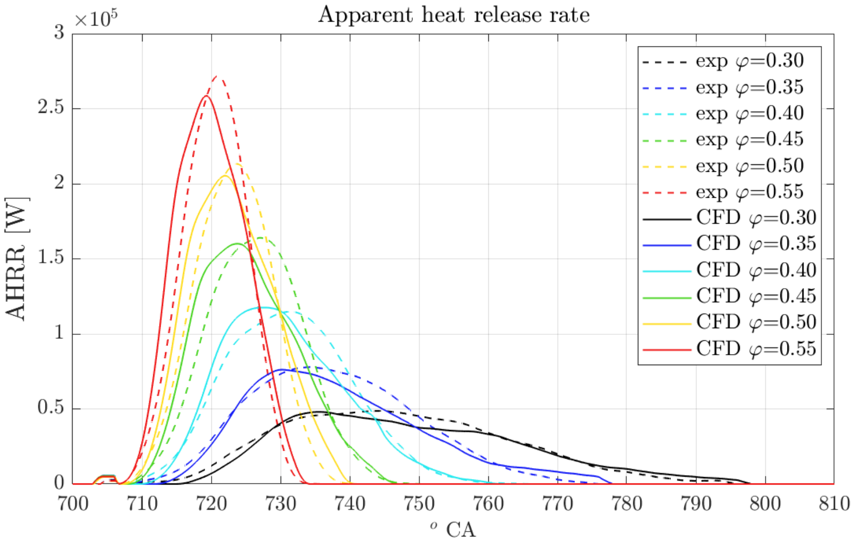

Figure 68: numerical-experimental comparison in terms of AHRR, for each investigated condition; CFD results are obtained with the 'improved' setup, featuring all the sub-models [22].

Figure 69 shows a numerical-experimental comparison of combustion indicators, which provide a more quantitative description of the results discussed above in terms of AHRR. An overall satisfying agreement between CFD and experimental outcomes is noticed. In detail, Figure 69a) shows the MFB 0-10, which confirms that, moving to leaner mixtures, the lengthening of the combustion initiation is slightly overpredicted by the simulations. Figure 69b) reports the MFB 50 and, even in this case, the observations on the AHRR are confirmed. The overprediction of the combustion rate in the first half of the process results in a slight underestimation of the combustion phasing. As for the duration (namely MFB 10-90), Figure 69c) confirms an overprediction of the experiments for all the cases, which is probably due to an overestimation of the quenching effect. However, similarly to the other indicators, the error in the MFB 10-90 prediction is still acceptable.

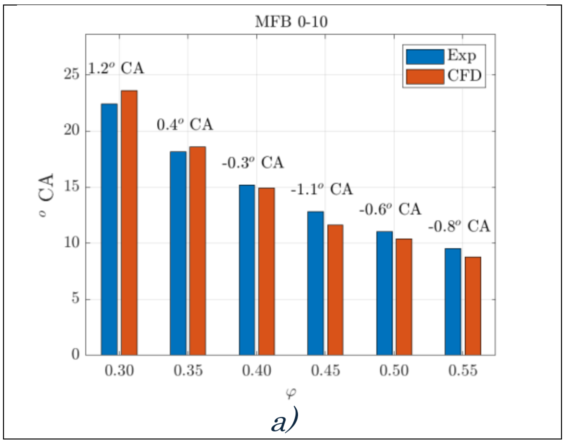

a)

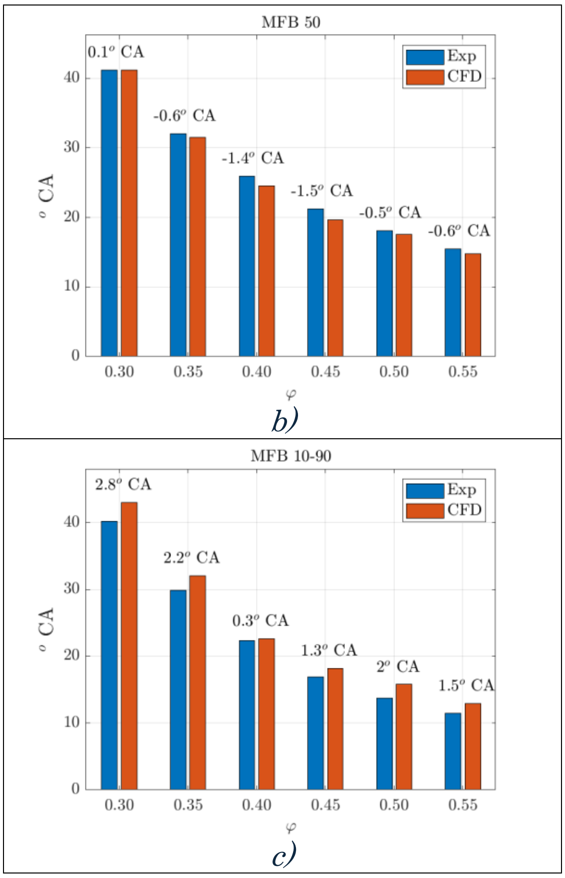

b)

c)

Figure 69: numerical-experimental comparison in terms of combustion indicators, for each investigated condition; CFD results are obtained with the 'improved' setup, featuring all the sub-models; a) MFB 10, b) MFB 50 and c) MFB 10-90 [22].

Thanks to the outcomes of the proposed simulation framework, it is possible to point out the moderate influence of the flame instability and the capability of turbulence-instability interaction and wall quenching to perfectly compensate it. The limited impact of the flame instability is a noteworthy outcome of this work. In fact, following the existing literature [11], [54], [90], the selected operating points presenting extremely lean mixtures and low engine speed should be characterized by a significant effect of the flame instability, that increases the flame speed despite low turbulence. However, pressure and temperature also play an important role and, at the investigated engine-like conditions, the stabilizing effect of the temperature limits the impact of the flame instability.

As a further remark on the results, it is useful to point out the proven predictive capabilities of the proposed numerical framework, especially of the turbulent flame speed correlation and, more in general, of the combustion model. In fact, the investigated conditions cover a wide range of the $\frac{u'}{s_l}$ ratio. The different values are obtained keeping u' roughly constant (as the engine speed does not modify), while changing the laminar flame speed through the variation of the mixture quality. The $\frac{u'}{s_l}$ sweep is particularly relevant not only for the wide range of φ (including conditions potentially affected by flame instability), but also with respect to the turbulent flame speed correlation, which depends solely on $\frac{u'}{s_l}$ itself. A wide variation of this ratio without case-by-case calibration strengthens the robustness of the combustion model, demonstrating the validity of the correlation across very different operating conditions.

Note on authorship and collaborative working

The work described in chapter 2 is a result of the collaborative efforts of the author, dr. Stefano Sfriso of University of Modena and Reggio Emilia and professors Marco Antonelli and Stefano Frigo from University of Pisa. The author carried out all the 3D CFD simulations and analysis, based on the experimental work previously carried out by professors Frigo and Antonelli at University of Pisa in the context of the project “Progetto H_2 filiera idrogeno” concluded in 2012. The work described in chapters 3 and 4 is a result of the combined efforts of the author and dr. Caio Ramalho Leite, from University of Orléans. The author carried out again all the 3D CFD simulations and dr. Caio Ramalho carried out the experimental activity within the “ALEKCIA ANR project” conducted between 2021 and 2025.

Conclusions

Throughout this research, a dedicated framework for in-cylinder URANS simulations was established to characterize the combustion processes in hydrogen-fuelled internal combustion engines. The framework has been thought to be easily implementable through many CFD solvers, and be as general as possible.

The equations encompassing laminar and turbulent flame speed with relative corrections, and the entire ignition model are manually implemented in the software through external Fortran user-coding. As for the equations underlying the flame instability sub-model, they are used in a Python script in conjunction with a kinetic solver (namely Cantera). Output values are then used within the turbulent flame speed computation routine, to correct the unstretched laminar flame speed. No further fundamental change is made to the remaining equations, and all this work may be, in principle, replicated on any other code.

In general, the combustion framework adopted here (intended as combination of ignition, combustion and quenching models, and turbulent flame speed correlation) is well-consolidated for stable premixed (or partially-premixed) flames, thus it can be extended in principle to any traditional fuel. In this regard, it is useful to remember that some tuning parameters such as the turbulent flame speed constant and the threshold kernel radius that governs the transition from ignition to combustion model may require fuel-to-fuel calibration. Additionally, the laminar flame speed must be adjusted to reflect the characteristics of the chosen fuel.

Although the methodology to account for flame instability is fuel-agnostic, the empirical correlation finally linking the corrected laminar flame speed the chemical quantities is fuel-dependent. Therefore, this correlation is specific for ultra-lean H_2 combustion and not directly applicable to other fuels. Also, the approach for the turbulence-instability interaction based on the Karlovitz stretch factor is fuel-agnostic. Even if it is purposely introduced to compare the effect of the H_2 flame instabilities to the turbulence one, it can be adopted in principle with any fuel.

The validation of the framework began with a test across 11 operative points on a retrofitted-to-hydrogen diesel single cylinder engine, sweeping from 1500 to 3000 rpm and equivalence ratios from 0.4 to 0.8. This drove to the calibration of the model, where the value for the calibration constant of the turbulent flame speed was inferred, and never altered anymore. Since the engine under study features a direct injection configuration, it was necessary to address the uncertainties associated with fuel stratification. This was done exploiting another set of operative points, for which the NO_x emissions were experimentally measured. Measures were then used as an indirect index to assess the realism of the mixture distribution represented in the simulations. Simulations, in this case, were run with additional kinetic models to solve in detail the burnt gases composition. Two models were tested to reduce the uncertainty possibly relating specific outcomes to specific kinetic models.

An interesting outcome of this fist part of the activity, was the apparent irrelevant role of lean hydrogen flame instability effect. Without integrating them in the modelling, in fact, all the operating points were close to the experimental target, with the CFD traces correctly predicting the experimental trends. Second part of the activity, thus, involved the modelling of flame instability, on another engine: a PFI single cylinder unit with an optical access, retrofitted from a gasoline unit. In this second engine, operative points didn't sweep as widely as in the previous engine, but they were more narrowly focused on the lean and ultra-lean mixtures, featuring equivalence ratios sweeping from 0.30 to 0.55.

A first overall validation of the model on this new engine, showed the need to slightly calibrate the ignition model with respect to prior engine, but no other calibration was needed. The new calibration of ignition model, moreover, was not altered through all the studied operative points on the new unit. During this activity, the previous outcomes were confirmed: apparently really weak effect of flame instability was observed as, without modelling it, all the points lied close to the respective experimental pressure trace without, in this case, the uncertainty of fuel distribution. This hypothesis was then partially confirmed when the modelling of instability was included in the simulations; not a strong acceleration was induced on the flame, and the operative points at which it should have been stronger were the ones where the turbulence dampening of its effect, due to the thickening of the flame and thus the restriction of the instability spectrum, was stronger. In cases unaffected by this dampening effect, the flame instability was entirely compensated by the wall flame quenching, showing that the magnitude of its effect is in fact limited.

The progressive integration of these sub-models highlights their relative significance at the tested operating points. The combination of relatively low pressure and high temperatures resulted in minimal instability-driven corrections to the laminar flame speed, despite the ultra-lean equivalence ratios. Paradoxically, incorporating instability without accounting for compensating phenomena initially worsened the agreement between CFD and experimental data, indicating that other physical interactions were at play.

By accounting for the damping effect of elevated turbulence, which thickens the flame and inhibits the development of instability spectral components, CFD predictions were brought back into alignment with experimental evidence. This damping was particularly influential in the leanest cases, which simultaneously exhibited the highest potential for instability-driven acceleration and the thickest laminar flames (inhibiting instability development). While specific to these operating points, this suggests a recurring pattern: as mixtures become leaner, the growth of instability is, to some extent, counteracted by the concurrent effects of flame thickening and turbulence damping.

These conditions approach the limits of flamelet model applicability, a common occurrence in ultra-lean operations where chemical length and velocity scales approach turbulent scales. In such regimes, classical combustion parameters definitions may no longer hold, necessitating a revised framework of parameters that more accurately reflects DNS-observed flame behaviour.

Finally, the inclusion of wall flame quenching restored the originally satisfactory agreement between CFD traces and experimental results. Its decelerating action effectively counterbalanced the instability-driven acceleration to produce a high-fidelity match. While this precise balance may be specific to the studied cases, a broader conclusion emerges: at these low IMEP conditions, even when thermochemical factors would favour instability-driven combustion rate enhancement, the net impact on the pressure trace is comparable in magnitude to wall quenching. In those conditions, thus, flame instability acts as a second-order effect.

Recommended future developments

The objective of refining URANS combustion representations, specifically where flame instability significantly alters the combustion rate, presents a complex challenge. Currently, a robust theoretical framework for predicting unstable laminar flame propagation speeds is missing. Consequently, researchers must rely on empirical models derived from DNS data, ideally based on a rational selection of physical parameters.

While the foundational work of Howarth [10], [11] and Berger [58] has paved the way, additional data is required to encompass the wide range of operating points found in ICEs which, at present, are limited to very low IMEP conditions. This data must be generated through 3D DNS, as research indicates a distinct scaling factor, though not yet universally defined, between flame acceleration in 2D and 3D domains.

Once the laminar baseline is established, the interaction with turbulence must be addressed. Current literature offers limited 3D DNS data across varying turbulence levels, necessitating a broader simulation campaign. The coupling between turbulent and instability spectra varies significantly:

1. Full decoupling: in cases where the spectra do not overlap because the smaller turbulence wavelength is larger than the bigger instability wavelength, a simpler 'superimposition of effects' approach may be used. Here, the instability-corrected laminar flame speed is enhanced by turbulence through classical correlations. However, these conditions are rare in ICE environments.
2. Full coupling: in this regime, turbulent eddies can trigger all the spectral components of the instability. This leads to an overall flame speed enhancement greater than the sum of the individual effects, as the phenomena excite one another [59], [63].
3. Interaction and damping: when turbulent wavelengths are smaller than instability wavelengths, eddies penetrate and thicken the flame front. This phenomenon can dampen the instability effect, progressively degrading its accelerating influence. This work implements a modelling approach for such phenomena based on the findings of Bradley et al. [64], [65], where turbulent acceleration persists while the contribution of flame instability is progressively attenuated.

A truly comprehensive turbulent flame speed correlation must integrate all three scenarios:

1. A fully coupled range: spectra are fully coupled, requiring extensive 3D DNS data to fit.
2. A decoupled range: effects are independent and can be superimposed.
3. A damping range: instability correction is progressively eliminated by turbulent action as it disrupts flame coherence.

While this work proposes a method to model the damping regime, further 3D DNS or experimental validation is essential to infer such a complex comprehensive model, able to universally mimic hydrogen flame speed under the different thermochemical and turbulent conditions found during ICEs operations.

Acronyms and abbreviations

Abbreviation	Description
BDC	Bottom Dead Centre
CA	Crank Angle
CFD	Computational Fluid Dynamics
CoV	Coefficient of Variation
CR	Compression Ratio
DC	Detailed Chemistry
EGR	Exhaust Gas Recirculation
ICE	Internal Combustion Engine
IMEP	Indicated Mean Effective Pressure
PFI	Port Fuel Injection
SOI	Start of Injection
TDC	Top Dead Centre
URANS	Unsteady Reynolds-Averaged Navier-Stokes

Latin symbols

Symbol	Description	Unit
A	Turbulent flame speed calibration constant	[-]
Da	Damköhler number	[-]
G	G-equation scalar field (Level-set)	[m]
k	Turbulent kinetic energy	[m^2/s^2]
K	Karlovitz stretch factor	[-]

Ka	Karlovitz number	[-]
Lb	Markstein length	[m]
Le	Lewis number	[-]
Ma	Markstein number	[-]
p	Pressure	[bar] or [Pa]
Re	Reynolds number	[-]
S_l	Laminar flame speed	[m/s]
S_T	Turbulent flame speed	[m/s]
T	Temperature	[K]
u'	Turbulent intensity (r.m.s. velocity fluctuation)	[m/s]
$y+$	Dimensionless wall distance	[-]
f	Frequency or functional relationship	[-]
D_{th}	Thermal diffusivity	[m^2/s]
L_t	Turbulence integral length scale	[m]
k	Wavenumber	[1/m]
$S_{l,instab}$	Laminar flame speed enhanced by instabilities	[m/s]
$S_{l,corrected}$	Final corrected laminar flame speed	[m/s]
Y_i	Mass fraction of the i-th chemical species	[-]
$F_{i,j}$	Diffusion flux of species i in direction j	[kg/(m^2·s)]
S_i	Source term (production/consumption rate) for species i	[kg/(m^3·s)]
M_i	Molecular weight of the i-th species	[kg/kmol]
N	Total number of chemical species	[-]
NR	Total number of elementary reactions	[-]
$k_{f,k}$	Forward reaction rate constant for reaction k	[varies]
$k_{r,k}$	Reverse reaction rate constant for reaction k	[varies]
l_q	Quenching distance (analytical)	[m]
f_q	Quenching calibration factor	[-]
p_{crit}	Critical pressure for sonic flow conditions	[bar]
p_{inlet}	Injector inlet total pressure	[bar]
R^2	Coefficient of determination (statistical accuracy)	[-]
y_i	Measured (experimental) value in statistical analysis	[varies]
$\hat{y}_i$	Predicted (computed) value in statistical analysis	[varies]
$\bar{y}$	Mean value of the experimental dataset	[varies]
C_μ	Standard k-ϵ turbulence model constant (0.09)	[-]

Greek symbols

Symbol	Description	Unit
α	Temperature exponent for laminar flame speed	[-]
β	Pressure exponent for laminar flame speed	[-]
δ_l	Laminar flame thickness	[m]
δ_q	Quenching distance	[m]
ϵ	Turbulent kinetic energy dissipation rate	[m^2/s^3]
λ	Air-excess ratio	[-]
μ	Dynamic viscosity	[kg/(m·s)]
ϕ	Equivalence ratio	[-]
ρ	Density	[kg/m^3]
ω_2	Thermo-diffusive instability correction factor	[-]
$\dot{\omega}_{\iota}$	Net molar production rate of species i (Reaction rate)	[kmol/(m^3 ·s)]
ν'_{ik}	Stoichiometric coefficient of reactant i in reaction k	[-]
ν''_{ik}	Stoichiometric coefficient of product i in reaction k	[-]
ω	Growth rate of flame instabilities	[1/s]
β	Zel'dovich number	[-]
γ	Specific heat ratio	[-]
σ	Unburnt to burnt density ratio	[-]

Subscripts

Subscript	Meaning
0	Reference or initial state
b	Burnt mixture
l	Laminar property
q	Quenching related
T	Turbulent property
u	Unburnt mixture

Bibliography

[1] Gustav Goldbeck, *L'inventeur Isaac de Rivaz (1752–1828) by Henry Michelet (review)*, vol. 7. Johns Hopkins University Press, 1966.

[2] K.-H. Dietsche, “History of the diesel engine,” in *Fundamentals of Automotive and Engine Technology*, Wiesbaden: Springer Fachmedien Wiesbaden, 2014, pp. 8–17. doi: 10.1007/978-3-658-03972-1_2.

[3] W. Peschka, “LIQUID HYDROGEN FUELED AUTOMOTIVE VEHICLES IN GERMANY - STATUS AND DEVELOPMENT,” in *Hydrogen Systems*, Elsevier, 1986, pp. 537–547. doi: 10.1016/B978-1-4832-8375-3.50060-6.

[4] K. Wróbel, J. Wróbel, W. Tokarz, J. Lach, K. Podsadni, and A. Czerwiński, “Hydrogen Internal Combustion Engine Vehicles: A Review,” *Energies (Basel).*, vol. 15, no. 23, p. 8937, Nov. 2022, doi: 10.3390/en15238937.

[5] R. Sari *et al.*, “Hydrogen Internal Combustion Engine Strategies for Heavy-Duty Transportation: Engine and System Level Perspective,” *SAE Int. J. Adv. Curr. Pract. Mobil.*, vol. 06, no. 6, pp. 2024-26–0175, Jan. 2024, doi: 10.4271/2024-26-0175.

[6] G. Kiesgen, M. Klüting, C. Bock, and H. Fischer, “The New 12-Cylinder Hydrogen Engine in the 7 Series: The H2 ICE Age Has Begun,” Apr. 2006. doi: 10.4271/2006-01-0431.

[7] S. Verhelst, “Recent progress in the use of hydrogen as a fuel for internal combustion engines,” *Int. J. Hydrogen Energy*, vol. 39, no. 2, pp. 1071–1085, Jan. 2014, doi: 10.1016/j.ijhydene.2013.10.102.

[8] World Health Organization, *WHO Global Air Quality Guidelines: Particulate matter (PM2.5 and PM10), ozone, nitrogen dioxide, sulfur dioxide and carbon monoxide*. 2021.

[9] I. Hernandez, C. Turquand D’Auzay, R. Penning, E. Shapiro, and J. Hughes, “Thermo-Diffusive Flame Speed Adjustment and its Application to Hydrogen Engines,” in *SAE Technical Papers*, SAE International, Apr. 2023. doi: 10.4271/2023-01-0197.

[10] T. L. Howarth and A. J. Aspden, “An empirical characteristic scaling model for freely-propagating lean premixed hydrogen flames,” *Combust. Flame*, vol. 237, p. 111805, Mar. 2022, doi: 10.1016/j.combustflame.2021.111805.

[11] T. L. Howarth, E. F. Hunt, and A. J. Aspden, “Thermodiffusively-unstable lean premixed hydrogen flames: Phenomenology, empirical modelling, and thermal leading points,” *Combust. Flame*, vol. 253, p. 112811, Jul. 2023, doi: 10.1016/j.combustflame.2023.112811.

[12] G. M. Kosmadakis, C. D. Rakopoulos, J. Demuynck, M. De Paepe, and S. Verhelst, “CFD modeling and experimental study of combustion and nitric oxide emissions in hydrogen-fueled spark-ignition engine operating in a very wide range of EGR rates,” *Int. J. Hydrogen Energy*, vol. 37, no. 14, pp. 10917–10934, Jul. 2012, doi: 10.1016/j.ijhydene.2012.04.067.

[13] C. D. Rakopoulos, G. M. Kosmadakis, J. Demuynck, M. De Paepe, and S. Verhelst, “A combined experimental and numerical study of thermal processes, performance and nitric oxide emissions in a hydrogen-fueled spark-ignition engine,” *Int. J. Hydrogen Energy*, vol. 36, no. 8, pp. 5163–5180, Apr. 2011, doi: 10.1016/j.ijhydene.2011.01.103.

[14] G. M. Kosmadakis, D. C. Rakopoulos, and C. D. Rakopoulos, “Assessing the cyclic-variability of spark-ignition engine running on methane-hydrogen blends with high

hydrogen contents of up to 50%," *Int. J. Hydrogen Energy*, vol. 46, no. 34, pp. 17955–17968, May 2021, doi: 10.1016/j.ijhydene.2021.02.158.

[15] S. Verhelst and T. Wallner, "Hydrogen-fueled internal combustion engines," *Prog. Energy Combust. Sci.*, vol. 35, no. 6, pp. 490–527, Dec. 2009, doi: 10.1016/j.pecs.2009.08.001.

[16] G. Maio, Z. Ding, K. Truffin, O. Colin, O. Benoit, and S. Jay, "ECFM-LES modeling with AMR for the CCV prediction and analysis in lean-burn engines," *Science and Technology for Energy Transition*, vol. 77, p. 20, Oct. 2022, doi: 10.2516/stet/2022017.

[17] G. Maio *et al.*, "Experimental and numerical investigation of a direct injection spark ignition hydrogen engine for heavy-duty applications," *Int. J. Hydrogen Energy*, vol. 47, no. 67, pp. 29069–29084, Aug. 2022, doi: 10.1016/J.IJHYDENE.2022.06.184.

[18] S. Sfriso, F. Berni, S. Fontanesi, A. D'Adamo, M. Antonelli, and S. Frigo, "A 3D-CFD Numerical Approach for Combustion Simulations of Spark Ignition Engines Fuelled with Hydrogen: A Preliminary Analysis," in *SAE Technical Papers*, SAE International, Apr. 2023. doi: 10.4271/2023-01-0207.

[19] S. Sfriso *et al.*, "Proposal and validation of a numerical framework for 3D-CFD in-cylinder simulations of hydrogen spark-ignition internal combustion engines," *Int. J. Hydrogen Energy*, vol. 53, pp. 114–130, Jan. 2024, doi: 10.1016/j.ijhydene.2023.12.027.

[20] S. Sfriso *et al.*, "Proposal and Validation of 3D-CFD Framework for Ultra-Lean Hydrogen Combustion in ICEs," in *SAE Technical Papers*, SAE International, Apr. 2024. doi: 10.4271/2024-01-2685.

[21] S. Sfriso *et al.*, "Combination of G-Equation and Detailed Chemistry: An application to 3D-CFD hydrogen combustion simulations to predict NOx emissions in reciprocating internal combustion engines," *Int. J. Hydrogen Energy*, vol. 89, pp. 161–176, Nov. 2024, doi: 10.1016/j.ijhydene.2024.09.252.

[22] S. Sfriso *et al.*, "On the influence of the H2 flame thermo-diffusive instability at engine-like conditions: A CFD-driven study," *Energy Convers. Manag.*, vol. 345, p. 120394, Dec. 2025, doi: 10.1016/j.enconman.2025.120394.

[23] S. Sfriso *et al.*, "3D-CFD simulations of H2 ICEs: a preliminary evaluation of a laminar flame speed correction for thermo-diffusive instability," 2024.

[24] S. Sfriso *et al.*, "Hydrogen and ICEs: validation of a 3D-CFD approach for in-cylinder combustion simulations of ultra-lean mixtures with a focus on the combustion regime," *Int. J. Hydrogen Energy*, vol. 175, p. 151347, Oct. 2025, doi: 10.1016/j.ijhydene.2025.151347.

[25] V. Yakhot and S. A. Orszag, "Renormalization group analysis of turbulence. I. Basic theory," *J. Sci. Comput.*, vol. 1, no. 1, pp. 3–51, 1986, doi: 10.1007/BF01061452.

[26] Siemens Digital Industries Software, *STAR-CD Methodology v2205.0001.* 2022.

[27] L. Teodosio and F. Berni, "Optimization via genetic algorithm of a variable-valve-actuation spark-ignition engine based on the integration between 1D/3D simulation codes and optimizer," *International Journal of Engine Research*, 2022, doi: 10.1177/14680874221099874.

[28] F. Berni *et al.*, "A zonal secondary break-up model for 3D-CFD simulations of GDI sprays," *Fuel*, vol. 309, Feb. 2022, doi: 10.1016/j.fuel.2021.122064.

[29] C. Iacovano, F. Berni, A. Barbato, and S. Fontanesi, "A Preliminary 1D-3D Analysis of the Darmstadt Research Engine under Motored Condition," in *E3S Web of Conferences*, EDP Sciences, Oct. 2020. doi: 10.1051/e3sconf/202019706006.

[30] S. Sparacino, F. Berni, M. Riccardi, A. Cavicchi, and L. Postrioti, "3D-CFD Simulation of a GDI Injector under Standard and Flashing Conditions," in *E3S Web of Conferences*, EDP Sciences, Oct. 2020. doi: 10.1051/e3sconf/202019706002.

[31] S. Sparacino, F. Berni, A. D'Adamo, V. K. Krastev, A. Cavicchi, and L. Postrioti, "Impact of the primary break-up strategy on the morphology of GDI sprays in 3D-CFD simulations of multi-hole injectors," *Energies (Basel).*, vol. 12, no. 15, Jul. 2019, doi: 10.3390/en12152890.

[32] F. Berni *et al.*, "Modeling of gaseous emissions and soot in 3D-CFD in-cylinder simulations of spark-ignition engines: A methodology to correlate numerical results and experimental data," *International Journal of Engine Research*, 2022, doi: 10.1177/14680874221112564.

[33] F. Berni, G. Cicalese, M. Borghi, and S. Fontanesi, "Towards grid-independent 3D-CFD wall-function-based heat transfer models for complex industrial flows with focus on in-cylinder simulations," *Appl. Therm. Eng.*, vol. 190, May 2021, doi: 10.1016/j.applthermaleng.2021.116838.

[34] F. Berni and S. Fontanesi, "A 3D-CFD methodology to investigate boundary layers and assess the applicability of wall functions in actual industrial problems: A focus on in-cylinder simulations," *Appl. Therm. Eng.*, vol. 174, Jun. 2020, doi: 10.1016/j.applthermaleng.2020.115320.

[35] F. Berni, G. Cicalese, S. Sparacino, and G. Cantore, "On the existence of universal wall functions in in-cylinder simulations using a low-Reynolds RANS turbulence model," in *AIP Conference Proceedings*, American Institute of Physics Inc., Dec. 2019. doi: 10.1063/1.5138752.

[36] R. Herweg and R. R. Maly, "A Fundamental Model for Flame Kernel Formation in S. I. Engines," *SAE Transactions*, vol. 101, pp. 1947–1976, 1992, [Online]. Available: http://www.jstor.org/stable/44611342

[37] M. Lee, M. Hall, O. Ezekoye, and R. Matthews, "Voltage, and Energy Deposition Characteristics of Spark Ignition Systems," *SAE Technical Papers*, Apr. 2005, doi: 10.4271/2005-01-0231.

[38] S. Huang, T. Li, P. Ma, S. Xie, Z. Zhang, and R. Chen, "Quantitative evaluation of the breakdown process of spark discharge for spark-ignition engines," *J. Phys. D Appl. Phys.*, vol. 53, no. 4, p. 045501, 2020, doi: 10.1088/1361-6463/ab56da.

[39] C. R. Stevens, "Energy Storage and the Criteria for Proper Ignition in the Internal Combustion Engine," *IEEE Transactions on Industrial Electronics and Control Instrumentation*, vol. IECI-12, no. 1, pp. 8–13, 1965, doi: 10.1109/TIECI.1965.229542.

[40] J. P. Trelles, J. V. R. Heberlein, and E. Pfender, “Non-equilibrium modelling of arc plasma torches,” *J. Phys. D Appl. Phys.*, vol. 40, no. 19, pp. 5937–5952, Oct. 2007, doi: 10.1088/0022-3727/40/19/024.

[41] J. P. Trelles, C. Chazelas, A. Vardelle, and J. V. R. Heberlein, “Arc plasma torch modeling,” *Journal of Thermal Spray Technology*, vol. 18, no. 5–6, pp. 728–752, Dec. 2009, doi: 10.1007/s11666-009-9342-1.

[42] J. Haidar, “Non-equilibrium modelling of transferred arcs,” *J. Phys. D: Appl. Phys*, vol. 32, pp. 263–272, 1999.

[43] A. Gleizes, J. J. Gonzalez, and P. Freton, “Thermal plasma modelling,” *J. Phys. D Appl. Phys.*, vol. 38, no. 9, May 2005, doi: 10.1088/0022-3727/38/9/R01.

[44] T. Lucchini *et al.*, “A Comprehensive Model to Predict the Initial Stage of Combustion in SI Engines,” in *SAE Technical Papers*, SAE International, Apr. 2013. doi: 10.4271/2013-01-1087.

[45] H. Willems and R. Sierens, “Modeling the initial growth of the plasma and flame kernel in SI engines,” *J. Eng. Gas Turbine. Power*, vol. 125, no. 2, pp. 479–484, Apr. 2003, doi: 10.1115/1.1501912.

[46] O. Colin and A. Benkenida, “The 3-Zones Extended Coherent Flame Model (Ecfm3z) for Computing Premixed/Diffusion Combustion,” *Oil & Gas Science and Technology*, vol. 59, no. 6, pp. 593–609, Nov. 2004, doi: 10.2516/ogst:2004043.

[47] N. Peters, *Turbulent Combustion*, vol. 12, no. 11. Cambridge University Press, 2000. doi: 10.1017/CBO9780511612701.

[48] R. Sola, “Correlazione numerico-sperimentale di un motore ad iniezione diretta alimentato ad idrogeno,” Università degli studi di Modena e Reggio Emilia, 2023.

[49] G. Damköhler, “Der Einfluss der Turbulenz auf die Flammengeschwindigkeit in Gasgemischen,” *Zeitschrift für Elektrochemie und angewandte physikalische Chemie*, vol. 46, no. 11, pp. 601–626, Nov. 1940, doi: 10.1002/bbpc.19400461102.

[50] R. Herweg and R. R. Maly, “A Fundamental Model for Flame Kernel Formation in S. I. Engines,” *JOURNAL OF ENGINES*, Oct. 1992, doi: 10.4271/922243.

[51] S. Verhelst, C. TJoen, J. Vancoillie, and J. Demuynck, “A correlation for the laminar burning velocity for use in hydrogen spark ignition engine simulation,” *Int. J. Hydrogen Energy*, vol. 36, no. 1, pp. 957–974, Jan. 2011, doi: 10.1016/j.ijhydene.2010.10.020.

[52] A. A. Konnov, “Yet another kinetic mechanism for hydrogen combustion,” *Combust. Flame*, vol. 203, pp. 14–22, May 2019, doi: 10.1016/j.combustflame.2019.01.032.

[53] S. R. . Turns, *An introduction to combustion : concepts and applications*. McGraw-Hill, 2012.

[54] M. Matalon, “The Darrieus-Landau instability of premixed flames,” *Fluid Dyn. Res.*, vol. 50, no. 5, Aug. 2018, doi: 10.1088/1873-7005/aab510.

[55] D. ter. Haar, *Collected Papers of L.D. Landau*. Elsevier Science, 2014.

[56] P. Clavin and P. Garcia, "The influence of the temperature dependence of diffusivities on the dynamics of flame fronts.," *Journal de Mécanique Théorique et Appliquée*, vol. 2, no. 2, pp. 245–263, 1983.

[57] G. I. SIVASHINSKY, "Diffusional-Thermal Theory of Cellular Flames," *Combustion Science and Technology*, vol. 15, no. 3–4, pp. 137–145, Jan. 1977, doi: 10.1080/00102207708946779.

[58] L. Berger, A. Attili, and H. Pitsch, "Intrinsic instabilities in premixed hydrogen flames: parametric variation of pressure, equivalence ratio, and temperature. Part 2 – Non-linear regime and flame speed enhancement," *Combust. Flame*, vol. 240, p. 111936, Jun. 2022, doi: 10.1016/j.combustflame.2021.111936.

[59] L. Berger, A. Attili, and H. Pitsch, "Synergistic interactions of thermodiffusive instabilities and turbulence in lean hydrogen flames," *Combust. Flame*, vol. 244, p. 112254, Oct. 2022, doi: 10.1016/j.combustflame.2022.112254.

[60] L. Berger, K. Kleinheinz, A. Attili, and H. Pitsch, "Characteristic patterns of thermodiffusively unstable premixed lean hydrogen flames," *Proceedings of the Combustion Institute*, vol. 37, no. 2, pp. 1879–1886, 2019, doi: 10.1016/j.proci.2018.06.072.

[61] N. Fogla, F. Creta, and M. Matalon, "Effect of folds and pockets on the topology and propagation of premixed turbulent flames," *Combust. Flame*, vol. 162, no. 7, pp. 2758–2777, Jul. 2015, doi: 10.1016/j.combustflame.2015.04.012.

[62] A. S. AL-SHAHRANY, D. BRADLEY, M. LAWES, K. LIU, and R. WOOLLEY, "DARRIEUS–LANDAU AND THERMO-ACOUSTIC INSTABILITIES IN CLOSED VESSEL EXPLOSIONS," *Combustion Science and Technology*, vol. 178, no. 10–11, pp. 1771–1802, Dec. 2006, doi: 10.1080/00102200600788734.

[63] L. Berger, A. Attili, M. Gauding, and H. Pitsch, "Effects of Karlovitz number variations on thermodiffusive instabilities in lean turbulent hydrogen jet flames," *Proceedings of the Combustion Institute*, vol. 40, no. 1–4, p. 105219, 2024, doi: 10.1016/j.proci.2024.105219.

[64] D. Bradley, P. H. Gaskell, X. J. Gu, and A. Sedaghat, "Premixed flamelet modelling: Factors influencing the turbulent heat release rate source term and the turbulent burning velocity," *Combust. Flame*, vol. 143, no. 3, pp. 227–245, Nov. 2005, doi: 10.1016/j.combustflame.2005.05.014.

[65] D. Bradley, M. Lawes, K. Liu, and M. S. Mansour, "Measurements and correlations of turbulent burning velocities over wide ranges of fuels and elevated pressures," *Proceedings of the Combustion Institute*, vol. 34, no. 1, pp. 1519–1526, 2013, doi: 10.1016/j.proci.2012.06.060.

[66] A. J. Aspden, M. S. Day, and J. B. Bell, "Characterization of low Lewis number flames," *Proceedings of the Combustion Institute*, vol. 33, no. 1, pp. 1463–1471, 2011, doi: 10.1016/j.proci.2010.05.090.

[67] M. Antonelli and L. Martorano, "Realization and testing of a low pressure hydrogen direct injection engine using commercial injectors," in *SAE Technical Papers*, SAE International, 2012. doi: 10.4271/2012-01-0652.

[68] A. Simi, “Hydrogen direct injection in recirpocating engines using commercial injectors,” PhD Dissertation, 2011.

[69] M. Antonelli and L. Martorano, “Analisi numerica e sperimentale dei processi di iniezione e miscelamento in un piccolo motore ad iniezione diretta di idrogeno,” 67° Congresso Nazionale ATI – Trieste, 2012.

[70] M. Scarselli, “Studio CFD dell’influenza della forma della camera di combustione di un motore ad iniezione diretta sul miscelamento tra aria ed idrogeno,” Bachelor degree Thesis, 2013.

[71] M. Antonelli and L. Martorano, *ANALISI NUMERICA E SPERIMENTALE DEI PROCESSI DI INIEZIONE E MISCELAMENTO IN UN PICCOLO MOTORE AD INIEZIONE DIRETTA DI IDROGENO.* 2012.

[72] S. Fontanesi, L. Postrioti, M. Magnani, M. Martino, G. Brizi, and G. Cicalese, “Preliminary Assessment of Hydrogen Direct Injection Potentials and Challenges through a Joint Experimental and Numerical Characterization of High-Pressure Gas Jets,” in *SAE Technical Papers*, SAE International, Sep. 2022. doi: 10.4271/2022-24-0014.

[73] Bulat Mikhail Pavlovich and Bulat Pavel Victorovich, “Comparison of Turbulence Models in the Calculation of Supersonic Separated Flows,” *World Appl. Sci. J.*, vol. 27, no. 10, pp. 1263–1266, 2013.

[74] V. De Bellis *et al.*, “Development and validation of a phenomenological model for hydrogen fueled PFI internal combustion engines considering Thermo-Diffusive effects on flame speed propagation,” *Energy Convers. Manag.*, vol. 308, p. 118395, May 2024, doi: 10.1016/j.enconman.2024.118395.

[75] A. Scalambro, A. Piano, and F. Millo, “Modelling thermodiffusive instabilities in hydrogen flames and their impact on the combustion process in a direct-injection hydrogen engine,” *Combust. Flame*, vol. 282, p. 114457, Dec. 2025, doi: 10.1016/j.combustflame.2025.114457.

[76] R. Novella, J. Gomez-Soriano, D. González-Domínguez, and O. Olaciregui, “Understanding the role of thermo-diffusive instabilities in hydrogen combustion for lean-burn spark-ignition engine operation,” *Energy Convers. Manag.*, vol. 334, p. 119801, Jun. 2025, doi: 10.1016/j.enconman.2025.119801.

[77] L. Sforza, T. Lucchini, A. Onorati, X. Zhu, and S.-Y. Lee, “Modeling Ignition and Premixed Combustion Including Flame Stretch Effects,” Mar. 2017. doi: 10.4271/2017-01-0553.

[78] K. P. Shrestha, L. Seidel, T. Zeuch, and F. Mauss, “Detailed Kinetic Mechanism for the Oxidation of Ammonia Including the Formation and Reduction of Nitrogen Oxides,” *Energy & Fuels*, vol. 32, no. 10, pp. 10202–10217, Oct. 2018, doi: 10.1021/acs.energyfuels.8b01056.

[79] S. J. Klippenstein, L. B. Harding, P. Glarborg, and J. A. Miller, “The role of NNH in NO formation and control,” *Combust. Flame*, vol. 158, no. 4, pp. 774–789, Apr. 2011, doi: 10.1016/j.combustflame.2010.12.013.

[80] C. Ramalho Leite, M. Laignel, P. Brequigny, J. Borée, and F. Foucher, “Experimental Combustion Analysis in a Gasoline Baseline Hydrogen-Fueled Internal Combustion Engine at Ultra-Lean Conditions,” in *SAE Technical Papers*, SAE International, Aug. 2023. doi: 10.4271/2023-24-0073.

[81] S. Sfriso, F. Berni, S. Fontanesi, A. D’Adamo, M. Antonelli, and S. Frigo, “A 3D-CFD Numerical Approach for Combustion Simulations of Spark Ignition Engines Fuelled with Hydrogen: A Preliminary Analysis,” Apr. 2023. doi: 10.4271/2023-01-0207.

[82] K. N. C. Bray, “Topics in Applied Physics (P. A. Libby and F. A. Williams, Eds),” 1980, *Springer Verlag*.

[83] N. Peters, “Twenty-First Symposium (International) on Combustion,” 1988, *The Combustion Institute*.

[84] C. Ramalho Leite, P. Brequigny, J. Borée, and F. Foucher, “Early flame development characterization of ultra-lean hydrogen–air flames in an optical spark-ignition engine,” *Proceedings of the Combustion Institute*, vol. 40, no. 1–4, p. 105260, 2024, doi: 10.1016/j.proci.2024.105260.

[85] J. B. Heywood, *Internal Combustion Engines Fundamentals*. New York, 1988.

[86] S. B. Pope, *Turbulent Flows*. Cambridge: Cambridge University Press, 2000.

[87] C. Ramalho Leite, P. Brequigny, J. Borée, and F. Foucher, “Early flame development characterization of ultra-lean hydrogen–air flames in an optical spark-ignition engine,” *Proceedings of the Combustion Institute*, vol. 40, no. 1–4, p. 105260, 2024, doi: 10.1016/j.proci.2024.105260.

[88] SIEMENS PLM, “STARCD v4.34 Manual - Methodology,” 2020.

[89] G. Bruneaux, “Asymptotic analysis, direct numerical simulation and modeling of premixed turbulent flame-wall interaction; Etude asymptotique, simulation numerique directe et modelisation de l`interaction flamme turbulente premelangee-paroi,” Ph.D. Thesis, Institut Francais du Petrole (IFP), 92 - Rueil-Malmaison (France), 1996.

[90] L. Berger, A. Attili, and H. Pitsch, “Synergistic interactions of thermodiffusive instabilities and turbulence in lean hydrogen flames,” *Combust. Flame*, vol. 244, p. 112254, Oct. 2022, doi: 10.1016/j.combustflame.2022.112254.